University of Groningen

Laser-deposited metallic coatings

Hemmati, Ismail

IMPORTANT NOTE: You are advised to consult the publisher's version (publisher's PDF) if you wish to cite from it. Please check the document version below.

Document Version
Publisher's PDF, also known as Version of record

Publication date:
2013

Link to publication in University of Groningen/UMCG research database

Citation for published version (APA):
Hemmati, I. (2013). *Laser-deposited metallic coatings: processing, characterization, alloy development*. s.n.

Copyright
Other than for strictly personal use, it is not permitted to download or to forward/distribute the text or part of it without the consent of the author(s) and/or copyright holder(s), unless the work is under an open content license (like Creative Commons).

The publication may also be distributed here under the terms of Article 25fa of the Dutch Copyright Act, indicated by the "Taverne" license. More information can be found on the University of Groningen website: https://www.rug.nl/library/open-access/self-archiving-pure/taverne-amendment.

Take-down policy
If you believe that this document breaches copyright please contact us providing details, and we will remove access to the work immediately and investigate your claim.

Downloaded from the University of Groningen/UMCG research database (Pure): http://www.rug.nl/research/portal. For technical reasons the number of authors shown on this cover page is limited to 10 maximum.

Download date: 05-05-2023

rijksuniversiteit
groningen

LASER-DEPOSITED METALLIC COATINGS

Processing, Characterization, Alloy Development

Proefschrift

ter verkrijging van het doctoraat in de
Wiskunde en Natuurwetenschappen
aan de Rijksuniversiteit Groningen
op gezag van de
Rector Magnificus, dr. E. Sterken,
in het openbaar te verdedigen op
vrijdag 1 november 2013
om 14.30 uur

door

Ismail Hemmati

geboren op 21 september 1981
te Kermanshah, Iran

Promotor:	Prof. dr. J. T. M. de Hosson
Copromotor:	Dr. V. Ocelik
Beoordelingscommissie:	Prof. dr. P. Rudolf Prof. dr. H. A. De Raedt Prof. ir. L. Katgerman

LASER-DEPOSITED METALLIC COATINGS

Processing, Characterization, Alloy Development

Ismail Hemmati

ISBN: 978-90-77172-94-0
Zernike Institute PhD thesis series 2013-17
ISSN: 1570-1530

Front cover: Scanning Electron Microscopy image of a chromium boride crystal (black) with niobium carbide precipitates (white) on its edges.

Back cover: Scanning Electron Microscopy image along with Orientation Imaging Microscopy maps (phase and orientation) showing the formation of CrB crystals on a single-crystal NbC precipitate.

This research was carried out under project number MC7.06259 in the framework of the Research Program of Materials innovation institute (M2i) in the Netherlands (www.m2i.nl).

To all from whom I have learned.

Contents

Chapter 1

INTRODUCTION

1.1 Laser deposition technologies

LASER (acronym for Light Amplification by Stimulated Emission of Radiation) is basically a coherent and monochromatic beam of electromagnetic radiation with the wavelength ranging from ultraviolet to infrared. The first working laser was constructed and demonstrated by Dr. Theodore H. Maiman in 1960. However, it was not until a decade later that the potentials of laser beam as a flexible machine tool for materials processing were noticed. As more powerful industrial laser sources were developed at lower prices, laser processing of engineering materials emerged as a new industry. Today, laser is an indispensable manufacturing tool in a wide range of materials processing applications. Its light produces a localized and highly controllable energy source which can be easily transferred and manipulated using optical devices. Owing to unique properties of the laser beam, many industries in automotive, aerospace, power generation, defense and several other sectors are widely applying laser technologies for cutting, welding, surface modification, near-net shape fabrication, etc.

Among the diverse applications of laser for processing of engineering materials, laser deposition technologies have received significant attention in recent years due to their enormous potential for coating, repair and even low-volume manufacturing. A broad range of laser deposition technologies have been developed by various research institutions, each with their own

respective names. In the coating applications, “laser cladding” is used frequently to address the laser deposition technology to produce thick protective coatings but other names such as “laser coating” and “laser powder deposition” are also used. In rapid prototyping or layered manufacturing, diversity of the names is even more and includes terms such as “Laser Engineered Net Shaping (LENS®), “direct metal deposition” (DMD^{TM}), “Laser direct casting” (LDC) and “laser additive manufacture” (LAM^{SM}) among others[1]. In this thesis, the terms “laser cladding” and “laser deposition” will be used interchangeably as the focus of the work will be on deposition of thick (in the millimeter range) metallic coatings on steel substrates using laser beam and powder injection.

1.1.1. Principles of laser cladding process

In laser cladding, a high-power laser beam is used to melt a thin layer of the substrate along with majority of the additional coating material. The molten coating material joins the melt pool formed on the surface of a substrate and the mixture solidifies when the melt pool and laser beam are moved relative to each other[1].

The coating material can be provided by different methods such as pre-placed powder bed, wire feeding or powder injection. Among them, powder injection during the laser cladding process has been demonstrated to be the most applicable and versatile. Addition of the coating material via powder injection can be done using side or coaxial cladding nozzle as shown in Figure 1.1. Powder injection using side cladding nozzle may result in high powder catchment efficiency. But it has the drawback of being directional. As a result, side cladding injection nozzle is more suitable for cladding on simple geometries. With coaxial injection nozzle, this limitation does not exist anymore and cladding can be carried out in any direction and on complex three-dimensional geometries[1].

An advantage of powder injection is that composition of the deposit can be varied in situ or different powders can be mixed and injected simultaneously. This capability was intensively used in the current work to deposit coatings with new and variable compositions. In both powder injection methods, a carrier gas such as argon, helium or nitrogen is used to deliver the powder stream from feeder to the injection nozzle. Furthermore, the melt pool is protected by a shielding gas, usually of the same type as carrier gas[2].

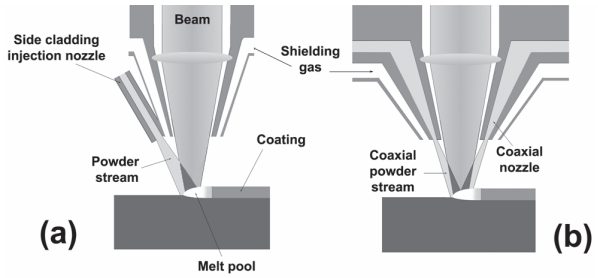

Figure 1.1. (a) Side and (b) coaxial set-ups for laser cladding by powder injection[3].

1.1.2. Advantages and drawbacks of laser cladding

In coating and repair applications, there are three main technologies competing against laser cladding: Plasma Spraying, High Velocity Oxy-Fuel (HVOF) and Plasma Transferred Arc (PTA) welding. Plasma Spraying is extensively used to deposit a diverse range of wear- and corrosion-resistant coatings with a limited heat input to the substrate. However, the deposits suffer from porosity, chemical inhomogeneity and weak bonding to the substrate. HVOF produces coatings with higher densities and better adhesion in comparison to those produced by Plasma Spraying. But the coatings are still mechanically bonded to the substrate. On the other hand, PTA welding produces fully dense coatings with metallurgical bonding to their substrate. However, the heat input is usually high which results in high dilution from the substrate, a large Heat Affected Zone (HAZ) and distortion of the substrate[1].

Laser deposition technologies have distinct advantages in comparison to all of the above-mentioned techniques. The highly controllable and localized energy of laser beam results in minimal dilution from the base metal, lower heat input and hence less distortion and smaller HAZ in the substrate component. In addition, laser-deposited coatings are fully dense with metallurgical bonding to the substrate. Laser deposition technologies are also amenable to automation and computer control. Consequently, excellent control of the layer thickness and composition, better surface quality and tight dimensional tolerances with higher material usage and little or no after-machining can be achieved in laser-deposited samples. Furthermore, laser deposition is more capable of selective and precise build-up on sensitive high-value components[1,2].

Currently, the main drawbacks of laser deposition technologies are higher investment costs, lower deposition rates and limited familiarity of

managers in comparison to competing technologies. Nevertheless, technological advancements in laser deposition technologies such as introduction of high power diode lasers with beam as wide as 2.5 cm, induction-assisted laser cladding heads and feedback control systems are rapidly solving the issue of low deposition rate. For example, with the laser as the only energy source, deposition rates of 9 kg/h of Inconel 625 corrosion protective coatings on large cylindrical components are reported. Furthermore, a deposition rate of 14-16 kg/h of Inconel 625 can be achieved with the simultaneous application of 8 kW laser and 12 kW induction power[4]. The other issues are also expected to be solved within a few years as more applications emerge and laser systems will be manufactured at lower costs.

The most important quality issue with laser-deposited samples is cracking[5] which is basically caused by high cooling rates, as will be discussed in detail in CHAPTER 5. Other defects usually occur because processing parameters are not properly adjusted. For example, excessive laser powers could result in too much dilution from the substrate which modifies the composition of the deposits and deteriorates their properties[6]. Dilution is an important quality measure for laser-deposited coatings and can be defined in the following two ways:

(i) Geometrical[7]: by calculating the ratio of the area of melted substrate to the total melted and deposited areas using *Eq. 1.1* as shown in Figure 1.2.

(ii) Compositional[2]: based on the concentration of a certain alloying elements using *Eq. 1.2*.

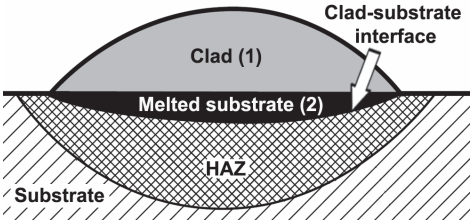

$$dilution = \frac{area(2)}{area(1) + area(2)} \qquad Eq.\ 1.1$$

Figure 1.2. Geometrical definition of dilution using a single laser-deposited track[7].

$$dilution = \frac{\rho_p (X_d - X_p)}{\rho_s (X_s - X_d) + \rho_p (X_d - X_p)} \qquad Eq.\ 1.2$$

in which ρ_p, ρ_s, X_d, X_p and X_s are density of the melted powder alloy (g/mm^3), density of the substrate (g/mm^3), weight percent of element X in the deposit, weight percent of element X in the powder alloy and weight

percent of element X in the substrate, respectively. In laser clad coatings, a dilution of around 5% is desirable as it will guarantee a strong bonding with minimum mixing from substrate.

Other defects such as porosity may also occur in laser-deposited samples. Porosity is usually caused by trapped pockets of gas[1]. Such gas pockets could be generated in a number of ways including contamination of substrate surface or moisture in the power. Hollowed particles of gas atomized powders can also lead to coarse porosity in the deposits as shown in Figure 1.3. This type of porosity occurs more severely at higher deposition rates. The clad layer shown in Figure 1.3 was deposited from the hollowed particles of a gas-atomized Ni-base hardfacing alloy powder at 40 mm/s transverse rate.

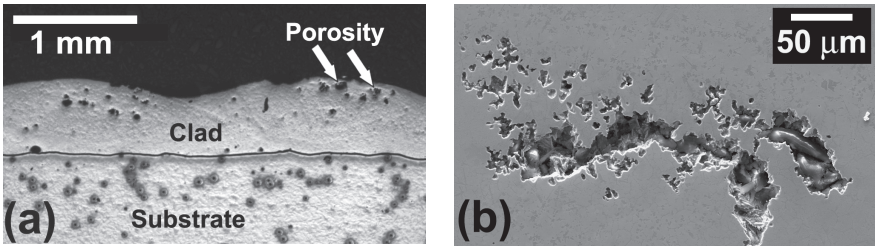

Figure 1.3. (a) Optical microscopy image of porosity in a laser-deposited coating, (b) Scanning electron microscopy image showing the internal pores.

1.1.3. Materials used in laser deposition

In coating applications, corrosion- and/or wear-resistant Co, Ni and Fe based alloys are the most widely used coating materials[1,2]. Stellite alloys (Kennametal-Stellite Inc.) or their equivalents from other manufacturers are the most commonly used Co-based hardfacing alloys. These Co-Cr-Mo-W-C alloys possess good mechanical, thermal and chemical properties, especially at high temperatures. Ni-base alloys are suitable for applications requiring good corrosion/wear resistance in aggressive environments (e.g. sea water). The most widely used Ni-base hardfacing alloys are Ni-Cr-B-Si-C from the Colmonoy alloy family (Wall Colmonoy Ltd.). In comparison to Co- and Ni-base alloys, Fe-base alloys are less widely used in coating applications. Wear resistant tool steels or corrosion/wear resistant austenitic and martensitic stainless steels have been used in laser cladding. In addition to metallic materials, metal-ceramic composites such as Ni-WC are widely deposited by laser cladding to produce wear-resistant coatings[1,2]. In the current research, AISI 431 martensitic stainless steel powder and various types of Ni-base

hardfacing alloy powders were deposited on steel substrates. Properties of these materials will be examined in more details in the next chapters.

1.1.4. Industrial applications of laser cladding

Laser deposition was originally developed as a surfacing tool. Subsequent refinements and utilization of other technologies such as robotics, sensors, control and computer-aided design and manufacturing (CAD/CAM), transformed the original surfacing technology into a flexible and cost-effective coating, repair and near net-shape manufacturing tool[1]. Until recent years, only components of very high value or complex geometries were coated or refurbished by laser deposition technologies over relatively small areas. In recent years, development of more powerful and reliable laser sources at lower costs has expanded the application of these technologies to also include lower value items and large area depositions in a broader range of industries. Some application examples are presented below.

1.1.4.1. Aeroengine turbine blade

The aerospace industry has always pioneered the application of laser deposition technologies for coating, repair and recently, three-dimensional manufacturing of turbine blades. The first reported use of laser cladding by industry was hardfacing of a Nimonic turbine blade interlock shroud by Rolls Roys in 1981[2]. Nowadays, several companies including General Electric, Honeywell, Rolls Roys, Pratt & Whitney, MTU, Sulzer, KLM, etc. employ laser cladding for coating and repair of turbine blades and other components of aeroengines[1,2]. Figure 1.4 presents examples of turbine blade coating and repair by laser cladding.

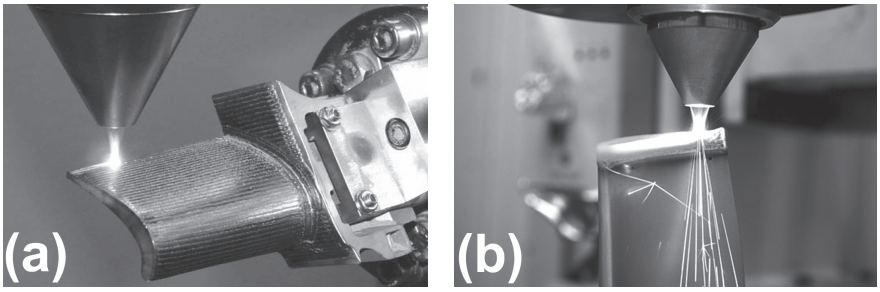

Figure 1.4. (a) Coating, and (b) repair of turbine blades using laser cladding[8,9].

1.1.4.2. Tools

Laser cladding is being used to deposit surface protective coatings or to adjust manufacturing errors in different types of dies, molds, blades, drilling tools, etc. Hardfacing alloys such as Ni-Cr-B-Si-C or Stellite are used to protect the glass-molding or hot forming dies against wear. Examples are shown in Figure 1.5. Laser cladding can be used to protect a wide range of metallic components operating in harsh environments which are exposed to corrosion, abrasion, fretting, particle erosion, etc. Typical examples are the downhole drilling tools for mining, oil and gas industries (Figure 1.6). In recent years, laser clad Tungsten carbide composite coatings (e.g. Ni-WC) have been used to increase the lifetime of drilling tools[10,11]. Adjusting the manufacturing errors can be done with the same material as that of the original component (usually alloy steels) or similar alloys.

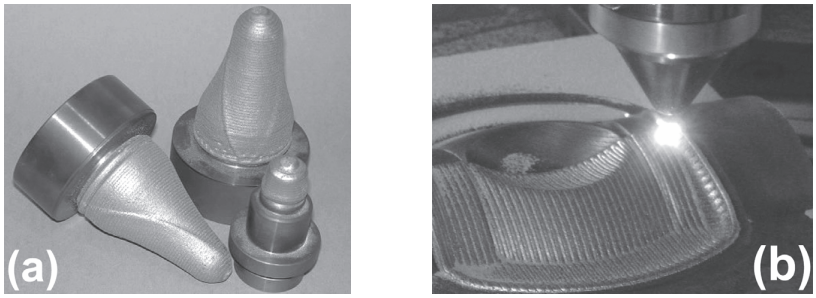

Figure 1.5. (a) Laser-clad coated glass plungers, (b) laser cladding of a hot-forming die[8,11].

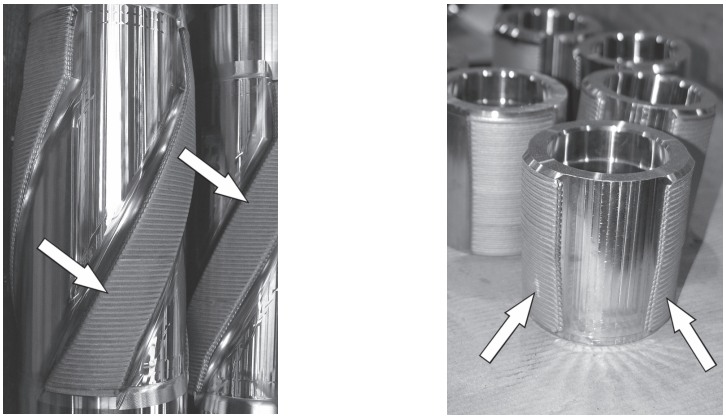

Figure 1.6. Drilling tools with laser-clad WC composite coatings in selected areas[10]. The clad areas are highlighted by arrows.

1.1.4.3. Valve seat and insert cladding

Internal combustion engine valves (e.g. for ships or automobiles) or control valve used in power plants and similar industries must be capable of withstanding very high contact stresses at high temperature and corrosive environments[2,12,13]. Laser cladding has long been used to protect the seat face or the entire surface of such valves against corrosion, wear and impact. Figure 1.7 shows the laser cladding of a diesel engine seat face. Cobalt- and nickel-base hardfacing alloys have been the primary coating materials in most cases. In some automotive engines, the valve seat shrink-fit inserts have also been replaced by a laser-deposited ring of suitable material. Such a replacement is reported to slightly improve the engine performance[13].

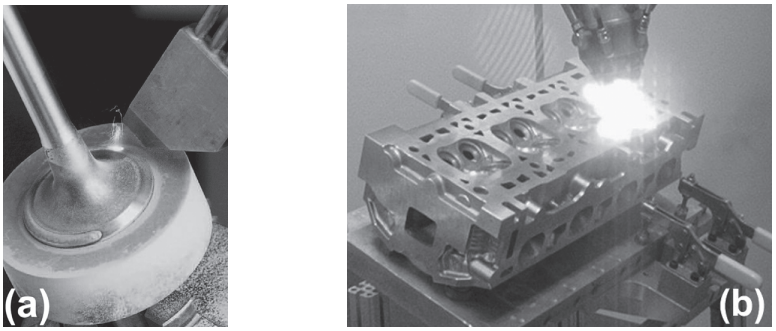

Figure 1.7. (a) Laser cladding of the valve seat face[14], (b) laser deposition as a replacement for valve seat inserts[15].

Laser deposition technologies are being used to enhance the performance of many other components with the range of the applications continuously expanding[1,2,10,11]. As explained before, new types of laser and deposition systems have dramatically increased the deposition rates of laser-based additive technologies[4]. This means that large areas can be protected by laser-deposited coatings not only with superior properties, but also at costs comparable to those of more established techniques such as thermal spraying. An example of such large area depositions is laser cladding of piston rods for large hydraulic cylinders. As this example was the main application target of the work reported in this thesis, it will be examined in more details.

1.2 Laser-deposited coatings for hydraulic piston rods

Hydraulic cylinders are used to transmit heavy forces in many applications in metal forming, construction, marine, drilling, aerospace and other industries.

The surface of piston rods is among the most important parts in any hydraulic cylinder[16]. In subsea applications such as dam gates, valve opening and closing systems, riser tensioners for splash zones or dredging machines, the surface of the hydraulic piston rods should be protected against various levels of wear and more importantly against corrosion from sea water.

Several coating techniques such as Electroplated Hard Chrome (EHC), Plasma Spraying, HVOF and PTA welding have previously been employed to protect the surface of piston rods[17]. Each of these techniques has its own advantages and limitations and can be used for certain environments and applications[18]. Currently, most of the piston rods are protected by either HVOF or PTA welding[19]. HVOF produces coatings which are less porous and brittle than Plasma Sprayed coatings but they are still mechanically bonded to the substrate. As a result, HVOF coatings may still suffer malfunction because of delamination after a relatively short period of time. Figure 1.8 shows failure of a hydraulic tensioner piston rod caused by coating delamination[19]. PTA welding is capable of producing fully dense and metallurgically-bonded layers which are far more ductile than the layers deposited by the previous methods and do not suffer from delamination. However, PTA process introduces a significant heat input to the substrate which increases the risk of piston rod distortion and iron pick-up to the coating.

In recent years, several companies such as *Eaton*[18], *Douce Hydro*[20], *Innoteq*[21] and *Praxair*[22] have developed or applied laser cladding processes to deposit protective coatings on hydraulic piston rods intended for extreme working environments such as marine applications. Figure 1.9 shows a hydraulic piston rod being coated by laser cladding. Laser-clad coatings basically offer all the benefits of PTA welded coatings. In addition, less heat will be introduced to the piston rod and dilution from the substrate will be much lower in laser-deposited coatings. An excellent performance and longer lifetimes (in comparison to pistons coated by previous methods) have been reported for the laser clad coated hydraulic piston rods[17–19,22].

A new and challenging application for laser cladding is protection of the hydraulic piston rods used in the dredging industry. In this case, the piston rod should not only be protected against corrosion by sea water, but also against the erosive and abrasive wear damage by the dredging products. Currently, the piston rods used in dredging industry are protected mostly by Plasma Spray or HVOF coatings of oxides of aluminum, titanium and chromium (usually with a NiCr bond layer)[23]. These ceramic coatings are applied because of their chemical resistance as well as their very high

hardness (~ 1200 HV) necessary to combat the wear damage during dredging operation. As a result, a minimum level of hardness is required for laser-deposited piston rod coatings which is higher than most of the previously developed laser clad coatings such as *LaserteK*® (300 HV)[20] or *Eatonite*™ *ABC-L1* (370-420 HV)[18]. These laser-deposited coatings are developed mainly for marine applications in which failure of the piston rods is largely corrosion related with little damage from wear. Deposition of harder coatings by laser cladding involves a serious risk of crack generation in the deposits which is totally unacceptable for components intended for subsea applications.

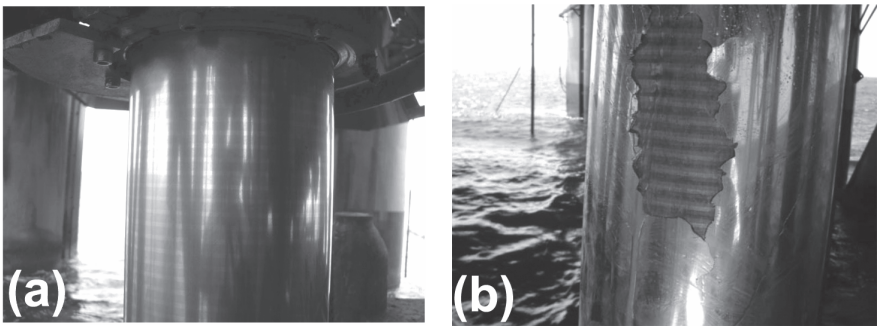

Figure 1.8. (a) Piston rod of a hydraulic tensioner with coating in a good condition, (b) the same piston rod with extensive delamination of the coating[19].

Figure 1.9. Laser cladding of a hydraulic piston rod[18].

So far, most of the laser clad coatings developed for hydraulic piston rods have been of Ni-base type. Inconel 625 has been used for applications involving a limited amount of wear[17,19]. Some companies such as Eaton have developed their proprietary Ni-base alloy to produce the *Eatonite*™ *ABC-L1* laser clad coatings reported to be twice as hard as Inconel 625[18]. Cobalt-base alloys can also be used for coating of hydraulic piston rods. Micro-Melt® CCW from Carpenter Technologies is a Co-base powder specifically

developed for laser cladding of tensioners in offshore drilling rigs[24]. Hardness of Micro-Melt® CCW laser-deposited coatings is expected to be around 400 HV. Ultimet® is another Co-base alloy for laser cladding applications with the same level of hardness as Micro-Melt® CCW[25]. Both of these alloys have shown excellent corrosion resistance in marine applications.

Apart from the higher price of Co-base alloys in comparison to Ni-base alloys, previous experiences of the industrial partner of this work (MTI Holland) showed that laser-deposited Ultimet coatings are not suitable for dredging applications because of high levels of abrasion damage. Similarly, Inconel 625 coatings did not have enough wear resistance for all dredging conditions. Based on these experiences as well as the data available from the other laser-clad piston rod coatings, it was decided in this work to choose Ni-base alloys capable of producing a hardness of above 400 HV as the coating material. For this purpose, two families of Ni-base alloys, namely Ni-Cr-B-Si-C and Ni-Cr-Mo-C were further analyzed to select the final alloy candidates. During the course of this research, several alloys from these two families including Colmonoy 69, Eatonite 5 and Nucalloy 488V were deposited, characterized and in some cases modified. More details about coatings from each alloy and their properties will be discussed in the relevant chapters.

1.3 Research and development in laser deposition

Since the 1980s, laser deposition technologies have been investigated to provide effective solutions for coating, repair and rapid prototyping and tooling purposes. Continuous research and development in this field have been driven by numerous successful applications such as those mentioned in the previous section as well as the enormous potential for new applications[26]. Research and development in laser deposition technologies can be divided into two general areas:

(i) Engineering developments including process monitoring and control, new laser machines, optical systems, beam shaping and manipulation, powder injection nozzles, laser hybrid processing, etc.[1,2,14,26].

(ii) Scientific research on solidification, microstructural development and characterization, processing-microstructure-properties relationships, alloy design and development, deposition of different materials including metal-ceramic composites and Functionally Gradient Materials (FGM), etc.[1,2,26].

The current work is an application-oriented scientific research which covers a wide range of subjects including studying the effects of deposition

parameters on microstructure/properties, characterization of constituent phases and microstructural developments, development of new alloys, assessing the functional properties of the deposits, etc. Various research highlights could be mentioned for this thesis including high-speed laser cladding (CHAPTER 3), microstructural and phase identification (CHAPTERS 3 to 6), alloy development (CHAPTERS 5 and 6) and tackling the cracking problem (CHAPTER 5). A subject which is common between all chapters of this work is solidification. Laser deposition is a rapid solidification process which involves a cooling rate of up to 10^5 K/s. In such high cooling rate, a considerable departure from equilibrium may happen which can result in extended solubilities, microstructural refinement, formation of metastable phases, phase selection processes, morphological changes and formation of amorphous phases[26,27]. Many of these phenomena were observed during the course of this work, sometimes with profound microstructural and functional consequences. A short overview of solidification during laser cladding process will be presented here.

Figure 1.10 shows a longitudinal section through the centerline of the melt pool during solidification of a laser-deposited track of coating. During laser cladding at constant power and beam speed, a steady-state melt pool is created after some time. Solidification front grows anti-parallel to the direction of heat extraction which is normal to the solid-liquid interface. As a result, growth velocity of the solidification front (V_n) can be correlated to the laser beam speed V_b via the equation $V_n = V_b.\cos(\theta)$. The angle θ shown in Figure 1.10 varies from 90° to 0° from bottom to top of the melt pool. As a result, V_n changes from zero to V_b. Temperature gradient in the melt pool (G) is another important parameter in the solidification of laser clad coatings. It has the highest value at clad-substrate interface and falls towards the top. Combinations of V_n and G define two other important parameters, namely cooling rate ($\dot{T}$) which is equal to $G * V_n$ in directional solidification and G / V_n which determines the stability of the solidification front. The graphs of Figure 1.10 also show variations of these two parameters from bottom to top of the melt pool during rapid solidification in laser cladding process[28]. Variations of V_n and G results in the highest value of G / V_n at the clad-substrate interface with a continuous decrease towards top of the melt pool. $\dot{T}$ follows an opposite trend with the highest value at top of the melt pool and

continuously decreasing towards the clad-substrate interface[28]. This can be explained by the fact that heat extraction is mainly done by the substrate through the clad-substrate interface. Hence, the cooling rate is the lowest close to that area because the heat released further away has to pass through the interface region. It should be noticed that variations in $G*V_n$ and G/V_n could also happen along the length of the clad layer if heat accumulation happens or the deposition rate (V_b) changes.

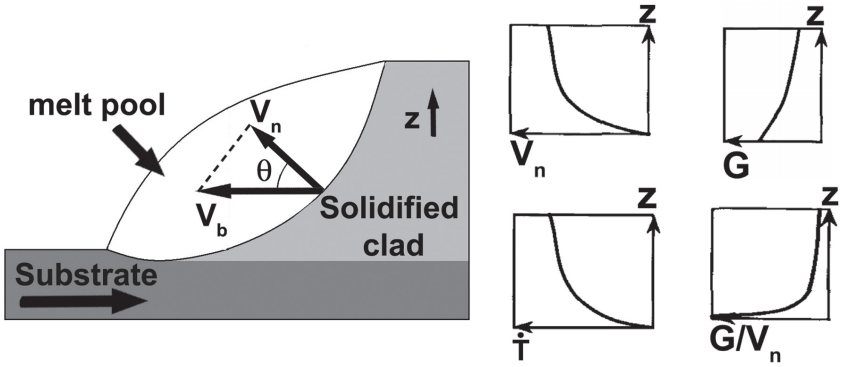

Figure 1.10. Longitudinal cross-section of the melt pool during solidification in laser cladding process along with changes of the solidification parameter across the depth of the melt pool[28].

Depending on sensitivity of the alloy systems, variations in solidification conditions, i.e. changes in $G*V_n$ and G/V_n could generate a number of phenomena along the depth and length of the clad layers. Transitions between columnar and equiaxed dendrites in AISI 431 (CHAPTER 3) and Colmonoy 69 (CHAPTER 4), epitaxial growth in multi-layer AISI 431 deposits (CHAPTER 3), formation of metastable phases in Colmonoy 69 (CHAPTER 4), phase selection processes in Colmonoy 69 and Zr-modified Colmonoy 69 (CHAPTERS 4 and 5) and in-situ formation of carbides in Colmonoy 69 deposits modified by vanadium, niobium or zirconium additions (CHAPTER 5) are among the solidification phenomena which will be explained in more details later.

1.4 Scope of the thesis

This research was carried out under the project number MC7.06259 in the framework of Materials innovation institute (M2i) research program at the Materials Science group, Department of Applied Physics, Zernike Institute for

Advanced Materials of the University of Groningen. Scope of the project was laser cladding of hardfacing metallic powders for corrosion/wear protection. The project had an experimental approach with a strong emphasis on the processing-microstructure-properties relationships. These relationships were studied by a range of experimental devices as explained in CHAPTER 2.

The work was done in two parts; the first part consisted of a curiosity-driven research on the effect of deposition rate on microstructure and properties of laser-deposited AISI 431 martensitic stainless steel coatings. The results of this part which are reported in CHAPTER 3 showed that contrary to what is widely believed, faster cooling rates at higher deposition speeds do not necessarily improve the functional properties of the coatings and depends very much on the alloy system.

The second part of the work which constitutes the majority of this thesis was focused on developing laser clad coatings to protect piston rods of hydraulic cylinders used in dredging ships. For this purpose, different types of Ni-base alloys were deposited and analyzed. The experiments started with Colmonoy 69 which is a hard Ni-Cr-B-Si-C alloy (hardness of around 800 HV) with molybdenum and copper additions which make this alloy suitable for marine applications. The large solidification range along with complicated and numerous phase formation reactions of this alloy generated a multitude of microstructures and properties in its laser-deposited coatings. Such variations and their underlying mechanisms are discussed in CHAPTER 4. An important part of this research was application of various electron microscopy characterization techniques. This subject is also explained in detail in CHAPTER 4 and used frequently in the subsequent chapters.

Laser-deposited Colmonoy 69 coatings not only suffered from microstructural instability, but even more importantly were very susceptible to cracking. Analysis of microstructural aspects of the cracking process revealed the important contribution of Cr-rich precipitates to crack propagation. Hence, a new direction was set for the project aiming at improving the toughness of Ni-Cr-B-Si-C alloys by refining the Cr-rich precipitates while preserving their hardness. To realize this goal, a number of compositional modifications on Colmonoy 69 were done by addition of vanadium, zirconium or niobium. The results of these compositional modifications will be presented in CHAPTER 5. Among the additional elements, niobium was the magic one. It eliminated the microstructural variations, dramatically refined the microstructure and preserved the high hardness of Colmonoy 69 alloy. With such a combination, the Nb-modified Colmonoy 69 coatings were further studied to check whether

microstructural refinement was a viable toughening mechanism for Ni-Cr-B-Si-C alloys or not. The correlation between microstructural refinement and cracking behavior of the laser-deposited coatings will also be discussed in CHAPTER 5.

As deposition of crack-free coatings from hard Ni-Cr-B-Si-C alloys over realistically large areas (necessary for the final application) proved to be very difficult even after preheating the substrate up to 650 ^{o}C, the focus was shifted to other Ni-base alloys such as Colmonoy 33 or Nucalloy 488V. CHAPTER 6 reports on the microstructure and corrosion/wear performance of laser-deposited dilute Ni-base alloys. This chapter culminates in development of a new Ni-base hardfacing alloy with a preferable combination of hardness, toughness and superior functional properties in comparison to those of the existing commercial alloys. The new alloy is capable of producing excellent laser-deposited coatings for piston rods intended for extreme working conditions. Finally, CHAPTER 7 summarizes the outcomes of this work and provides an outlook for future works.

References

1. Ion, J. C. *Laser Processing of Engineering Materials: Principles, Procedure and Industrial Application*; Elsevier: Boston, 2005.
2. Toyserkani, E. *Laser Cladding*; CRC Press: Boca Raton, Fl, 2005.
3. Ocelík, V.; Hosson, J. T. M. De Thick metallic coatings by coaxial and side laser cladding: processing and properties. In *Advances in laser materials processing technology*; Woodhead Publishing Ltd. and CRC Press: Oxford (UK)-West Palm Beach (USA), 2010; pp. 426–458.
4. Beyer, E. New Industrial Systems & Concepts for Highest Laser Cladding Efficiency http://www.lia.org/blog/2011/05/high-performance-laser-cladding/ (accessed Feb 18, 2013).
5. Wang, D.; Liang, E.; Chao, M.; Yuan, B. Investigation on the Microstructure and Cracking Susceptibility of Laser-clad V2O5 /NiCrBSiC Alloy Coatings. *Surface and Coatings Technology* **2008**, *202*, 1371–1378.
6. Hemmati, I.; Ocelík, V.; Hosson, J. T. M. De Dilution Effects in Laser Cladding of Ni–Cr–B–Si–C Hardfacing Alloys. *Materials Letters* **2012**, *84*, 69–72.
7. Kannatey-Asibu, E. *Principles of Laser Materials Processing*; Wiley series on processing of engineering materials; Wiley: Hoboken, N.J, 2009.
8. Thermal Coatings http://www.iws.fraunhofer.de/content/dam/iws/en/documents/publications/business_field_brochures/Info_4e_GF_NOW_BER_Therm_Besch.pdf.
9. Sulzer - Component Manufacturing and Repair http://www.sulzer.com/en/Products-and-Services/Coating-Services/Laser/Component-Manufacturing-and-Repair (accessed Apr 5, 2013).
10. Laser Cladding Services - Product Enhancement http://www.lasercladding.com/enhancement.html (accessed Apr 5, 2013).
11. Examples for Cladding - Laserline USA http://www.laserline.de/laser-cladding-examples.html (accessed Apr 5, 2013).
12. Chang, S.-S.; Wu, H.-C.; Chen, C. Impact Wear Resistance of Stellite 6 Hardfaced Valve Seats with Laser Cladding. *Materials and Manufacturing Processes* **2008**, *23*, 708–713.
13. Adachi, S.; Horio, K.; Nakamura, Y.; Nakano, K.; Tanke, A. Development of Toyota 1ZZ-FE Engine. In *New engine design and automotive filtration*; Society of Automotive Engineers: Warrendale, Pa, 1998.
14. Laser Cladding Brochure - Fraunhofer IWS http://ilt.fraunhofer.de/eng/ilt/pdf/eng/products/LaserCladding.pdf (accessed Apr 18, 2013).
15. Irepa Laser http://www.irepa-laser.com/ (accessed Apr 5, 2013).
16. Hunt, T. M. *The Hydraulic Handbook*; 9th ed.; Elsevier Advanced Technology: Kidlington, Oxford, UK, 1996.
17. Haukas-Eide, O.; Fischer, K. P.; Lønvik, K. Guideline for material selection and qualification of wear and corrosion protective hard face coatings for piston rods. In *Proceedings of "Corrosion 2007" conference*; NACE: Nashville, TN, 2007; paper #07694.
18. Said, B. A Brief Overview of Corrosion-resistant Piston Rod Coating Technology http://www.eaton.com/ecm/groups/public/@pub/@eaton/@hyd/documents/content/pct_298624.pdf (accessed Apr 8, 2013).

19. Haukas-Eide, O.; Fischer, K. P.; Lønvik, K. Qualification of Wear and Protective Surface Coating for Hydraulic Piston Rods. In *Proceedings of "Corrosion 2006" conference*; NACE: San Diego, CA, 2006, paper #6026.
20. LASERTEK Piston Rod Coating http://www.doucehydro.com/index.php?mod=5&id=26 (accessed Apr 8, 2013).
21. Laser Cladding Applications - Innoteq GmbH http://www.innoteq.de/application.php?sub=2 (accessed Apr 8, 2013).
22. Laser Cladding Services - Praxair Service Technologies http://www.praxairsurfacetechnologies.com/na/us/pst/pst.nsf/AllContent/72B0BFC48C875ABB852576A50056C2ED?OpenDocument&URLMenuBranch=D5835AF016E87136852576A50076AC49 (accessed Apr 8, 2013).
23. Aludra - Wear-Resistant Thermal Spray Coatings http://www.aludra.nl/15/wear-resistant-thermal-spray-coatings.html (accessed Apr 9, 2013).
24. Carpenter Technology http://www.cartech.com/ (accessed Apr 9, 2013).
25. Haynes International, Inc. ULTIMET® Alloy http://www.haynesintl.com/ultimetalloy/UltimetAlloyPF.htm (accessed Apr 9, 2013).
26. Zhong, M.; Liu, W. Laser Surface Cladding: The State of the Art and Challenges. *Proceedings of the Institution of Mechanical Engineers, Part C: Journal of Mechanical Engineering Science* **2010**, *224*, 1041–1060.
27. *Rapidly Solidfied Alloys: Processes, Structures, Properties, Applications*; Materials engineering; M. Dekker: New York, 1993.
28. Kurz, W.; Trivedi, R. Rapid Solidification Processing and Microstructure Formation. *Materials Science and Engineering A* **1994**, *179-180*, 46–51.

Chapter 2

DEPOSITION AND CHARACTERIZATION TECHNIQUES

2.1 Introduction

AS explained in CHAPTER 1, the focus of this work is on understanding the processing-microstructure-properties relations in the laser-deposited coatings. In order to establish such relations, a wide range of microstructural characterization and phase identification techniques as well as testing methods to evaluate mechanical properties and corrosion resistance of the samples were employed. In this chapter, the laser cladding set-up and some of the analytical techniques and devices used to characterize the laser-clad coatings will be discussed.

2.2 Laser cladding set-up

A set-up consisting of a high power fiber laser, a twin-hopper powder feeder and a cladding station was used to deposit the samples of this work. Figure 2.1 shows the YLS-3000 laser machine from IPG Photonics and the Twin 10C powder feeder from Sulzer Metco. The YLS-3000 laser machine has an ytterbium doped fiber laser source which generates 500-3000 watts of laser power with the wavelength of 1070-1080 nm at a wall-plug efficiency of more than 30%. The operating range of this machine is from 10% of the minimum power to the full power without change of beam quality or profile[1]. The

generated beam was transported to the cladding station using an optical fiber with a diameter of 600 μm. The laser power and its rate of change were adjusted by control software of the laser machine as well as using Lompoc Pro software from Fraunhofer IWS[2].

The Sulzer Metco Twin 10C is a precision powder feeding system with two hoppers and on-board powder heating system. The powder is stirred and/or heated in the hoppers and subsequently transported to the point of application using a carrier gas, e.g. argon. The two hoppers of the machine could be operated and controlled independently which allows injecting two different powders. This capability was used in this research for compositional modification of commercially-available alloys as will be discussed in CHAPTERS 5 and 7. The powder feeding rate of Twin 10C is 2-150 g/min[3] and could be controlled either manually or using the CNC program. The same program controlled movements of the table and laser head as well as the flow rate of the melt pool shielding and powders carrier gases (both argon).

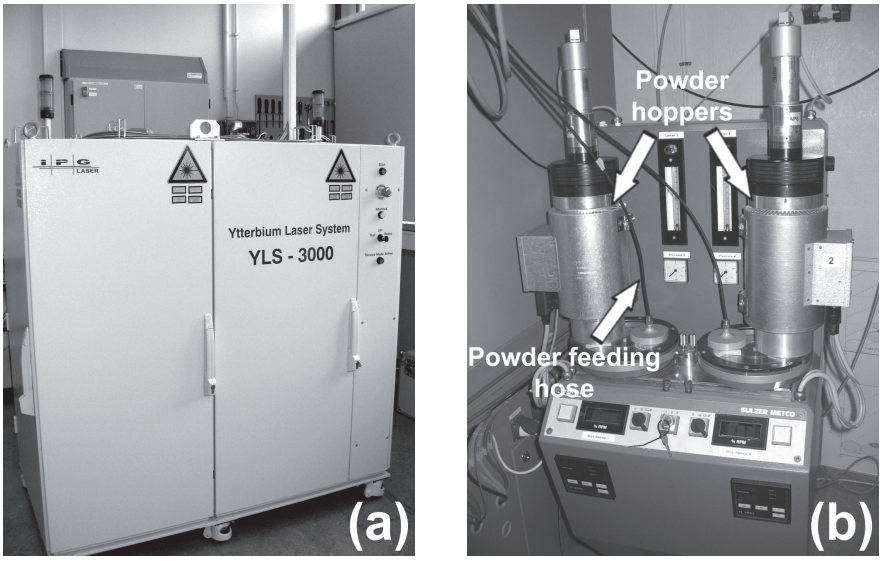

Figure 2.1. (a) Fiber laser machine, and (b) powder feeder used in this work.

Figure 2.2 shows the laser cladding station. The optical fiber carrying the laser beam was connected to a lens system consisting of collimator and focusing lenses. The deposition experiments were done using Cu-based side-cladding powder injection nozzles from ALOtec Dresden GmbH (Germany)[4]. The steel substrate bars were mounted on the CNC spindle head and rotated during experiments. A 4-axes CNC table was used to manipulate the substrate

and the laser head. In some experiments, the substrate bar was preheated using an electric tube furnace immediately before deposition. The same furnace was used for controlled cooling of the deposits. Temperature of the preheated bars was measured by the infrared pyrometer connected to the laser head as well as a hand-held pyrometer.

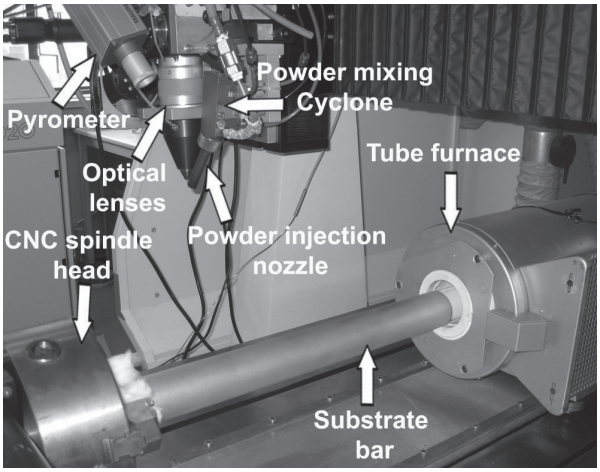

Figure 2.2. Laser cladding station.

2.3 Characterization techniques

In this research, two groups of characterization techniques were used to observe the microstructure/identify the constituent phases or to assess functional properties of the deposits. The first category included X-ray Diffraction (XRD) and various microscopy or microscopy-based techniques such as Optical Microscopy (OM), Scanning Electron Microscopy (SEM), Transmission Electron Microscopy (TEM), Energy Dispersive Spectroscopy (EDS), and Electron Backscatter Diffraction (EBSD). A combination of these techniques was used to characterize the coatings' microstructure and phases in various length scales ranging from bulk (XRD) to micrometer (SEM-based techniques) and finally sub-micrometer (TEM). The second category was concerned with testing the mechanical (bulk and surface) and corrosion properties of the coatings and included Vickers microhardness and indentation measurements, dry sliding wear test, slurry erosion test, Open Circuit Potential (OCP) and Electrochemical Impedance Spectroscopy (EIS). Detailed description for each technique could be found in several textbooks[5–11]. A list of the experimental devices used in this work is provided in Table 2.1. More

details about slurry erosion and corrosion testing facilities will be presented in this chapter. For further details about the rest of the equipments, the readers are referred to the website of Materials Science Group of University of Groningen (www.materials-science.phys.rug.nl). In the remaining of this section, significance of some of the above-mentioned techniques in the context of the current work will be discussed using a number of examples.

Table 2.1. List of experimental equipments employed in this work.

Equipment	Specification
Metallographic preparation	Struers grinding and polishing machines and consumables
OM	Olympus VANOX-T
SEM	Field Emission Gun Philips FEI XL-30
EDS	EDAX with SUTW+ detector
EBSD	TSL OIM system with digital camera
TEM	Field Emission Gun JEOL JEM 2010F (200 kV) with EDS
XRD	Bruker D8 Advance
Hardness	CSM Revetest Scratch tester
Dry sliding wear	CSM Tribometer
Slurry erosion tester	Pot-type testing set-up (TNO, Eindhoven)
Corrosion tester	EIS testing set-up (TNO, Den Helder)

2.3.1 Application of combinatorial microscopy techniques

Combination of different microscopy techniques proved to be very helpful and even necessary to truly characterize the microstructures and their evolutions, constituent phases, crack growth paths, hardness variations, etc. in the studied coatings. In this section, some examples of such combinatorial studies will be presented.

2.3.1.1 Different imaging modes in SEM

Both of the main imaging modes in SEM, namely Secondary Electron (SE) and Backscatter Electron (BSE) were used for microstructural observation and phase identifications. The image contrasts in SE and BSE modes are generated by the surface topography and differences in atomic number, respectively[5,6]. While imaging in SE mode was useful to study the fracture surfaces, majority of the SEM characterizations were performed in BSE mode

which made it easy to find and observe the boride and carbide precipitates. In some cases as shown in the example of Figure 2.3, finding these precipitates in SE mode was almost impossible. Figure 2.3 shows the microstructure of Zr-modified Colmonoy 69 (CHAPTER 5) which was observed to find Zr-rich phases for subsequent identification by EBSD. It can be seen that the submicron Zr-rich phases which are clearly visible as bright particles in the BSE image are very difficult to find in the SE image. Most of the alloys studied in this work had a similar phase constitution with numerous boride and carbide precipitates. Using the BSE imaging mode or combining it with SE mode wherever useful, proved to be a very powerful technique in revealing the true microstructure of the Ni-base hardfacing alloys of this work.

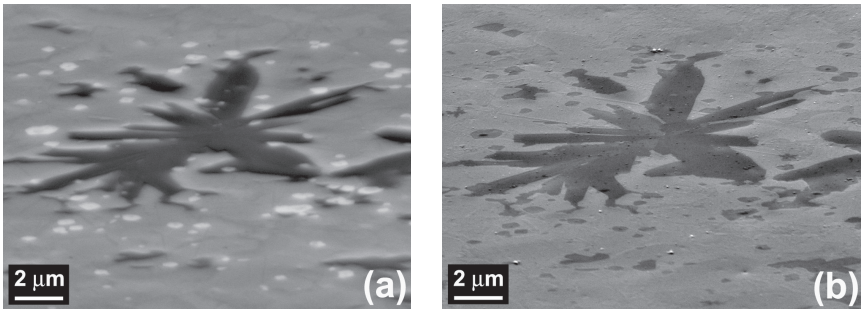

Figure 2.3. SEM images (taken at 70 ^{o} tilt angle for EBSD analysis) of the microstructure of a Zr-modified Colmonoy 69 coating in (a) BSE and (b) SE imaging modes. Zr-rich phases are visible as bright particles in (a).

2.3.1.2 EDS/EBSD phase identification

Identification of the constituent phases was an essential part of this research. In most cases, the target phases were micron-sized boride and carbide precipitates. In addition, a characterization method capable of analyzing selected areas anywhere in the sample (in millimeter range) was needed to study the microstructural variations. To identify any crystalline phase, two sets of information are required[7]: composition and crystallography. Using the compositional information from EDS as an input for EBSD crystallographic analyses, the type, grain structure, orientation relationships with other phases, etc. could be determined. Full details on how to combine EDS and EBSD will be presented in CHAPETR 4. Furthermore, several examples of EDS/EBSD analyses to identify phases and study the phase transformations will be discussed in CHAPTERS 4-6. Examples of using EDS or EBSD alone for

quantitative compositional analysis or study of the grain structure and orientation relationships will also be presented and discussed.

2.3.1.3 Studying the crack growth path

Cracking is a big issue in laser-deposited Ni-base hardfacing coatings[12]. In order to tackle this problem, understanding the microstructural aspects of crack nucleation and growth, i.e. the way different phases and microstructural features contribute to the cracking process is essential. Observation of crack growth paths in conjunction with the information on the type of phases (obtained by techniques such as EDS/EBSD combination) could provide a great deal of data about the cracking process and its microstructural aspects. It was mentioned before that revealing the true microstructure of the intended coatings required the usage of multiple observation methods. A similar approach was necessary to understand the origins of the cracking process. Although BSE imaging in SEM was very useful for microstructural observation, it was not able to reveal the true nature of crack growth in Ni-base coatings. Figure 2.4 shows the BSE image of a crack in Colmonoy 69 samples. While BSE image cannot provide an explanation for the tortuous crack path, OM image of the same area clearly shows how cracks not only grow through the precipitates (the dark phases in the BSE image), but also through the eutectics. In addition, the contribution of Ni dendrites to crack deflection and bridging could also be observed only in the OM image.

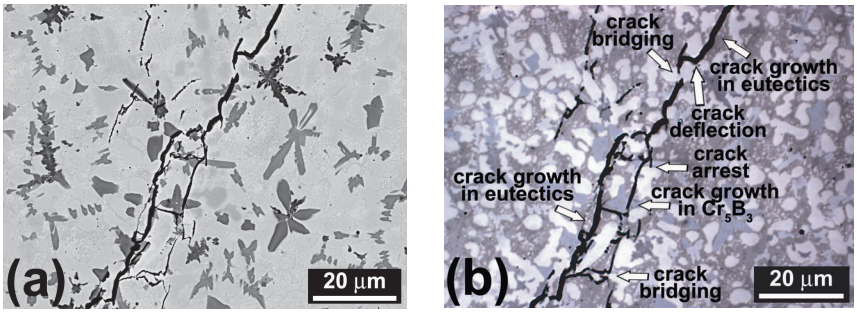

Figure 2.4. Observation of crack growth path in a Colmonoy 69 deposit by (a) SEM-BSE and (b) OM.

2.3.2 Analysis of functional properties

The coatings of this work were intended for wear or corrosion/wear applications. For all coatings, Vickers hardness was measured. Furthermore,

resistance of the coatings against different modes of wear including dry sliding and slurry erosion and against corrosion from seawater was evaluated.

2.3.2.1 Hardness measurements

Hardness is one of the most important general characteristics of engineering materials. It is easy to measure and yet provides useful information about strength, toughness and wear resistance of materials[9]. In this work, microhardness of coatings deposited from different alloys was measured using Vickers technique[13]. In addition to evaluating the overall hardness of the coatings as an important functional property, variations of hardness for multiple microstructures of the same alloy, effects of dilution from the substrate and characteristics of different phases and microstructures were studied by local hardness measurements as shown in Figure 2.5. More details will be discussed in CHAPTERS 4 & 5. Furthermore, Vickers indentation at higher loads was used to evaluate the toughness of Colmonoy 69 as will be explained in CHAPTER 5.

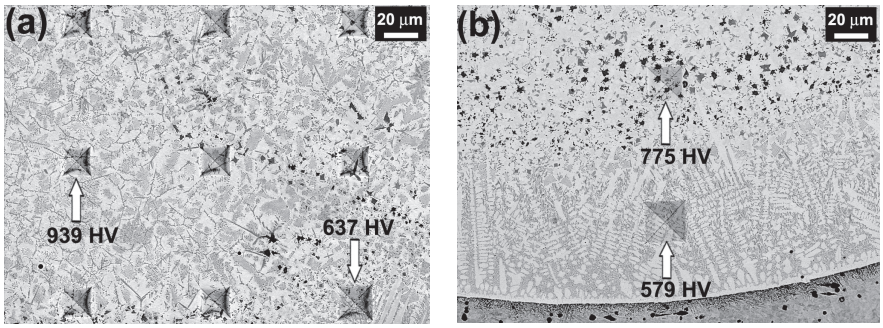

Figure 2.5. Effects of microstructural variations and dilution on hardness of Colmonoy 69 clad layers.

2.3.2.2 Dry sliding wear test

A pin-on disk configuration was used to study the dry sliding wear resistance of laser-deposited AISI 431 stainless steel coatings (CHAPTER 3). In this test, a pin with the laser clad layer at one end machined into a semicircle profile was loaded with a precise force onto a sliding hardened steel disk as shown in Figure 2.6. The pin was mounted on a stiff lever, designed as a frictionless force transducer. As the disc rotated, the resulting frictional forces between the pin and the disc were measured by very small deflections of the lever. The friction coefficient was determined during the test by measuring the deflection

of the elastic arm. Wear coefficients for the pin and disk materials were calculated from the volume of material lost during the test. Wear behavior for both the pin and the disk can be analyzed by measuring the respective volume loss during a specific friction run. The CSM Revetest Tribometer allows the user to perform the tests with varying time, load, sliding velocity, temperature, humidity, atmosphere, lubricants, etc. to simulate the real conditions of practical wear applications[14]. In this work, tests were done without lubricant and at room temperature according to ASTM G99 standard.

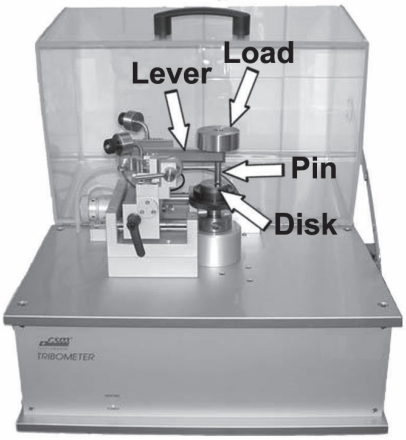

Figure 2.6. Configuration of dry sliding wear test using CSM Revetest machine.

2.3.2.3 Slurry erosion test

The Ni-base laser clad coatings for hydraulic piston rods of the dredging ships are intended to work in a marine environment with solid erodent particles impinging on their surface. Erosion test using slurry of sand particles in water is a relatively realistic test for such a working condition. An in-house built pot-type slurry erosion test set-up at Materials Performance & Tribology department of TNO research institute in Eindhoven (The Netherlands) was used to perform the slurry erosion tests. The essential part of the equipment was the sample holder shown in Figure 2.7. It consists of two stainless steel disks which carry four sample holders, two test samples and two C22 steel reference samples. The disks are driven by electric motor so that they rotate in opposite directions inside the pot. Cylindrical test samples with a diameter of 10 mm are mounted in holders and immersed in silica sand-water mixture. Movement of the disks in opposite directions generates turbulence and creates a homogenous mixture. The angle of sample holders can be adjusted to

control the impact angle of the particles. The erosion wear rate is calculated based on amount of the lost material in a specific period of time[15].

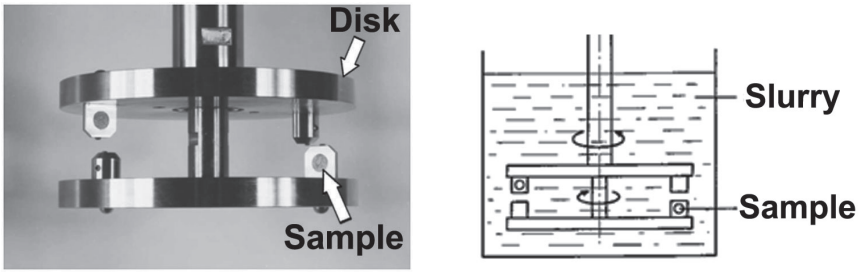

Figure 2.7. Slurry erosion test set-up.

2.3.2.4 Corrosion test

Electrochemical impedance spectroscopy (EIS) can provide a great deal of information about the corrosion behavior of coatings. In EIS measurements, a sinusoidal AC potential $E_t = E_o \sin(\omega t)$ is applied in which E_o is amplitude of the signal, and ω the radial frequency (rad/s). ω can be related to frequency f (hertz) as $\omega = 2\pi f$. The resultant current $I_t = I_o \sin(\omega t + \Phi)$ is shifted in phase by Φ and has amplitude of I_o as shown in Figure 2.8. Analogous to Ohm's law, impedance of the system (Z) can be calculated as $Z = \frac{E_t}{I_t} = \frac{E_o \sin(\omega t)}{I_o \sin(\omega t + \Phi)} = Z_o \frac{\sin(\omega t)}{\sin(\omega t + \Phi)}$. The impedance is therefore expressed in terms of the magnitude Z_o and phase shift Φ. There are different methods to represent the EIS data including Nyquist and Bode plots. In this work, the EIS data will be presented as Bode plots in which impedance is plotted with log frequency on the X-axis and Z_o or Φ on the Y-axis[11,16].

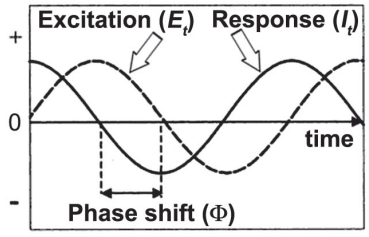

Figure 2.8. Schematic sinusoidal potential excitation and the resultant response in EIS measurements[16].

The impedance data reflects reactions and mass transfer across the electrochemical interface (ECI). Interpretation of EIS data is usually done using an 'Equivalent Circuit' (EC) that models the electric characteristics of the electrode/solution ECI. The EC consists of components such as resistors and capacitors or more complex frequency-dependant components. The theoretical impedance of the proposed circuit can be derived as a multivariable function. By adjusting the variables, a fit of theoretical spectrum to the experimental one within the frequency domain could be achieved. Then, the information regarding electrochemical corrosion can be extracted through appropriate interpretation of the variables. Since the perturbing AC potential is very small, the resultant polarization of the electrode is in the linear potential region. Therefore, impedance spectroscopy is a non-destructive technique and so can provide time-dependent information about ongoing processes such as corrosion reactions[17].

The EIS measurements on some of the Ni-base deposits were done in a Faraday cage at two positions on each of the laser clad and machined rods using a three electrode cell and Ivium instruments with Ag/AgCl reference electrode (XR820 double junction) and artificial seawater as the solution as shown in Figure 2.9. Before the EIS measurements, Open Circuit Potential (OCP) i.e. potential of the working electrode relative to the reference electrode when no external potential is being applied to the cell was measured[16]. The results of EIS measurements (as well as slurry erosion tests) on laser clad Ni-base coatings will be presented and discussed in CHAPTER 6.

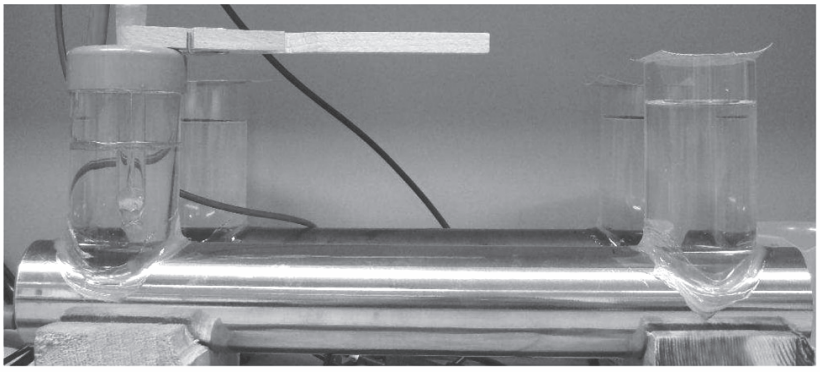

Figure 2.9. The experimental EIS set-up with two cells on each bar.

References

1. IPG YLS Series of Laser Machines http://www.ipgphotonics.com/apps_materials_multi_yls.htm (accessed Apr 16, 2013).
2. Variable Software Control “LompocPro” http://www.iws.fraunhofer.de/en/business_fields/surface_treatment/surface_treatment/products/lompocpro.html (accessed Apr 16, 2013).
3. Dispenser for Powders (volumetric Feeder) - TWIN 10-C http://www.directindustry.com/prod/sulzer-metco/dispensers-for-powders-volumetric-feeder-23581-59001.html (accessed Apr 16, 2013).
4. ALOtec Dresden GmbH http://www.alotec.de/index.php (accessed Apr 16, 2013).
5. Amelinckx, S. *Electron Microscopy: Principles and Fundamentals*; VCH: Weinheim, 1997.
6. Leng, Y. *Materials Characterization: Introduction to Microscopic and Spectroscopic Methods*; J. Wiley: Hoboken, NJ, 2008.
7. *Electron Backscatter Diffraction in Materials Science*; 2nd ed.; Springer: New York, 2009.
8. Zschornack, G. *Handbook of X-ray Data*; Springer: New York, 2006.
9. Gilman, J. J. *Chemistry and Physics of Mechanical Hardness*; Wiley series on processing of engineering materials; Wiley: Hoboken, N.J, 2009.
10. Stachowiak, G. W. *Engineering Tribology*; 3rd ed.; Elsevier Butterworth-Heinemann: Amsterdam, 2005.
11. Orazem, M. E. *Electrochemical Impedance Spectroscopy*; The Electrochemical Society series; Wiley: Hoboken, N.J, 2008.
12. Wang, D.; Liang, E.; Chao, M.; Yuan, B. Investigation on the Microstructure and Cracking Susceptibility of Laser-clad V2O5 /NiCrBSiC Alloy Coatings. *Surface and Coatings Technology* **2008**, *202*, 1371–1378.
13. International, ASM *Hardness Testing*; 2nd ed.; ASM International: Materials Park, OH, 1999.
14. Pin-on-Disk Tribometer - CSM Instruments http://www.csm-instruments.com/en/Pin-on-Disk-Tribometer (accessed Apr 16, 2013).
15. Mens, J. W. M.; Gee, A. W. J. de Erosion in Seawater Sand Slurries. *Tribology International* **1986**, *19*, 59–64.
16. Perez, N. *Electrochemistry and Corrosion Science*; Kluwer Academic Publishers: Boston, 2004.
17. Liu, C.; Bi, Q.; Leyland, A.; Matthews, A. An Electrochemical Impedance Spectroscopy Study of the Corrosion Behaviour of PVD Coated Steels in 0.5 N NaCl Aqueous Solution: Part I. Establishment of Equivalent Circuits for EIS Data Modelling. *Corrosion Science* **2003**, *45*, 1243–1256.

Chapter 3

HIGH-SPEED CLADDING OF AISI 431 MARTENSITIC STAINLESS STEEL

In this chapter, effects of increasing the deposition rate up to 117 mm/s on microstructure and properties of AISI 431 martensitic stainless steel coatings are examined. Solidification structures and solid state phase transformation products are investigated using various microscopy techniques as well as using theoretical tools available in the literature. Variations of hardness and dry sliding wear resistance of the coatings are examined and the microstructure-property relationships are established. Faster cooling at higher deposition rates decreased the primary austenite (γ) cell size. In addition, while in the beginning of each solidification step, both delta ferrite and γ could form in similar quantities, γ became the dominant phase as solidification progressed. Extreme refinement of solidification structure increased the amount of retained γ which lowered the hardness and wear resistance of the deposits. This chapter shows that microstructural refinement obtained at higher deposition rates does not necessarily improve the functional properties of the coatings. The final outcome depends very much on strengthening mechanism of the alloy system.

This chapter has been published in the following journal papers:

I. Hemmati, V. Ocelík, J.Th.M. De Hosson, Microstructural characterization of AISI 431 martensitic stainless steel laser-deposited coatings. Journal of Materials Science, 46 (2011) 3405–3414.

I. Hemmati, V. Ocelík, J. Th. M. De Hosson, The effect of cladding speed in phase constitution and properties of AISI 431 stainless steel laser deposited coatings, Surface & Coatings Technology, 205 (2011) 5235-5239.

3.1 Introduction

ONE of the most important characteristics of laser deposition is its ability to produce deposits with refined microstructures, i.e. having features with a decreased structural scale[1–3]. Microstructural refinement in laser deposited coatings happens because of the rapid cooling during solidification and could occur more strongly at higher deposition rates. This characteristic of laser deposition has been reported to improve the functional properties of the deposits, e.g. increasing their hardness[1,3–5]. As a result, there has been an impetus for increasing the deposition rate of laser cladding to produce coatings with improved functional properties. Other benefits such as decreasing the processing time and improving the energy efficiency of the process have also been mentioned for high-speed laser cladding[6,7].

In this chapter, the results of depositing AISI 431 martensitic stainless steel on AISI 304 austenitic stainless steel rods at cladding speeds up to 117 mm/s are presented. AISI 431 is a low carbon high chromium steel which provides a good combination of hardness, toughness and corrosion resistance[8]. This alloy is a good candidate for improving wear resistance of austenitic stainless steels being extensively used for structural components in corrosion applications such as hydro-turbines, valves and pumps[9–12].

The focus of this chapter will be on whether the idea of microstructural refinement via increasing the cladding speed will improve hardness and wear resistance of an alloy strengthened by formation of martensite. The reason for such a focus is that previous results on beneficial effects of high speed cladding were reported for alloy systems in which size of the constituent phases (e.g. grains or precipitates) was a key factor in determining the properties of the deposits[4,5,13,14]. However, in an alloy system strengthened by martensite, the solid state transformation of austenite (γ) to martensite will finally control the microstructure and properties. The results of this chapter along with those for effects of cladding speed on microstructure and properties of Ni-Cr-B-Si-C alloys (CHAPTER 4) and Inconel 625 (CHAPTER 6) contribute to our understanding of how to predict the possible effects of increasing the cooling rate (e.g. by increasing the cladding speed) on coatings deposited from different alloy systems.

3.2 Experimental procedure

42C powder from Sulzer Metco (equivalent to AISI 431) with particle size of -140 to +325 mesh was deposited on 40-mm-diameter AISI 304 rods. The

laser beam was defocused to obtain a spot size of 3.3 mm in all experiments. Single layer and five layer samples were deposited at scanning speeds of 5, 25, 58 and 117 mm/s. Chemical compositions of the cladding and substrate materials are presented in Table 3.1.

Solidification structure and solid state transformation products were observed by Scanning Electron Microscopy (SEM) as well as Optical Microscopy (OM) after etching with Kalling 1 reagent for 5-10 seconds. Energy Dispersive Spectroscopy (EDS) mapping was employed to analyze the distribution of alloying elements and their possible partitioning. EDS maps of Cr, Ni, Si and Mn were obtained at 20 kV and map of C was collected at 4 kV.

Electron Backscatter Diffraction (EBSD) was employed to measure the percentage of retained austenite and the austenite-martensite orientation relationship (OR). For EBSD characterizations, surface preparation procedure recommended by Struers Co. for EBSD analysis of ferrous alloys was applied[15]. Previous research showed that choosing other crystal symmetries than bcc for indexing martensite EBSD patterns will produce poor results[16]. Consequently, γ and ferrite (α) were included as the constituent phases in the EBSD analyses. Ternary phase diagram, Schaeffler and TTT diagrams were also used to analyze the experimental findings.

Mechanical properties were determined using Vickers microhardness measurements (CSM Revetest) and pin-on-disk dry sliding wear test (CSM Tribometer) at room temperature. Pin-shape samples with a 6-mm-diameter hemispheric head were cut from the clad layers using Electric Discharge Machining. Pin samples were cleaned with ethanol in an ultrasonic bath and tested for a distance of 1000 m against a steel disk with hardness of 970 HV at a linear sliding speed of 100 mm/sec while a normal force of 10 N was being applied. Prior to the test, the disk was polished to a mirror-like finish. The wear volume was calculated for a spherical cap using *Eq. 3.1* [17]:

$$V = \frac{\pi d^4}{64R} \qquad \textit{Eq. 3.1}$$

where V is the worn volume, d diameter of the wear scar and R radius of the wear sample tip (3 mm in our case). The wear rate, K defined as the worn volume (V) per unit sliding distance (L) and applied force (F_N) was determined using *Eq. 3.2*:

$$K = \frac{V}{L.F_N} \qquad \textit{Eq. 3.2}$$

Table 3.1. Nominal composition of coating and substrate materials (wt.%)[8].

Alloy	C	Mn	Si	Cr	Ni	Fe
AISI 431	0.2	1	1	15-17	1.25-2.5	Bal.
AISI 304	0.08	2	1	18-20	8-10.5	Bal.

3.3 Results

3.3.1 Solidification structure

Figure 3.1 shows the three distinct microstructures which could be identified in the deposits. A thin layer of planar growth was present at all clad-substrate interfaces with an extension of around 20 μm. This plane growth zone became unstable as solidification proceeded and broke down into cellular dendrites within short distances from the interface. In multi-layer samples, dendrites with epitaxial growth across track interfaces (Figure 3.1(b) and Figure 3.1(c)) formed the majority of solidification microstructures. Finally, a Columnar to Equiaxed Transition (CET) occurred at the top of the deposits resulting in a thin layer of equiaxed grains (Figure 3.1(d)).

The observed microstructural changes can be explained by variations of G (temperature gradient in the melt) and V_n (component of the growth velocity normal to the solid-liquid interface) as discussed in CHAPTER 1. The G/V_n ratio determines the solidification mode and the $G*V_n$ controls scale of the solidified structure (Figure 3.2)[18]. During laser deposition, decrease in G/V_n from bottom to top of the melt pool can change the solidification structure from planar to cellular and then columnar and equiaxed dendrites[18]. Furthermore, heat accumulation during multi-layer laser claddings decreases the temperature gradient in the melt pool[19,20] which provides the opportunity for CET as shown in Figure 3.1.

Increasing the solidification rate did not affect the microstructural features such as epitaxial growth or CET. But the cellular dendritic structure was significantly refined as visible in Figure 3.3. Higher cladding speeds produced smaller cell spacing sizes down to around 9 μm in five-layer and 3 μm in single layer deposits. This can be explained by the fact that growth rate is a direct function of cladding speed and higher growth rates are obtained at higher deposition velocities (CHAPTER 1). A variation of 15% is included in

the data of Figure 3.3 to account for changes in cell spacing from bottom to top of the coating because of local variations in solidification conditions[21]. The difference in the cell spacing values of single and multi-layer deposits, despite their similar cladding speeds, can be attributed to the heat accumulation in multi-layer claddings. In both cases, cell spacing size followed the empirical power law of $\sim V_n^{-0.5}$ reported previously[21].

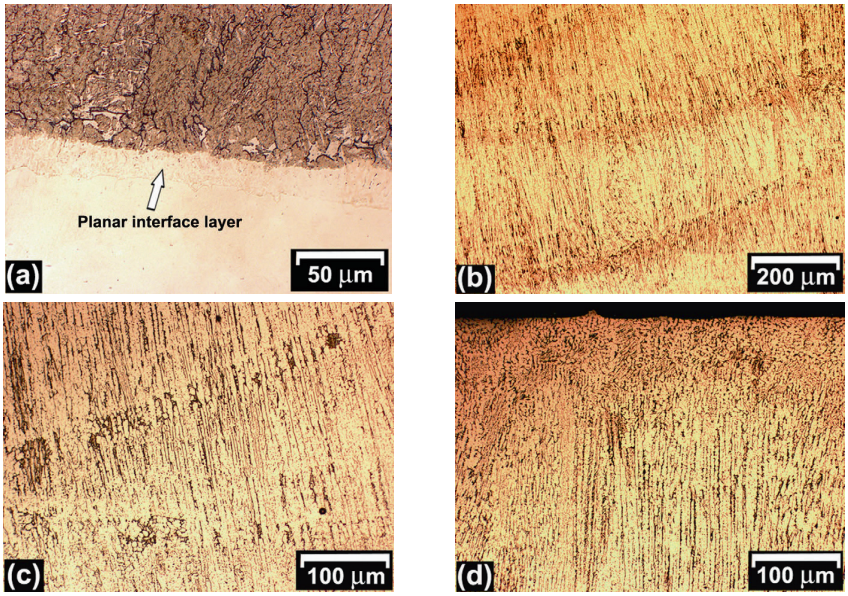

Figure 3.1. Solidification structures revealed by OM: (a) planar growth at substrate-coating interface, (b) dendritic structure with epitaxial growth (c) closer view of epitaxial growth across track interfaces, and (d) CET at top.

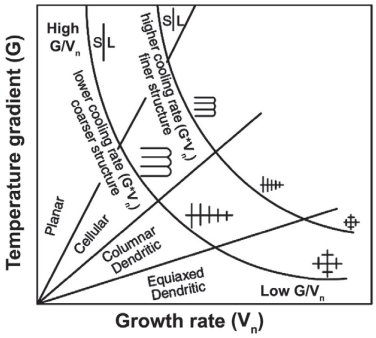

Figure 3.2. Effect of G and V_n on morphology and size of solidification structures[18].

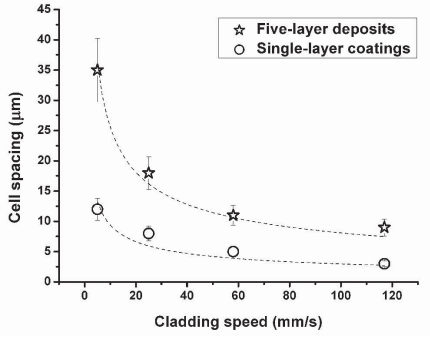

Figure 3.3. Effect of cladding speed on cell spacing in single- and multi-layer deposits. Dashed lines show the graph for $V^{-0.5}$.

3.3.2 Solidification phases

The connection between chemical composition of stainless steels and their equilibrium phase constitution can be obtained by tools such as Schaeffler and ternary phase diagrams. Figure 3.4(a) locates the composition of AISI 431 alloy on Schaeffler diagram[22]. Also, position of AISI 431 on a section of ternary Fe-Cr-Ni phase diagram at the latest stage of solidification (1400 ^{o}C) calculated by *Ternary Phase Diagrams* software from Japan Science and Technology Corporation is shown in Figure 3.4(b). A dilution of around 10% from substrate was taken into account for calculating the position of AISI 431 on the above-mentioned diagrams. Dilution from the austenitic stainless steel substrate increases the Ni content and slightly decreases the C content in the clad layer. As a result, the values of equivalent nickel ($Ni_{eq.}$) and equivalent Cr ($Cr_{eq.}$) are not significantly affected by dilution. Hence, the same position on the diagram could be selected for single and multi layer deposits. Based on these diagrams, equilibrium solidification of AISI 431 produces austenite and around 10% ferrite which finally results in ferrite, martensite and retained austenite at room temperature.

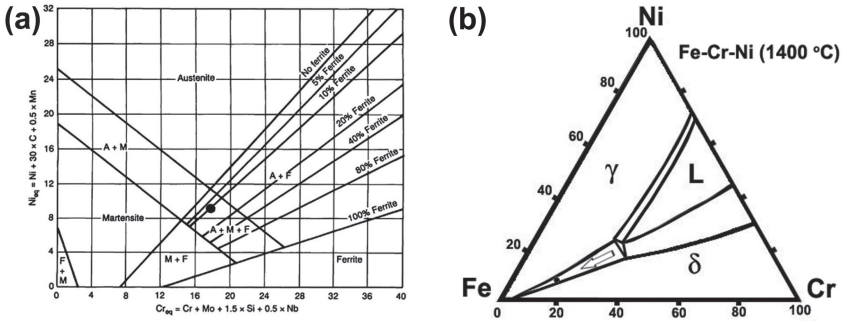

Figure 3.4. Composition of AISI 431 on (a) Schaeffler diagram, and (b) a section of the ternary Fe-Cr-Ni phase diagram as highlighted by the arrow.

While these diagrams are reliable for predicting structures at cooling rates close to equilibrium, previous research[23–26] showed that cooling rate during solidification has a significant effect on the final microstructures of the stainless steels. Thus, the above-mentioned diagrams could not reliably predict the phase constitution of rapidly cooled stainless steels. This unreliability was shown in the current study in terms of the amount and distribution of ferrite in samples deposited at different speeds. Figure 3.5 shows the optical micrographs of the five-layer samples deposited at different speeds. It can be seen, especially at track overlapping areas, that by increasing

the cladding speed, less ferrite (visible as white islands) was formed. In addition, distribution of ferrite is not homogenous. While little amounts of ferrite are present at interdendritic areas, large quantities are formed at the beginning of each solidification step, i.e. at substrate-coating interface or in remelted parts of the previous track (Figure 3.6).

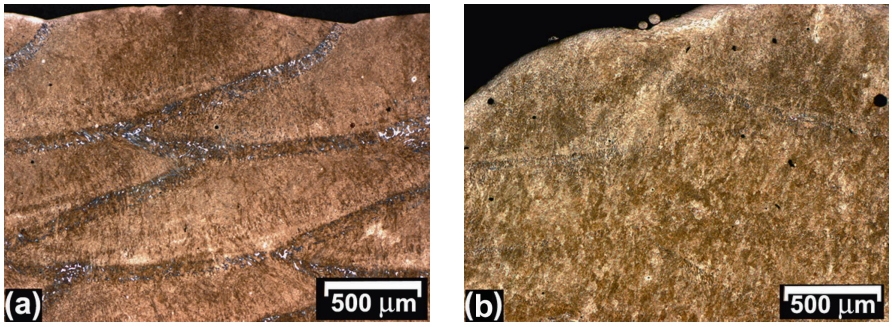

Figure 3.5. Reduction in the amount of ferrite with increasing cladding speed from (a) 5 to (b) 117 mm/s. Ferrite appears as bright island at track interfaces.

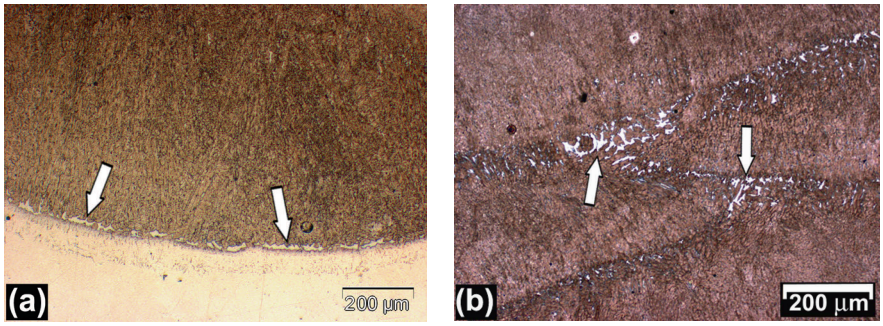

Figure 3.6. Distribution of ferrite (shown by arrows) at (a) substrate-cladding interface and (b) track overlapping areas.

Figure 3.7 shows the EDS maps for Ni, Cr and C (the main alloying elements of AISI 431) at overlapping areas (which contain considerable quantities of both ferrite and transformed austenite). EDS mapping showed that even at the lowest cladding speed, there was no detectable partitioning of alloying elements between these two phases. Uniformity of chemical composition in dual-phase areas suggests that solidification of these coatings occurred in a partitionless manner. This can be explained based on the high cooling rates experienced during the laser deposition process.

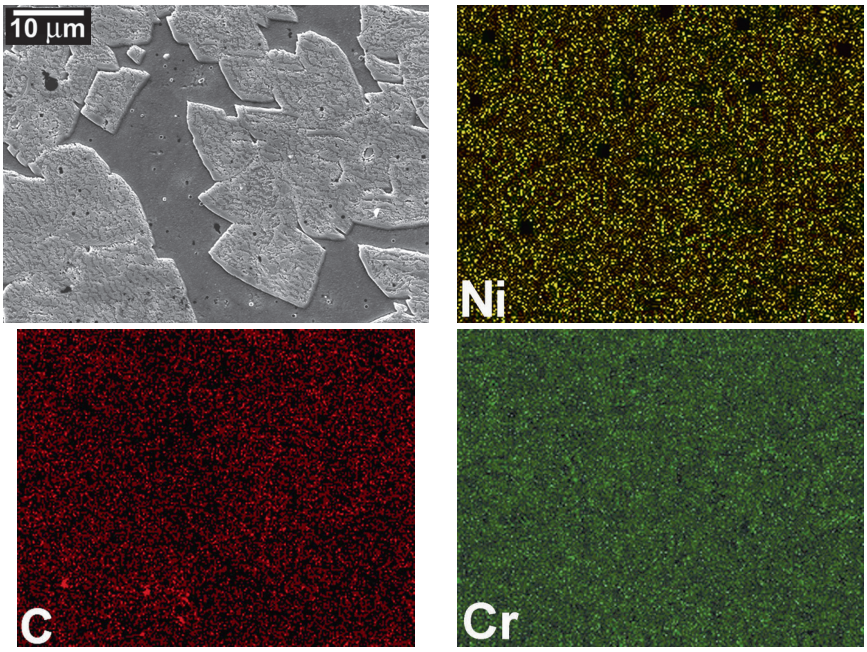

Figure 3.7. SEM image of a dual- phase area in AISI 431 laser deposited coatings along with the EDS maps for Ni, Cr and C in that area.

Taking the partitionless solidification into account, T_o line as shown in Figure 3.8 (and not the liquidus line in equilibrium phase diagram) should be considered as the onset of solidification. T_o line is the loci of T_o temperatures at which the new phase can appear with a net decrease in free energy at the same composition as the parent phase. In fact, T_o line defines the boundary below which diffusionless transformation is possible[27]. Below T_o, free energy of the single phase δ-ferrite or γ will be lower than free energy of the undercooled liquid and partitionless solidification will be theoretically possible[23]. T_o curve is located between the liquidus and solidus lines of the equilibrium phase diagram. In Figure 3.8, the data from references [23] and [26] are combined to show the composition of AISI 431 in the phase diagram with T_o lines. Solidification structure depends on whether the T_o line (or its extension) for γ, δ or both of them is crossed by the undercooled melt and relative quantity of γ and δ is governed by the difference in T_o temperatures of the two phases[24]. As can be seen in Figure 3.8, T_o

temperatures of γ and δ for AISI 431 are very close. It means if the undercooled liquid crosses the T_o lines, both phases will form in similar quantities. This is confirmed by Figure 3.6 which shows that at the beginning of each solidification stage, γ and δ formed in similar proportions. It can be concluded that the undercooling achieved during rapid solidification was sufficient to bring the liquid metal below both T_o lines, thus making it possible for both phase to nucleate. Figure 3.6 also shows that γ quickly outgrew δ and became the primary solidification phase. This can be attributed to the faster growth kinetics of γ in comparison to δ as observed in several previous studies[23,24,28]. It seems that while partitionless solidification provided the opportunity for both γ and δ to nucleate at the initial stages of solidification, the more favorable growth kinetics of γ dominated the rest of the solidification (especially at higher solidification rates) and resulted in a mostly austenitic structure with isolated block of ferrite at the interfaces and occasionally at interdendritic areas.

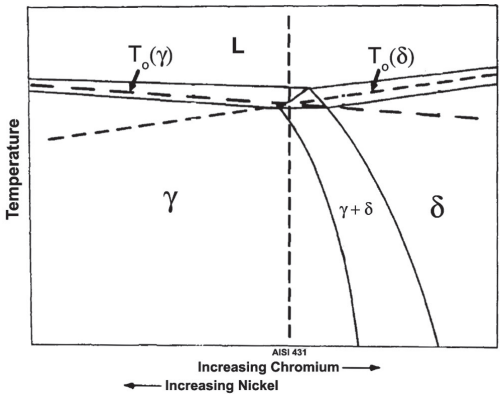

Figure 3.8. Position of AISI 431 composition in ternary phase diagram during partitionless solidification[23,26].

3.3.3 Solid-state phase transformation

3.3.3.1 Microstructural observation

By changing the cladding speed, not only solidification rate changes, but also cooling rate in solid state could be affected which in turn may influence the solid state phase transformations. According to TTT diagram of AISI 431[29],

this type of steel has a very high hardenability and in order to form any transformation product other than martensite, it should take 10^3-10^4 seconds to reach from austenitizing temperature to around 600 ^oC. Under our processing conditions, having such slow cooling rates was virtually impossible. So, only the transformation of austenite to martensite could occur. Microstructural investigation using OM and SEM on samples deposited at different cladding speeds proved that this was the general case and typical lath martensite was the dominant microstructural feature (Figure 3.9).

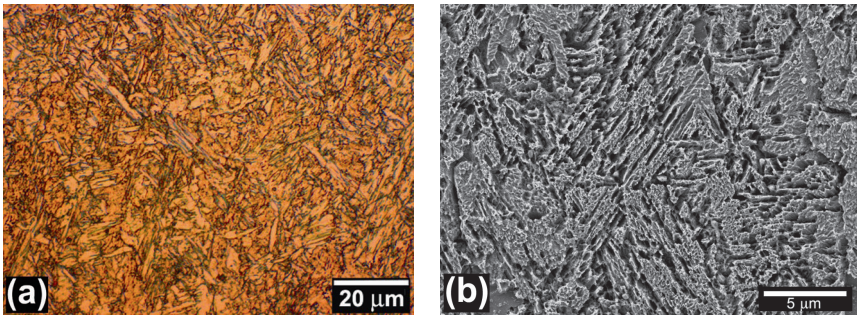

Figure 3.9. Lath martensitic microstructure of the deposits observed by (a) OM, and (b) SEM.

EBSD was employed to analyze the characteristics of solid state transformation products with special interest in quantity of the phases, austenite/martensite OR and austenite/martensite interphase boundaries. Several scans were performed and the results for one of them are shown in Figure 3.10 and Figure 3.11. Figure 3.10shows examples of grain, [001] inverse pole figure (IPF) and phase maps superimposed on image quality (IQ) map of the studied coatings (The image quality parameter or IQ describes the sharpness of an EBSD pattern[30]). Martensite lathes and traces of retained austenite are clearly visible.

3.3.3.2 Quantity of constituent phases

The quantity of martensite and retained austenite were measured by EBSD scans performed on single- and multi-layer coatings deposited at two extreme cladding speeds. Figure 3.11 shows the variations of retained austenite as a function of the cladding speed. It can be seen that while increasing the cladding speed did not significantly affect the amount of retained austenite in the five-layer coatings, the same amount for single-layer coatings was considerably increased. This increase in the content of retained austenite at higher cladding speeds could be correlated to variations of cell spacing sizes

(Figure 3.3). In fact, extreme refinement of the cellular dendrites in single-layer deposits resulted in stabilization of austenite, i.e. a higher percentage of retained austenite. Also, it seems that there is some sort of threshold for the cell spacing size below which stabilization of austenite becomes noticeable. In section 3.4.2 , the mechanism of such stabilization will be discussed.

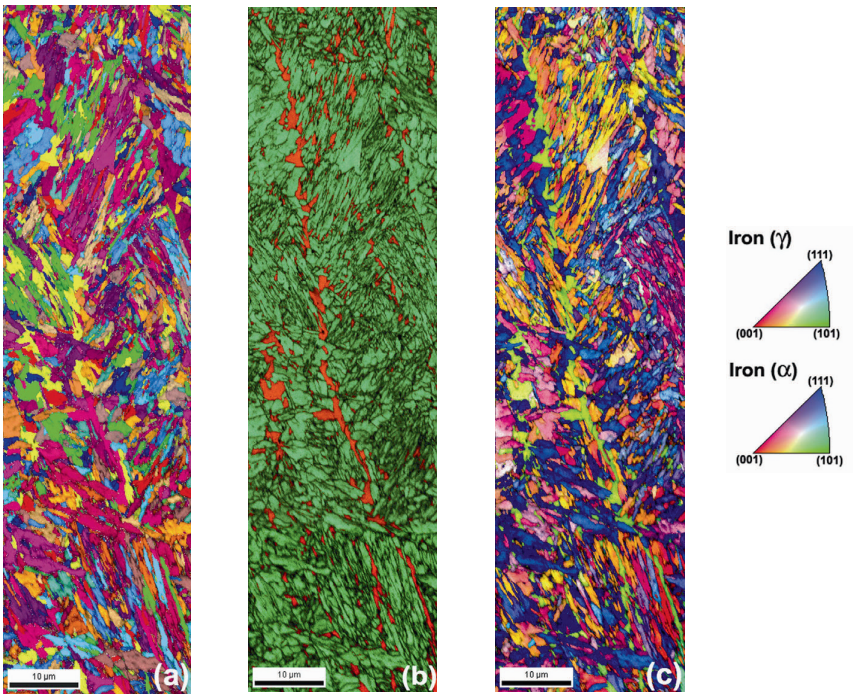

Figure 3.10. Examples of EBSD scan results: (a) grain, (b) phase (martensite: green, austenite: orange) and (c) [001] inverse pole figure (IPF) maps superimposed on image quality (IQ) map.

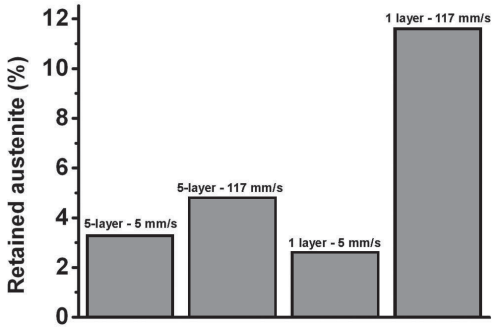

Figure 3.11. Percentage of retained austenite measured by EBSD in single- and multi-layer deposits with lowest and highest cladding speeds.

3.3.3.3 Austenite-martensite phase transformation

As the formation of martensite involves coordinated and collective movement of atoms, parent austenite and product martensite always have some form of orientation relationship. Over the years, several models such as Kurdjumov-Sachs (K-S)[31], Nishiyamam-Wassermann (N-W)[32,33] and Greninger-Troiano (G-T)[34] have been proposed to describe the fcc/bcc OR formed during martensitic transformation. The basic idea in all of these models is that closed-packed planes of the two phases (i.e. {111} for austenite and {110} for ferrite) are parallel or nearly parallel. By confirming the validity of the concept of parallel close-packed planes, it will be reliable to use these models to study the OR in our coatings. To explore this, Pole Figure (PF) texture plots for close-packed planes of austenite and martensite were obtained and compared. As shown in Figure 3.12, it is obvious that the criterion of parallel close-packed planes is valid in our case because the projection of all {111} plane poles for austenite coincides with the projection of some {110} planes for martensite. Having this fundamental concept confirmed, discrete PF plots for different planes of austenite and martensite were obtained and compared with the theoretical PFs for each OR model. The PF plots of the two phases show close resemblance to the PF of G-T model as shown in Figure 3.13.

Usually different austenite-martensite ORs are associated with different values of misorientation across their interphase boundaries[35]. The misorientation across the austenite-martensite boundaries was studies by EBSD to recheck the existence of G-T orientation relationship. Figure 3.14 shows a close-up of an area in the EBSD scan of Figure 3.10 containing both martensite and retained austenite. This section was selected in such a way that it contained only one originally-austenite grain (evident from the inverse pole figure map in Figure 3.14(b)) to avoid considering the γ-γ interfaces in the boundary measurements. By measuring the misorientation angle across the interphase boundary, it was revealed that the two phases are separated by high-angle boundaries with misorientation around 45^{o}. More detailed analysis of misorientation values showed that there was in fact a range of boundary misorientations from 42 to 46^{o} as highlighted in Figure 3.14(d). Highlighting the 42-46 degree boundaries in the whole scan area revealed that this was the general case and almost all of the interphase boundaries were high-angle with misorientations in the range of 42-46^{o} (Figure 3.15). Average misorientation angle between austenite and martensite was 44.27^{o} which is very close to 44.3^{o} misorientation calculated for G-T orientation relationship[35].

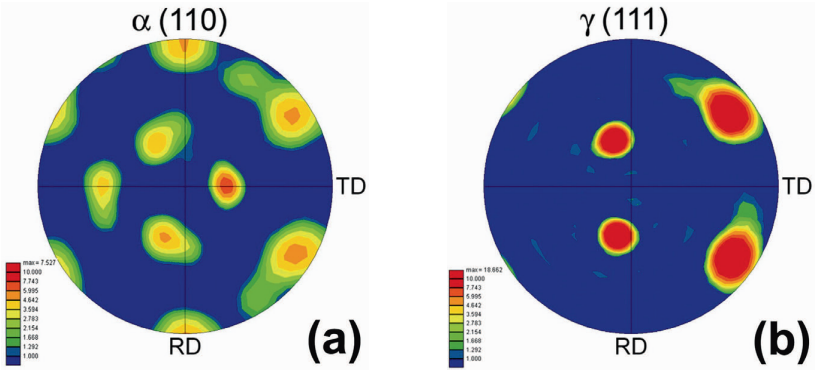

Figure 3.12. PF texture plots for close-packed planes of γ and α. Identical location of all {111} plane poles for γ and some {110} planes for α confirms that theses two sets of planes are parallel.

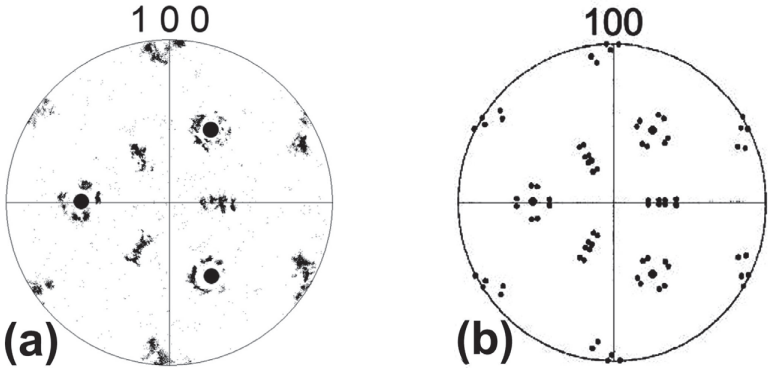

Figure 3.13. (a) (100) PF plot $\gamma + \alpha$ (γ poles are shown by dots) (b) fcc/bcc OR in G-T model. Similarity of (a) and (b) shows the existence of G-T orientation relationship between γ and α in our coatings.

3.3.4 Hardness and wear rate

Figure 3.16 represents the hardness of single and multi-layer samples deposited at different speeds. Hardness of single-layer claddings was more homogenous than that of multi-layer deposits. Furthermore, the wear rates of single and multi-layer samples deposited at the two extreme cladding speeds are presented in Figure 3.17. It is obvious from Figure 3.16 and Figure 3.17 that while the properties of five-layer deposits were not sensitive to the cladding speed, higher deposition rates decreased the hardness and increased the wear rate in single-layer samples. The correlation between hardness and

wear rate can be explained by the inverse relationship between these two properties when the wear mechanism is constant[36]. It should be mentioned that because of the similar set-up and environmental conditions during wear testing, it is reasonable to compare the wear performance of the samples.

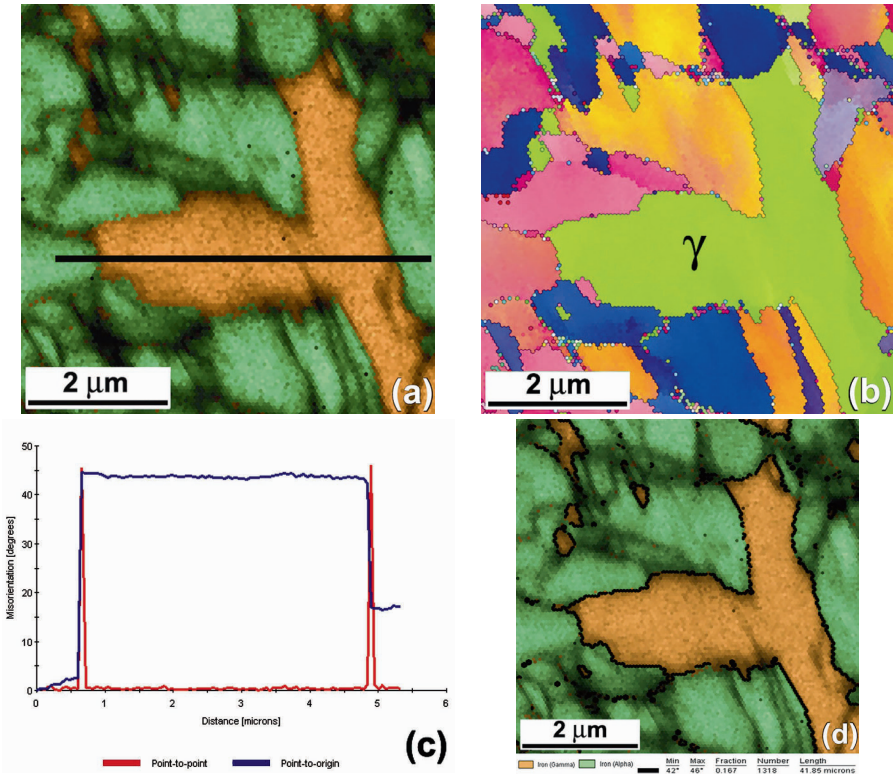

Figure 3.14. (a) A section of the phase map containing martensite and only one austenite grain as shown by the single-orientation (single color) grain of austenite in [001] IPF of (b). (c) Misorientation angle across the line drawn in (a). (d) 42-46 ^{o} boundaries are highlighted.

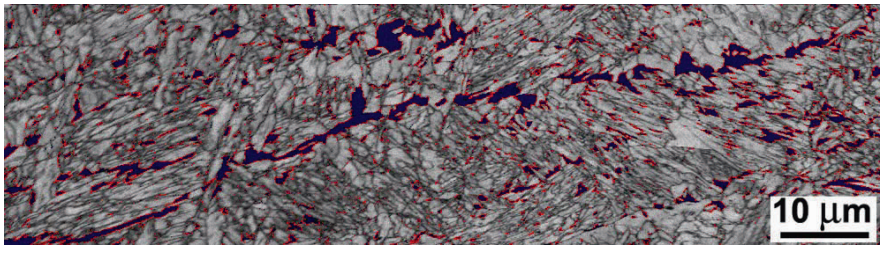

Figure 3.15. 42-46 ^{o} boundaries highlighted in the whole scan area showing that misorientation of nearly all interphase boundaries are in this range.

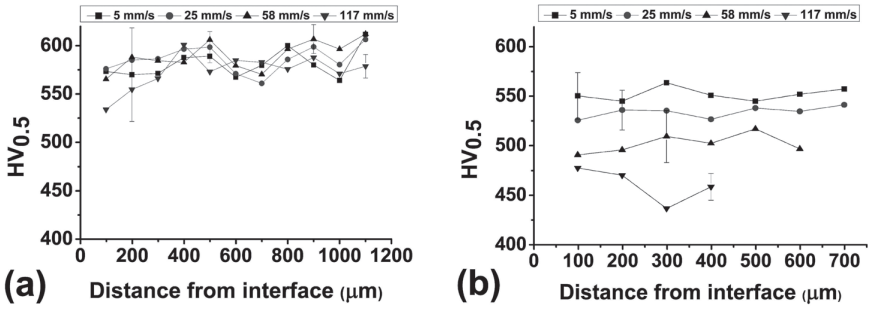

Figure 3.16. Variation of hardness with cladding speed in (a) multi-layer and (b) single-layer deposits. A representative error bar is included for each graph.

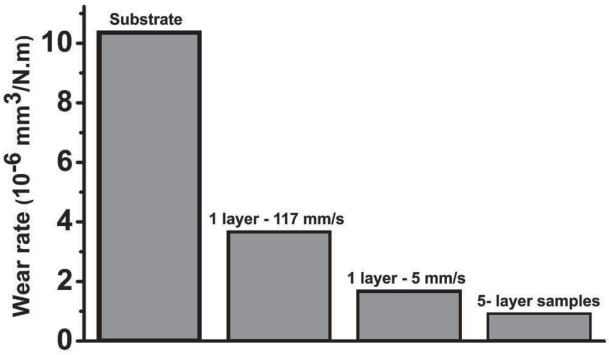

Figure 3.17. Wear rate of substrate, single- and multi-layer samples deposited at different cladding speeds.

3.4 Discussions

3.4.1 Processing-microstructure-properties relationship

As cladding speed was increased, two opposite trends were observed for microstructure/phases and properties of the deposited coatings. Refinement of the dendritic structure and increase in percentage of retained austenite was accompanied by a decrease in hardness and an increase in wear rate. In addition, while the refinement of dendritic structure was generally visible in both single- and multi-layer deposits, noticeable changes in hardness and wear rate were observed only in single-layer coatings with dendritic structures much finer than that of the multi-layer counterparts. This implies that there is a connection between cell spacing and austenite stabilization which shows itself below some threshold.

Although deposition of AISI 431 at higher cladding speeds produced coatings with refined microstructures (i.e. smaller cell spacing sizes) as reported for other alloy systems, functional properties of the coatings were either unchanged or even deteriorated. Reduction in hardness and wear resistance of the coatings could be correlated to higher percentages of retained austenite. As a result, effects of the microstructural refinement on solid-state phase transformation of austenite to martensite should be further analyzed in order to understand the underlying mechanism of the observed processing-microstructure-properties relationship.

3.4.2 Mechanism of microstructural evolution

It is known that during quenching of austenite, transformation to martensite does not start until reaching the martensite start temperature (M_s) and extent of transformation at a certain temperature below M_s depends on the difference between M_s and that temperature[37]. This means that if any parameter is going to affect the extent of martensitic transformation at room temperature, it should affect the M_s temperature. Finer dendritic structure obtained at higher cladding speeds stabilized the austenite, i.e. more austenite was retained. This means that extreme microstructural refinement lowered M_s and delayed the transformation to martensite.

According to the model proposed by Jiang et al.[38], dependence of M_s on austenite grain size could be related to the probability of finding nucleation sites for martensite embryos. This can be described as a function of grain size reciprocal using *Eq. 3.3*:

$$M_s = M_s^c \exp(-\frac{B}{D}) \qquad \textit{Eq. 3.3}$$

where M_s^c is the martensite start temperature calculated based on the alloy composition, B a dimensional constant in μm related to material (≈ 1 for most steels) and D is the value of austenite grain size in μm. Using Andrews equation[39], the M_s of AISI 431 is calculated to be 195 ºC. By plotting *Eq. 3.3* with B =1 and M_s^c = 195 ºC, the graph of Figure 3.18 will be obtained which shows that with austenite grain sizes smaller than around 10 μm, M_s temperature quickly decreases.

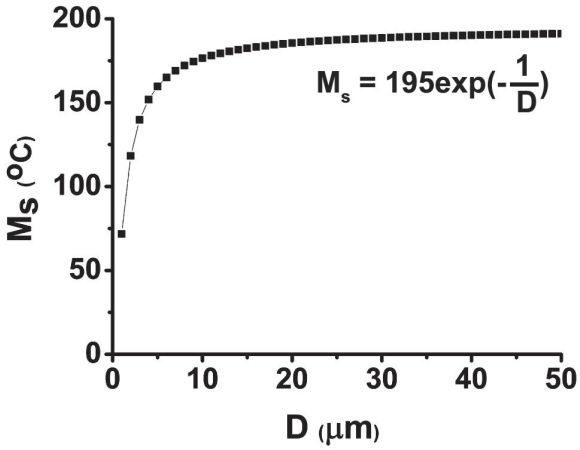

Figure 3.18. Dependence of the M_s temperature of AISI 431 on austenite grain size.

The underlying mechanism of the reduction of M_s in a structure with smaller grain size could be explained by the schematic diagram of Figure 3.19. According to the theory of martensitic transformation[27], the energy barrier (E_b) against formation of a martensitic lath or plate mostly consists of the strain energy required to initiate two types of plastic deformation; a simple shear parallel to the habit plane (the common, coherent plane between austenite and martensite) and a uniaxial expansion (dilation) normal to the habit plane. This means that to initiate the martensitic transformation, austenite should be deformed. Consequently, the yield stress of austenite plays a major role in determining the energy barrier to martensitic transformation. This energy barrier is the strain energy necessary to reach the required level of plastic deformation and will be more for austenite with a higher yield stress.

Several researchers have reported and explained the reduction in M_s temperature as a result of refinement in austenite grain size[40–42]. One popular explanation is that in a coarse-grain austenitic structure, the strength of austenite and hence the martensite start temperature primarily depends on the chemical composition (M_s^c) because the parent austenite grains are mainly strengthened by solid solution hardening. Hence, the energy barrier to martensitic transformation is primarily compositional (E_b^c). However, in a fine-grain austenitic structure, in addition to E_b^c, there will be an extra energy barrier against deformation (E_{ext}) caused by the increase in yield stress of the

material as given by the Hall-Petch relationship[43]. The higher energy barrier requires a greater driving force ($\Delta G_{\gamma/M}$) which translates into a lower M_s temperature. In other words, the strengthening effect of the grain refinement on parent austenite will make the martensite nucleation and growth more difficult[40].

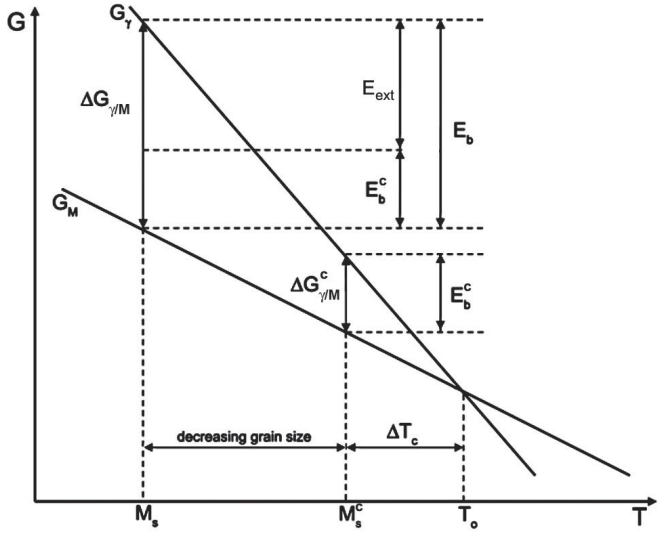

Figure 3.19. Schematic representation of the Gibbs free energy changes in martensitic transformation and the contribution of austenite grain refinement[21].

The question here is whether cell spacing can be regarded as grain size. Microstructural investigation of the studied coatings using SEM and EBSD showed that martensite lathes are stopped by cell boundaries in various locations. Figure 3.20 shows examples of this for one of the single-layer deposits. It can be seen that martensite lathes are stopped at cell boundaries which means that these boundaries acted as effective obstacles against the growth of martensite lathes. From this point of view, cell spacing can be regarded as austenite grain size because the cell and grain boundaries have the same functionality[21]. In fact, since martensite growth relies on glissile interfaces which need a certain level of coherency with the parent austenite, the misorientation across dendrite boundaries effectively hinders the growth of martensite lathes or plates[27]. In this case, the translation of slip across grain boundaries as described by Hall-Petch model is not possible and the growth of the martensite crystals will be suppressed[42].

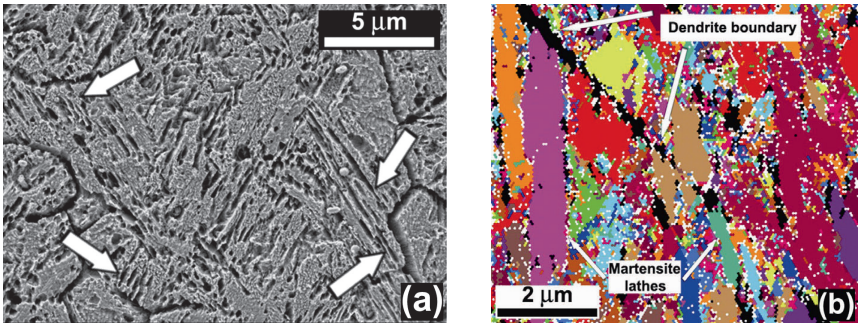

Figure 3.20. (a) SEM micrograph and (b) EBSD grain map showing how martensite lathes are stopped by dendrite boundaries.

3.5 Conclusions

Microstructure and properties of single- and multi-layer AISI 431 martensitic stainless steel coatings deposited by laser cladding at speeds up to 117 mm/s were examined. The purpose was to check if an increase in deposition rate would improve the functional properties of the coatings deposited from an alloy strengthened by martensitic transformation. The results showed that solidification structures were extremely refined at higher cladding speeds. This was accompanied by higher percentages of retained austenite, lower hardness and wear resistance. The correlation between microstructure and properties of the coatings was explained in terms of reduction in martensite start temperature as a result of microstructural refinement during solidification. It could be concluded that increasing the deposition rate does not enhance the hardness and wear resistance of laser deposited martensitic stainless steel coatings and may even deteriorate them in extreme cases. These findings show the commonly-accepted belief that microstructural refinement always improves the properties of laser deposited alloys is not necessarily true and very much depends on the strengthening mechanism of the alloy system.

References

1. Ion, J. C. *Laser Processing of Engineering Materials: Principles, Procedure and Industrial Application*; Elsevier: Boston, 2005.
2. Toyserkani, E. *Laser Cladding*; CRC Press: Boca Raton, Fl, 2005.
3. Zhong, M.; Liu, W. Laser Surface Cladding: The State of the Art and Challenges. *Proceedings of the Institution of Mechanical Engineers, Part C: Journal of Mechanical Engineering Science* **2010**, *224*, 1041–1060.
4. Kathuria, Y. P. Some Aspects of Laser Surface Cladding in the Turbine Industry. *Surface and Coatings Technology* **2000**, *132*, 262–269.
5. Frenk, A.; Kurz, W. High Speed Laser Cladding: Solidification Conditions and Microstructure of a Cobalt-based Alloy. *Materials Science and Engineering: A* **1993**, *173*, 339–342.
6. Partes, K.; Seefeld, T.; Sepold, G.; Vollertsen, F. High efficiency laser cladding at elevated processing speed. In *24th ICALEO Congress Proceedings*; LIA: Miami, FL., 2005; pp. 621–628.
7. Vollertsen, F.; Partes, K. Optimization of Laser Cladding by Using a High Speed Process. *Lasers in Engineering* **2008**, *18*, 23–33.
8. McGuire, M. F. *Stainless Steels for Design Engineers*; ASM International: Materials Park, Ohio, 2008.
9. Farias, M. C. M.; Souza, R. M.; Sinatora, A.; Tanaka, D. K. The Influence of Applied Load, Sliding Velocity and Martensitic Transformation on the Unlubricated Sliding Wear of Austenitic Stainless Steels. *Wear* **2007**, *263*, 773–781.
10. Kwok, C. .; Cheng, F. .; Man, H. . Laser Surface Modification of UNS S31603 Stainless Steel. Part II: Cavitation Erosion Characteristics. *Materials Science and Engineering: A* **2000**, *290*, 74–88.
11. Heathcock, C. J.; Protheroe, B. E.; Ball, A. Cavitation Erosion of Stainless Steels. *Wear* **1982**, *81*, 311–327.
12. Gireń, B. G.; Szkodo, M. Cavitation Erosion of Some Alloys Manufactured on Steel and Iron Surfaces by Laser Beam. *Journal of Materials Engineering and Performance* **2003**, *12*, 512–520.
13. Wang, H. .; Liu, Y. . Microstructure and Wear Resistance of Laser Clad Ti5Si3/NiTi2 Intermetallic Composite Coating on Titanium Alloy. *Materials Science and Engineering: A* **2002**, *338*, 126–132.
14. Singh, J.; Mazumder, J. Microstructure and Wear Properties of Laser Clad Fe−Cr−Mn−C Alloys. *Metallurgical Transactions A* **1987**, *18*, 313–322.
15. Preparation of Ferrous Metals for Electron Backscatter Diffraction (EBSD) Analysis http://www.struers.com/resources/elements/12/144633/Application_Note_EBSD_English.pdf (accessed Apr 19, 2013).
16. Ryde, L. Application of EBSD to Analysis of Microstructures in Commercial Steels. *Materials Science and Technology* **2006**, *22*, 1297–1306.
17. Rutherford, K. L.; Hutchings, I. M. A Micro-abrasive Wear Test, with Particular Application to Coated Systems. *Surface and Coatings Technology* **1996**, *79*, 231–239.
18. Kou, S. *Welding Metallurgy*; 2nd ed.; Wiley-Interscience: Hoboken, N.J, 2003.
19. Bontha, S.; Klingbeil, N. W.; Kobryn, P. A.; Fraser, H. L. Effects of Process Variables and Size-scale on Solidification Microstructure in Beam-based

Fabrication of Bulky 3D Structures. *Materials Science and Engineering: A* **2009**, *513-514*, 311–318.
20. Jendrzejewski, R.; Śliwiński, G.; Krawczuk, M.; Ostachowicz, W. Temperature and Stress During Laser Cladding of Double-layer Coatings. *Surface and Coatings Technology* **2006**, *201*, 3328–3334.
21. Colaço, R.; Vilar, R. Stabilisation of Retained Austenite in Laser Surface Melted Tool Steels. *Materials Science and Engineering: A* **2004**, *385*, 123–127.
22. International, ASM *ASM Handbook*; 10th ed.; ASM International: Materials Park, OH, 1990; Vol. 6.
23. David, S. A.; Vitek, J. M.; Hebble, T. L. Effect of Rapid Solidification on Stainless Steel Weld Metal Microstructures and Its Implications on the Schaeffler Diagram. *Welding Journal* **1987**, *66*, 289–300.
24. Elmer, J. W.; Allen, S. M.; Eagar, T. W. Microstructural Development During Solidification of Stainless Steel Alloys. *Metallurgical Transactions A* **1989**, *20*, 2117–2131.
25. Zambon, A.; Bonollo, F. Rapid Solidification in Laser Welding of Stainless Steels. *Materials Science and Engineering: A* **1994**, *178*, 203–207.
26. David, S. A.; Babu, S. S.; Vitek, J. M. Welding: Solidification and Microstructure. *JOM* **2003**, *55*, 14–20.
27. Porter, D. A. *Phase Transformations in Metals and Alloys*; 3rd ed.; CRC Press: Boca Raton, FL, 2009.
28. Kelly, T. F.; Cohen, M.; Sande, J. B. Rapid Solidification of a Droplet-processed Stainless Steel. *Metallurgical Transactions A* **1984**, *15*, 819–833.
29. *Heat Treater's Guide: Practices and Procedures for Irons and Steels*; 2nd ed.; ASM International: Metals Park, OH, 1995.
30. Wright, S. I.; Nowell, M. M. EBSD Image Quality Mapping. *Microscopy and Microanalysis* **2005**, *12*, 72.
31. Kurdjumow, G.; Sachs, G. Uber Den Mechanismus Der Stahlhartung. *Zeitschrift fur Physik* **1930**, *64*, 325–343.
32. Nishiyama, Z. *Sci Rep Tohoku Imp Univ Tokyo* **1934**, *26*, 637.
33. Wassermann, G. *Mitt K-Wilh-Inst Eisenforsch* **1935**, *17*, 149.
34. Greninger, A. B.; Troiano, A. R. *J Met Trans* **1949**, 185.
35. Nolze, G. Improved Determination of Fcc/bcc Orientation Relationships by Use of High-indexed Pole Figures. *Crystal Research and Technology* **2006**, *41*, 72–77.
36. Colaço, R.; Vilar, R. On the Influence of Retained Austenite in the Abrasive Wear Behaviour of a Laser Surface Melted Tool Steel. *Wear* **2005**, *258*, 225–231.
37. Koistinen, D. P.; Marburger, R. E. A General Equation Prescribing the Extent of the Austenite-martensite Transformation in Pure Iron-carbon Alloys and Plain Carbon Steels. *Acta Metallurgica* **1959**, *7*, 59–60.
38. Jiang (Jiang Bohong), B. H.; Sun, L.; Li, R.; Hsu (Xu Zuyao), T. Y. Influence of Austenite Grain Size on Γ-ε Martensitic Transformation Temperature in Fe-Mn-Si-Cr Alloys. *Scripta Metallurgica et Materialia* **1995**, *33*, 63–68.
39. Andrews, K. W. Empirical Formulae for the Calculation of Some Transformation Temperatures. *Journal of the Iron and Steel Institute* **1965**, *203*, 721–727.
40. Huang, J.; Xu, Z. Effect of Dynamically Recrystallized Austenite on the Martensite Start Temperature of Martensitic Transformation. *Materials Science and Engineering: A* **2006**, *438–440*, 254–257.

41. Brofman, P. J.; Ansell, G. S. On the Effect of Fine Grain Size on the Ms Temperature in Fe-27Ni-0.025C Alloys. *Metallurgical Transactions A* **1983**, *14*, 1929–1931.
42. Yang, H.; Bhadeshia, H. Austenite Grain Size and the Martensite-start Temperature. *Scripta Materialia* **2009**, *60*, 493–495.
43. *Physical Metallurgy*; 4th, rev. and enhanced ed.; North-Holland: Amsterdam□; New York, 1996.

Chapter 4

MICROSTRUCTURE AND PROPERTIES OF HIGH-ALLOY Ni-Cr-B-Si-C COATINGS*

In this chapter, microstructural evolutions and phase selection phenomena during laser deposition of Colmonoy 69 Ni-base hardfacing alloy are experimentally investigated over a broad range of length scales using several techniques. Possible mechanisms of microstructural formation as well as implications for functional properties of the deposits are discussed. The results show that even minor variations in the thermal conditions during solidification can modify the type and morphology of the phases. The chapter concludes with addressing the issues with laser deposition of the existing high-alloy grades of Ni-Cr-B-Si-C family such as Colmonoy 69 and lays the foundations for compositional modifications which will be presented in the next chapters.

* This chapter has been published in the following journal papers:

I. Hemmati, J.C. Rao, V. Ocelík and J.Th.M. De Hosson, Electron Microscopy Characterization of Ni-Cr-B-Si-C Laser Deposited Coatings, Microscopy and Microanalysis, 19 (2013) 1-12.

I. Hemmati, V. Ocelík, and J.Th.M. De Hosson, Dilution effects in laser cladding of Ni–Cr–B–Si–C hardfacing alloys, Materials Letters, 84 (2012) 69–72.

I. Hemmati, V. Ocelík, K. Csach, and J.Th.M. De Hosson, Microstructure and phase formation in a rapidly solidified laser deposited Ni-Cr-B-Si-C hardfacing alloy, Metallurgical and Materials Transactions A, in print.

4.1 Introduction

THE focus of this chapter will be on microstructure and properties of laser-deposited Ni-base hardfacing coatings for hydraulic piston rods. In CHAPETR 1, the approach to select coating materials and required properties of the coatings were briefly addressed. In this chapter, microstructure and properties of Colmonoy 69 coatings deposited at different cladding speeds will be discussed. According to manufacturer's datasheet, Colmonoy 69 (nominal composition: Ni-13.5Cr-3B-4Si-0.7C-2.1Mo-1.7Cu-4Fe (wt.%)) produces thermal sprayed and fused coatings with hardness values of 58-63 HRC (650-775 HV). The laser deposited Colmonoy 69 coatings could be harder (up to 900 HV) as will be presented later. High Cr content along with Mo and Cu enhance the pitting corrosion resistance of this alloy. The combination of high hardness and good corrosion resistance suggests that Colmonoy 69 would be a suitable candidate coating material for hydraulic piston rods of dredging applications.

Colmonoy 69 is a member of Ni-Cr-B-Si-C family of corrosion resistant hardfacing alloys. This family was originally developed for deposition by spray and fuse techniques[1]. The phase constitution of Ni-Cr-B-Si-C alloys is based on four binary diagrams shown in Figure 4.1, namely Ni-Si, Ni-B, Cr-B and Cr-C. Additions of Si and B are made to produce low-temperature (around 1000 ^{o}C) Ni-Si and Ni-B eutectics which facilitate the fusing step and also give a self-fluxing character to the deposits by protecting them against oxidation[1]. Both of these attribute are essential during thermal spray and fuse deposition while none are needed for laser deposition. The Cr-B and Cr-C pairs generate several types of boride and carbide precipitates which increase the hardness and wear resistance of the deposits. These precipitates are the first phases to solidify. Ni dendrites containing Fe, Cu and parts of Cr, Mo and Si solidify at intermediate temperatures between the precipitation and eutectic reactions.

Depending on the content of alloying elements, Ni-Cr-B-Si-C alloys can be roughly divided to high-alloy and low-alloy grades. Colmonoy 69 is one of the high-alloy grades in which high content of B and Cr and low ratio of Si/B generate a microstructure with numerous boride precipitates and a considerable amount of interdendrtitic eutectics. The low-alloy grades contain less B and Cr and high Si/B ratios. These categories will be further discussed in CHAPTER 6.

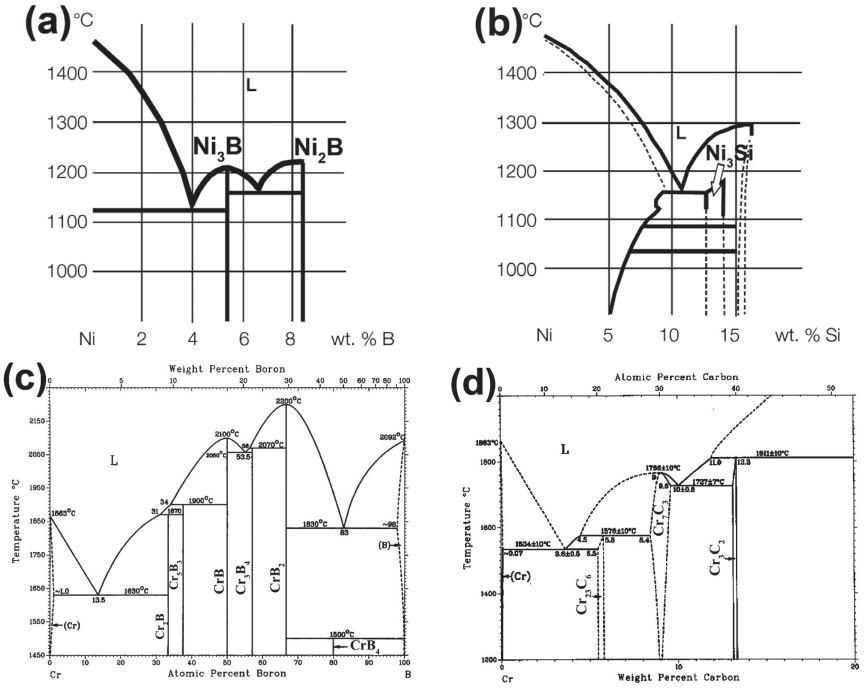

Figure 4.1. Ni-rich sides of (a) Ni-B and (b) Ni-Si binary phase diagrams, (c) and (d) binary phase diagrams of Cr-B and Cr-C, respectively[2].

In order to evaluate the effects of deposition rate on microstructure and properties of Colmonoy 69 coatings, samples studied in this chapter were deposited at 5, 10 and 20 mm/s on cold and preheated substrates. The idea was similar to what was already explained in CHAPTER 3, i.e. whether increasing the cooling rate at higher deposition speeds[3] or by deposition on cold substrate[3] will produce coatings with enhanced properties. The outcome was even more unexpected than that for martensitic stainless steel coatings.

The multitude of microstructural variations in Colmonoy 69 coatings necessitated careful and detailed phase identification and microstructural observation. Such analyses had to cover a broad length scale ranging from microstructural heterogeneities in millimeter-sized coatings studied by Optical Microscopy (OM), low magnification Scanning Electron Microscopy (SEM) and X-ray Diffraction (XRD) to characterization of micrometer and sub-micrometer precipitates by a combination of Energy Dispersive Spectroscopy (EDS) and Electron Backscatter Diffraction (EBSD) and finally observation and characterization of nanometer-sized eutectic structures by Transmission Electron Microscopy (TEM). Among these techniques, the EDS/EBSD combination for characterization of boride and carbide precipitates was more

novel, less straightforward and more versatile in comparison to the other ones. Hence, the EDS/EBSD combination and its significance in the context of the current research have to be further explained.

The use of EBSD for identification of unknown phases has increased in recent years because of its capability of conclusive phase identification in selected areas with a submicron spatial resolution[4–7]. Furthermore, the possibility of combining EBSD crystallographic information with EDS compositional data, the imaging capabilities of SEM (using Secondary Electron (SE) or Backscatter Electron (BSE) detectors) and the relatively easy sample preparation have made EBSD a powerful tool for phase identification in many metallic and nonmetallic systems[5,8–11].

The spatial resolution of EBSD is two orders of magnitude higher than conventional XRD and two orders of magnitude lower than TEM, filling the gap between them and perfectly suitable for characterization of microstructural features in numerous selected areas[4]. As EDS and EBSD detectors are both installed on SEM, it is possible to explore and observe relatively large areas of the samples under SEM and perform EDS or EBSD characterization and their combinations on areas or phases of interest. Such a unique capability was crucial for characterization of microstructural heterogeneities in Colmonoy 69 coatings. The procedure to perform EDS/EBSD phase identification will be explained in section 4.4.2 .

The results discussed in this chapter will show the issues with laser deposition of the existing high-alloy grades of Ni-Cr-B-Si-C family such as Colmonoy 69 and lay the foundations for compositional modification of these alloys as will be presented in CHAPTERS 5 & 6.

4.2 Experimental procedure

Deposition experiments and characterizations of this chapter were done in three stages. In the first stage, Colmonoy 69 gas-atomized powder from Wall Colmonoy Ltd. was deposited on S355 plain low-carbon steel rods using a fiber laser and side-cladding set-up. Single tracks and single-layer coatings (five tracks, 33% overlapping) with a thickness of 0.9-1.1 mm were deposited at scanning speeds of 5, 10 and 20 mm/s using laser powers of 800-1600 W. For each condition, one single-track and one multi-track coatings were deposited and three sample were prepared for subsequent characterizations. Dilution from the substrate (calculated as explained in CHAPTER 1) was kept in the range of 5-15 percent by adjusting the laser power. If needed,

depositions were repeated to obtain samples with the required level of dilution. To avoid cracking of the coatings, substrate was preheated to 500 ^{o}C using the tube furnace immediately before cladding. The coated bars were left in the furnace to cool slowly down to the room temperature.

Samples for OM/SEM analyses and hardness measurements were cut from transversal and longitudinal cross sections and prepared by mechanical grinding with suspensions containing 9 and 3 μm diamond particles and polishing with colloidal Al_2O_3. One of the samples was etched with a solution consisting of 7 ml HF, 3 ml HNO_3 and 5 ml H_2O to reveal the eutectic structures in SEM analyses. The eutectic structures were also visible in as-polished samples under OM.

Characterization of samples revealed several microstructures with gradual or abrupt changes. Phase identifications using EDS/EBSD and TEM proved that the microstructural variations were not just morphological changes, but changes in type of the constituent phases. Furthermore, hardness measurements confirmed that functional properties of various microstructures could be significantly different. Hence, it was important to explain the mechanisms of the observed microstructural evolutions in the deposits.

The multitude of microstructural variations and phase changes in multi-track deposits proved that an experimental analysis of microstructural evolutions directly on the multi-track samples was not easy. Variations in type and morphology of the constituent phases can be attributed to either changes in chemistry of the alloy or the thermal conditions during solidification. Hence, new experiments were done to assess the role of these two factors in phase formation reactions.

The second stage of the experiments was done to evaluate the effects of chemistry, i.e. percentage of dilution. Single-track samples were deposited at a speed of 5 mm/s with 5-45 percent dilution. Microstructure, phase constitution and hardness were evaluated and the dilution-microstructure-properties correlations were established.

Complexity of the thermal conditions in multi-track samples made it necessary to start with either simpler cases or cases in which the thermal conditions were better known. In order to establish the relationship between thermal conditions and microstructural evolutions, a third stage including the following experiments was performed:

(i) The DTA samples cooled at 10 and 100 K/min: The cooling rate of DTA samples is orders of magnitude lower than the cooling rates experienced during laser cladding process (higher than 10^3 K/s^3). However, the DTA

samples are cooled with precisely controlled rates without any dilution effects and can be used to observe the trends in microstructural changes with increasing cooling rate.

(ii) The single-track samples deposited on preheated substrates: In practice, most Ni-Cr-B-Si-C alloys are deposited on preheated substrates to prevent cracking[12]. The single-track samples deposited on a preheated substrate at the same laser cladding speeds are good representatives for the real coatings. Moreover, absence of overlapping and shorter deposition times, make these samples easier to analyze.

(iii) The single-track samples deposited on cold substrates: These samples were meant to simulate the effect of higher cooling rates as the cooling rate for deposition on the cold substrate is higher than the same value for deposition on preheated substrates[3].

(iv) Starting powder particles rapidly solidified during the gas atomization process: The gas-atomized powder particles with a size of 50-150 μm can be considered as small droplets of melt rapidly solidified with a cooling rate (10^3-10^5 K/s for inert gas atomization[3,13]) comparable to the cooling rate during laser cladding. Powder particles also contain no dilution effects. However, they may have variable amounts of impurities and heterogeneous nucleation sites and can solidify at different levels of undercooling.

4.3 Microstructural variations in multi-track deposits

Preliminary SEM observations of the samples showed that their microstructure was not uniform across the depth and length of the clad layers. So, it was decided to perform a detailed track by track characterization. Figure 4.1(a) shows the transversal cross-section of a five-track coating (first track on the left side) deposited at a speed of 5 mm/s. The labels in Figure 4.2(a) denote locations in different tracks from which the dominant microstructures are presented by the SEM images of Figure 4.2(b) to (g). Most of the SEM observations were done using BSE imaging mode on as-polished samples. In this way, the boride and carbide precipitates could be observed in detail.

Substantial differences in size, shape and composition (based on BSE image contrast) of the precipitates could be observed from the first to the last track as shown in Figure 4.2(b) to (e). In tracks 1 and 2, the precipitates were mostly blocky (Figure 4.2(b) and (c)). The main difference between these two tracks was the bigger size of precipitates in track 2 because of the lower dilution. The effects of dilution on boride precipitates will be discussed in

more detail in section 4.5.1 . In track 3, butterfly-shape precipitates were dominant but there were some blocky precipitates as well (Figure 4.2(d)). In tracks 4 and 5, the microstructure was entirely different and consisted of a mixture of floret-shape structures and dendritic phases (Figure 4.2(e)). The insert in Figure 4.2(e) shows a close-up view of what is called the "floret-shape structure" throughout this text. In some cases, abrupt microstructural changes were found inside one track or from one track to the subsequent one as shown in Figure 4.2(f). The abrupt changes indicate sharp thresholds at which variations in phase formation could occur. These microstructural variations could sometimes happen from bottom to top of one track. Figure 4.2(g) shows the cross section of track 5 (position g) in which after a thin layer of columnar dendrites adjacent to the substrate-clad interface, first blocky and then butterfly-shape precipitates formed and finally a mixture of floret-shape structures and dendritic phases became dominant. The precipitate-free layer of columnar dendrites was present in all of the samples. Thickness of this layer depended on the level of dilution. At higher cladding speeds, the microstructure consisting of floret-shape structures and dendritic phases was formed in earlier tracks although the changes were not always consistent. The hardness of microstructures shown in Figure 4.2(b) to (e) had significant differences as will also be discussed later.

4.4 Phase identification

4.4.1 XRD

In many previously published studies on Ni-Cr-B-Si-C coatings, conventional XRD was the only phase identification tool[14–20] and in some other works, EDS results were used to help interpret the XRD data[11,21–23]. The problem with the latter case is that the structural information provided by XRD represents microscopically large regions and correlation between compositional information obtained by EDS in the micron scale (e.g. by elemental mapping of a few borides or carbides) with crystallographic information obtained by XRD is difficult, especially in multiphase and heterogeneous systems[24].

But even more importantly, the identification of unknown phases only based on conventional XRD will produce tentative results[25,26]. A complication in conventional XRD phase identification is that diffraction patterns of different phases may superimpose and consequently cause uncertainties as to which diffraction peak belongs to which phase (or phases). Although, in

principle, a diffraction pattern is ‘‘unique’’, in practice there may be considerable similarities between patterns. This can obscure the identification process particularly in the case of multiphase specimens. Mixtures of phases with low symmetry, as in the case of Ni-Cr-B-Si-C coatings, are usually more difficult to differentiate due to the larger number of diffraction peaks[26].

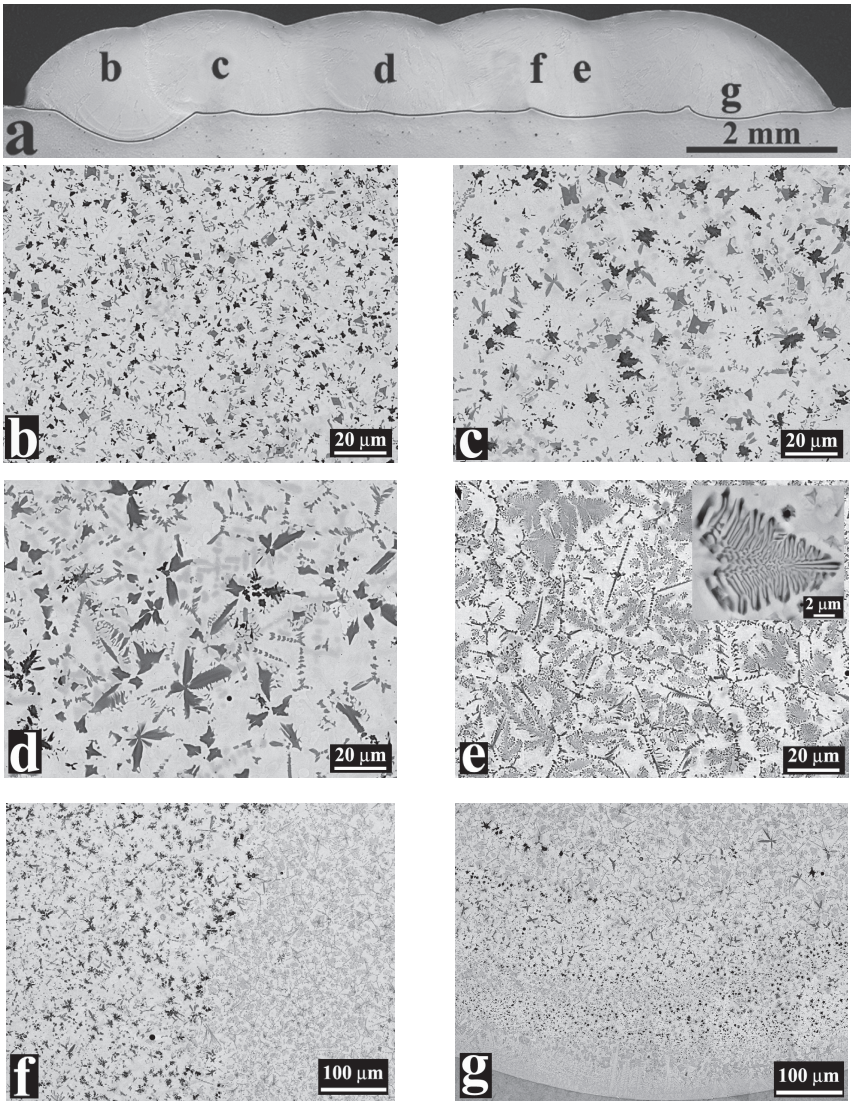

Figure 4.2. (a) OM image showing the transversal cross-section of a five-track deposit.(b) to (e) SEM-BSE images showing the microstructure of different tracks as labeled in (a). (f) and (g) SEM-BSE images showing the abrupt or gradual microstructural changes in the locations labeled f and g in (a).

For laser deposited coatings, extended solubility, strong texture and internal stresses in the clad layer can make the conventional XRD phase identification even less reliable[25]. Using the high brilliance and resolution of synchrotron X-ray or refinement and optimization tools such as the Rietveld technique, many of the above-mentioned issues may be solved[27]. In the current research, conventional XRD analysis was done to check its capabilities and limitations for phase identification of the intended coatings first-hand.

Figure 4.3 shows the XRD patterns obtained from Colmonoy 69 powder and one of the deposits. Although the diffraction patterns are generally similar, there are some differences. The peaks of Ni for the clad layer are slightly shifted to the left which indicates an increase in the lattice parameter of Ni solid solution in the clad layer. The lattice parameters of Ni solid solution in clad layer and Colmonoy 69 powder were calculated to be 0.357 and 0.355 nm respectively. This increase can be attributed to dissolution of Fe in Ni as a result of dilution. Except for the peaks of Ni, most of the other peaks are small in intensity and close to each other. In the case of the clad layer, the peaks are broadened which resulted in several peaks overlaps. This broadening can be related to the distortions of the crystal structures caused by the rapid cooling during laser processing[25].

The peak overlaps and the fact that in many cases agreement was obtained only for some of the peaks (except for the peaks of Ni), made it difficult and inconclusive to identify the phases based on the XRD spectra. This is not unexpected as the microstructure of these deposits consisted of several phases with low symmetry crystal structures (e.g. orthorhombic CrB and Ni_3B) each in relatively small quantities. Without complementary techniques, conventional XRD phase identification of Ni-Cr-B-Si-C coatings will not be conclusive. However, by considering the results obtained from EDS/EBSD and TEM given in detail later on, it was possible to identify the peaks in XRD spectra as shown in Figure 4.3.

4.4.2 EDS/EBSD

The first step was compositional analysis of the intended phases by EDS to get qualitative compositional information. This information was later used as a filter to select the candidate phases. In this work, EDS line scanning was used to identify the elements in particular phases.

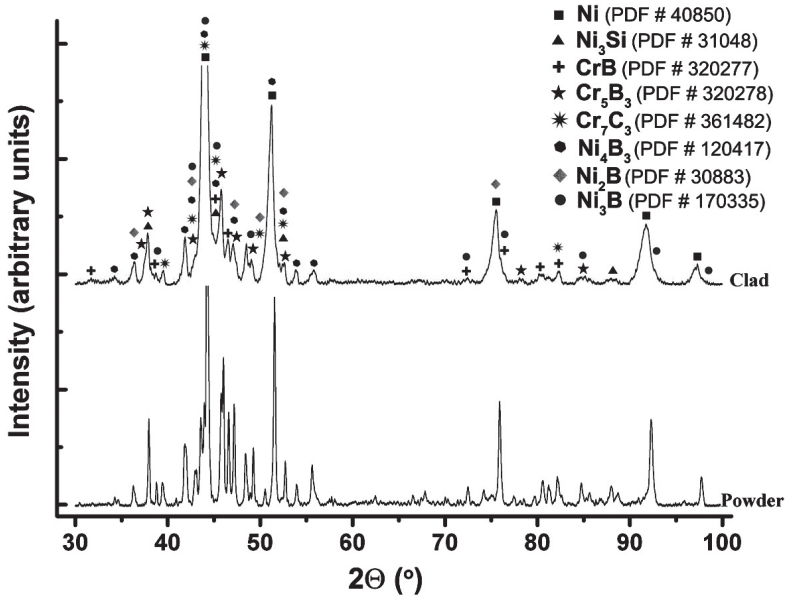

Figure 4.3. XRD spectra of Colmonoy 69 powder and clad layer (The main peak of Ni is cut out to make the weaker peaks more visible).

Figure 4.4 shows an example line scan where Cr carbide and two Cr borides could be distinguished during scanning from left to right. In some previous researches, the two steps of EDS and EBSD were done simultaneously[4,7]. But for identification of borides and carbides, simultaneous EDS and EBSD may not produce the best possible results because of various reasons. Apart from the different optimum working distances for EDS and EBSD, the low acceleration voltages necessary for optimum EDS analysis of light elements such as B and C will generate a very weak EBSD pattern, especially from low symmetry compounds with complicated crystal structures (e.g. orthorhombic CrB). In addition, the spatial resolution of EDS and EBSD are very different with the former in the range of micrometer and the latter in the submicron range[4]. As a result, to avoid the mismatch between spatial resolutions and to obtain the optimum data with the highest accuracy, the EDS and EBSD analyses were done separately at two different acceleration voltages and working distances, i.e. 5 kV and 10 mm for EDS and 30 kV and 15 mm for EBSD. By knowing the composition of different precipitates, a list of possible candidates can be gathered. If the structure file for any of the candidate phases does not exist in the *TSL database* (the standard database of the EBSD system), the structure file should be created and optimized.

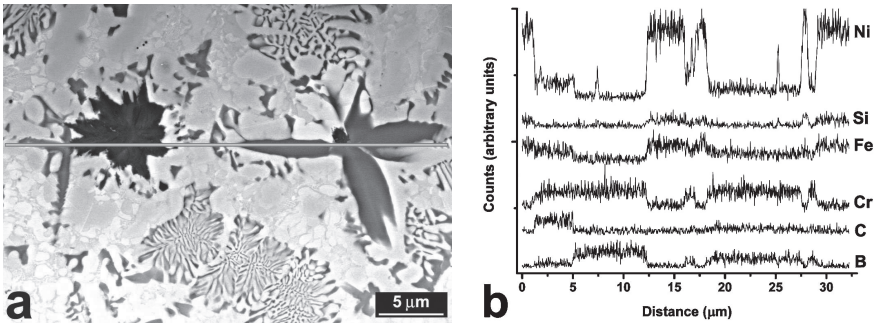

Figure 4.4. (a) EDS scanning along the line over precipitates, (b) variations of different elements which allow distinguishing the carbide and borides.

For Cr borides, the link to *International Center for Diffraction Data (ICDD)* was used to generate the structure files. Then, these structure files were optimized by collecting and indexing several high resolution patterns from each precipitate. Reflectors were optimized by visual scrutiny and manual adjustments to obtain fit values (the angular error between collected and predicted patterns) of less than 1°. The optimization step is important to account for the differences between X-ray and electron diffraction patterns[4]. Before optimization of the structure files, the EBSD system was carefully calibrated by fine tuning of the indexed patterns obtained from Ni. Figure 4.5 shows the EBSD patterns obtained from boride and carbide precipitates and their indexing by generated and optimized structure files. In Figure 4.5(b), (d) and (f), the solution errors are 0.85, 0.5 and 0.3 degree respectively. Phase parameters for Cr boride precipitates are presented in Table 4.1.

An important issue in the phase identification by EBSD is consistency or reproducibility of the indexing process for different crystal orientations of a particular phase. If an entry indexes a phase correctly for some crystal orientations but not for all of them, i.e. if it does not index the phase consistently, the reflectors are not optimal and hence, the indexing and identification procedures will not be reliable. After optimization of the structure files and checking the consistency of the indexing process, it was possible to perform scans on precipitates or areas of interest. For an accurate pattern indexing, the criteria for a minimum number of bands of more than 9 and maximum solution error of less than 1.5 ° were applied in all EBSD scans[28]. Figure 4.6 presents SEM images along with Inverse Pole Figure (IPF) maps of selected precipitates identified as polycrystalline orthorhombic CrB, single crystal tetragonal Cr_5B_3 and single crystal hexagonal Cr_7C_3.

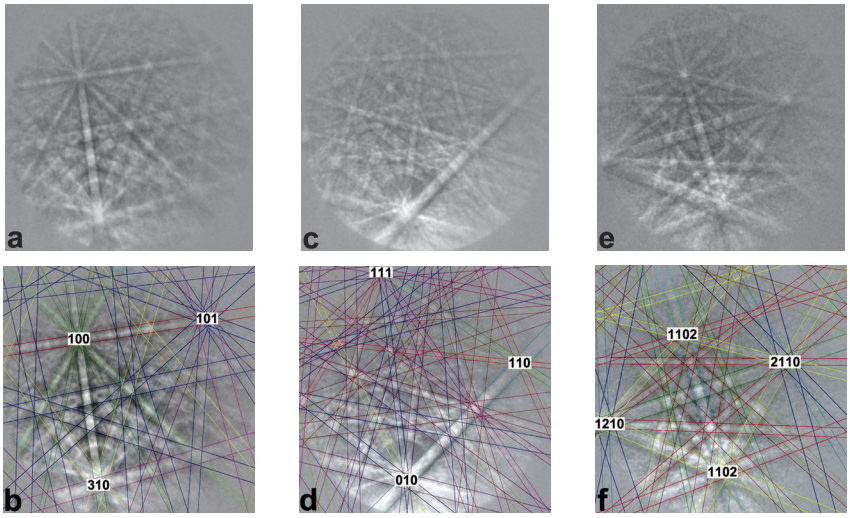

Figure 4.5. Experimental EBSD patterns and their indexing by the optimized structure files, (a) and (b): CrB, (c) and (d): Cr_5B_3, (e) and (f): Cr_7C_3.

Table 4.1. Crystallographic features of Cr boride precipitates.

Phase	Symmetry point group	Lattice parameters (nm)			Reflector planes
		a	b	c	
Cr_5B_3	Tetragonal (D4h)[4/mmm]	0.537	-	1.018	(112),(200),(202) (211),(114),(213) (220),(204),(310) (006),(413),(334)
CrB	Orthorhombic (D2h)[mmm]	0.296	0.786	0.293	(110),(021),(111) (130),(131),(200) (002),(060),(151) (221),(132),(170)

The following steps were taken to clean-up the EBSD scan data:
(i) Grain Confidence Index (CI) Standardization,
(ii) Removal of data points with CI less than 0.05,
(iii) Neighbor CI Correlation with minimum Confidence Index of 0.05. (CI shows the degree of confidence in correct indexing.)

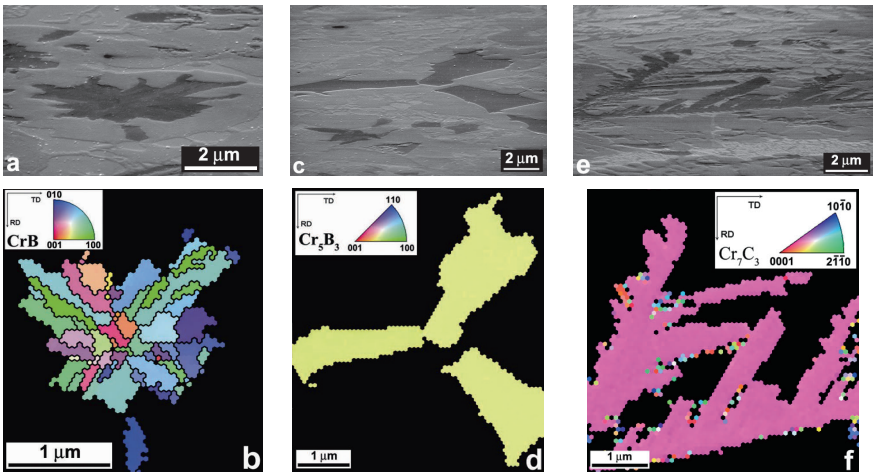

Figure 4.6. SEM images (70 ^{o} tilted) and the IPF maps of the main types of precipitates in Colmonoy 69 coatings: (a) & (b): polycrystalline CrB, (c) & (d): single crystal Cr_5B_3,, e & f: single crystal Cr_7C_3 (minimum boundary misorientation: 5 ^{o}).

According to a previous research[21], the floret-shape structures contain layers of Ni and Cr boride. The EBSD results corroborated that the floret-shape structures consisted of Ni and Cr_5B_3 as shown in Figure 4.7. As the layers of Cr_5B_3 in the floret-shape structures are around 100 nm, it was necessary to reduce the step size during the EBSD scans to 50 nm or less. The black areas in Figure 4.7(b) and (c) are filtered because of poor indexing.

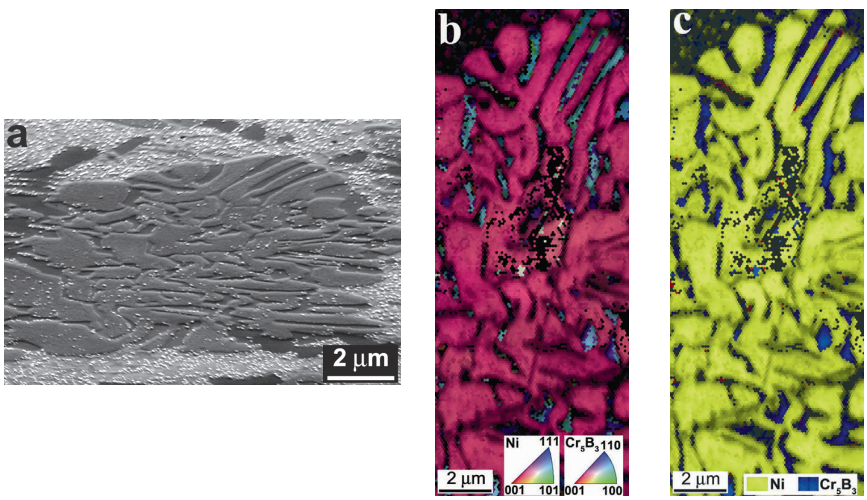

Figure 4.7. (a) SEM image of a floret shape structure (70 ^{o} tilted), (b) IPF and (c) phase map, both superimposed on the image quality map.

4.4.3 Transmission Electron Microscopy

The Ni-Cr-B-Si-C alloys are designed to contain large amounts of Ni-B and Ni-Si eutectics to lower their melting point and facilitate the fusing step during the thermal spray and fuse deposition[25]. Depending on B and Si content, different quantities of fine eutectic structures will form[1]. Resolution of EDS/EBSD combination is not high enough to conclusively identify the eutectic phases. Hence, TEM was used for characterization of the fine eutectics. A combination of TEM-EDS data and the Selected Area Diffraction (SAD) patterns were used for all TEM phase identifications.

Eutectic structures could be observed by SEM (after etching the sample) as shown in Figure 4.8(a) with the same appearance as in TEM bright-field images (Figure 4.8(b)). The features in Figure 4.8(b) have two different length scales: the submicron layered structure and the micron-size dendrites. The submicron layered structure consisted of Ni_3B (dark) and Ni_3Si_2 (bright) as shown in Figure 4.9. Ni_3Si_2 is not a eutectic phase itself. But may form in the solid state[29] from eutectic products such as NiSi or $NiSi_2$. In Figure 4.10, the diffraction pattern obtained from the submicron layers observed between islands of Ni_3Si could be indexed as Ni_3B.

Figure 4.11 shows the coexistence of Ni_3B and Ni_2B, the latter containing many stacking faults. The presence of Ni_3B in almost all of the TEM analyses shows that the Ni-Ni_3B was the main Ni-B eutectic reaction in Colmonoy 69 coatings. Formation of Ni-Ni_2B can be attributed to the non-equilibrium solidification caused by the rapid cooling during laser cladding[25]. Simultaneous existence of Ni_3B and Ni_2B suggests that both Ni-Ni_3B stable reaction and Ni-Ni_2B metastable reaction could occur during the laser deposition.

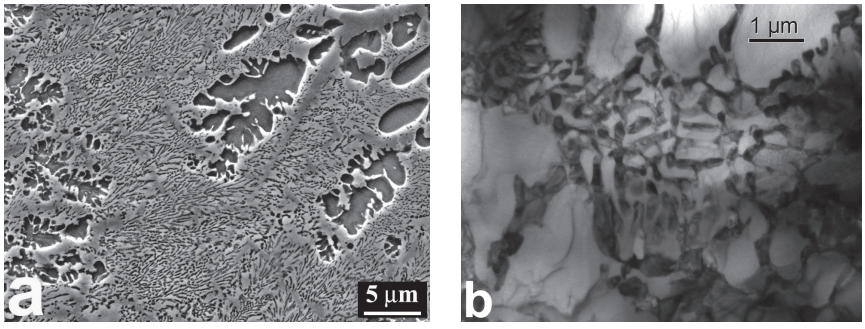

Figure 4.8. The eutectic structures observed by (a) SEM and (b) TEM.

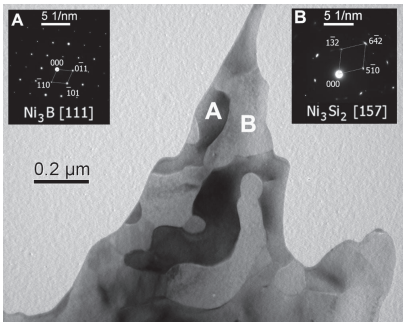

Figure 4.9. TEM image of the submicron eutectic structure with A and B layers identified by SAD as Ni_3B and Ni_3Si_2, respectively.

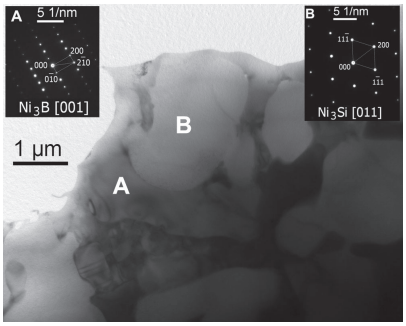

Figure 4.10. Islands of Ni_3Si separated by layers of Ni_3B as identified by SAD.

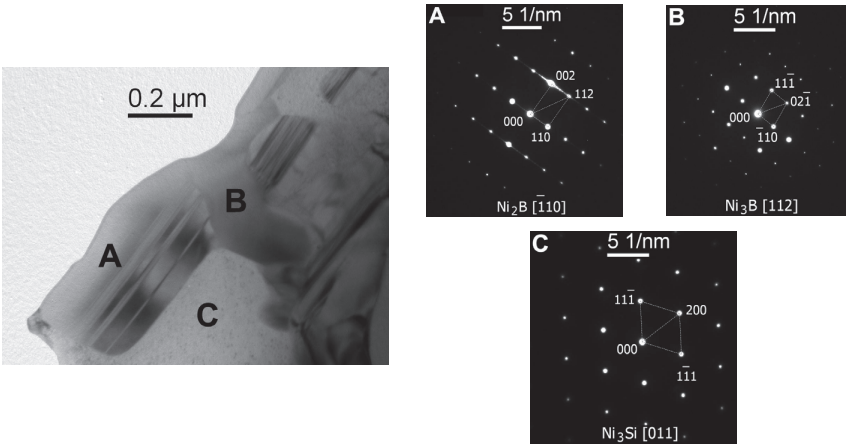

Figure 4.11. TEM image and SAD patterns of Ni_2B, Ni_3B and Ni_3Si.

The results up to now prove that Ni-Cr-B-Si-C alloys have the potential to form various types of strengthening phases. This not only includes Cr boride precipitates, but also Ni-B and Ni-Si eutectic phases. In fact, depending on the ratio between free Si and B, different eutectic reactions may happen[30]. Free Si and B are fractions of the original Si and B contents which were not depleted out of the melt through precipitation of borides or solidification of Ni solid solution dendrites. It seems that possibility of different precipitation reactions, rapid cooling during laser deposition and the inherent complexity of eutectic reactions are the reasons for observing multiple microstructures in the studied coatings. These can also explain different reports in literature on microstructure and phases of coatings deposited by laser cladding from similar Ni-Cr-B-Si-C alloys[23,25,31–33].

TEM analyses confirmed and extended the findings of EBSD on identification of floret-shape structures and Cr_7C_3. Figure 4.12(a) shows the TEM bright-field image of a floret-shape structure. Figure 4.12(b) is a close-up of (a) for identification of the constituent phases by SAD. The SAD confirmed the findings of EBSD that in floret-shape structures, layers of Ni were separated by bands of Cr_5B_3. In addition to Cr_5B_3 layers, CrB (area C in Figure 4.12(c)) and Ni_3B could also be found at the edges of the floret-shape structures. Formation of floret-shape structures can be explained by the following ternary eutectic reactions in the Ni-Cr-B system[34]: $L \rightarrow Cr_5B_3 + Ni_3B + Ni$ which is the stable reaction at 1100 ^oC and $L \rightarrow CrB + Ni_3B + Ni$, a metastable reaction at 1080 ^oC. It seems that the high cooling rates during laser deposition allowed the metastable reaction to happen shortly after the stable reaction. Consequently, product of the metastable reaction formed at the edges of the stable products.

Based on the EDS/EBSD results, carbide phases were mainly of Cr_7C_3 type. Carbides were easy to distinguish because of their dendritic morphology and good contrast in BSE images (Figure 4.13(a)). Figure 4.13(b) shows the TEM bright-field image of a dendritic structure identified as Cr_7C_3 according to SAD pattern (in line with the results of EBSD).

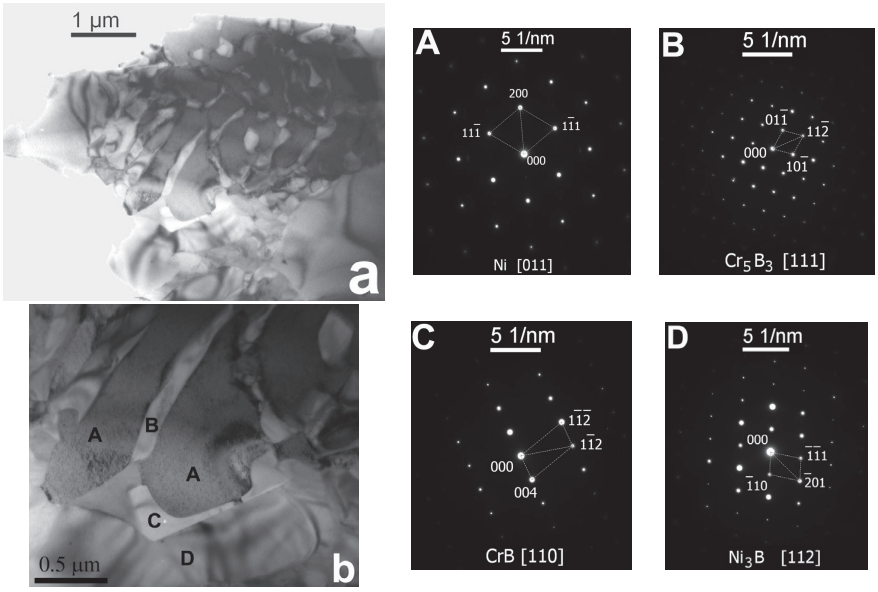

Figure 4.12. (a) Floret-shape structure observed by TEM bright field, (b) close-up view of (a) with A, B, C and D identified as Ni, Cr_5B_3, CrB and Ni_3B, respectively.

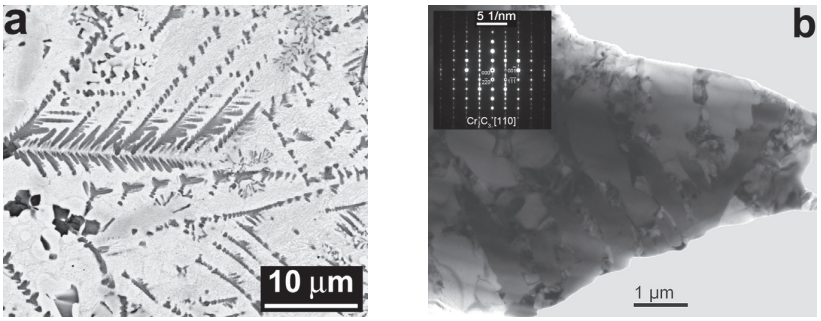

Figure 4.13. (a) Dendritic morphology of Cr_7C_3 (BSE image), (b) TEM image of the dendritic phase identified as Cr_7C_3 according to SAD.

4.5 Processing-microstructure relationships

In this section, the results of the second and the third stages of experiments which were done to assess the effects of changes in chemistry (i.e. dilution) and cooling rate during solidification of the laser deposited Colmonoy 69 coatings will be presented.

4.5.1 Effects of dilution

The main contribution of dilution from the carbon steel substrate (with minor amounts of Mn, Si, Ni and Cr) was increase of iron (Fe) content in the clad layer. The Fe content was measured by EDS over an area of 1 by 1 mm in the single tracks with different amounts of dilution. It was found that single tracks with 5, 10, 15, 25, 30 and 35 percent of dilution contained around 8, 14, 18, 25, 32 and 39 wt.% of Fe, respectively. Higher dilution reduced the amount of Ni-B-Si eutectics as shown in Figure 4.14. In addition, as Fe content increased, boride precipitates started to change in morphology and gradually diminished (Figure 4.15). In other words, high Fe content modified and suppressed the precipitation of Cr borides at the beginning and formation of Ni-Si-B eutectics at the end of the solidification. The influence of Fe content on microstructure and phase formation of Colmonoy 69 coatings could also be observed near coating-substrate interfaces as shown in Figure 4.16. In all coatings, a precipitate-free layer of columnar dendrites existed adjacent to the interface. This precipitate-free band progressed with increasing dilution and ultimately expanded to the whole coating for Fe contents of more than 40 wt.%. EDS mapping confirmed that the interfacial layer was enriched with Fe without precipitation of primary Cr borides as represented in Figure 4.16(b) and (c).

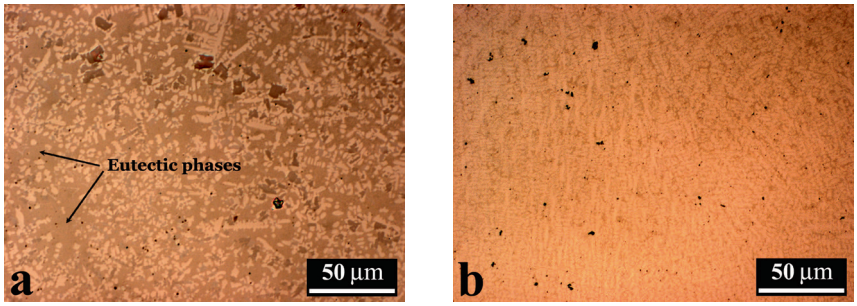

Figure 4.14. OM images of the deposits with (a) 5% and (b) 35% dilution showing reduction in the amount of eutectic structures at higher dilutions.

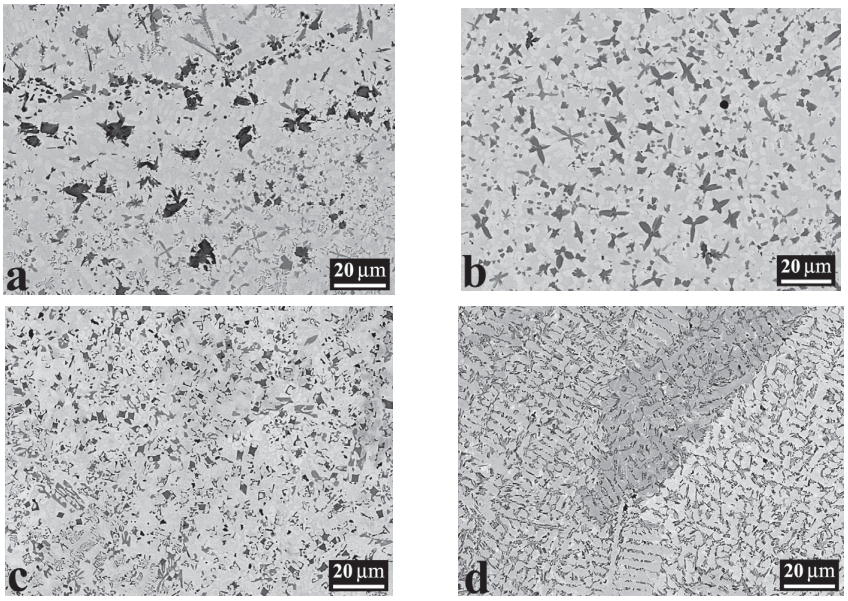

Figure 4.15. SEM images showing the microstructure of deposits with different dilutions: (a) 5%, (b) 10%, (c) 25%, (d) 35% and higher.

The fact that convection in the melt pool could homogenize the composition in areas above the interface layer was because of the Columnar to Equiaxed Transition (CET) in the Ni dendrites. In all of the samples, the columnar dendritic structure close to the interface (Figure 4.17(a)) was replaced by equiaxed dendrites (Figure 4.17(b)). EBSD scans were performed on the longitudinal cuts at the middle of the track to study the morphological changes of the Ni grains from bottom to top of the deposits. Figure 4.17(d) shows the IPF map of the interface region shown in Figure 4.17(c) in which the CET in Ni dendrites around 100 µm from the clad-substrate interface is

clearly visible. The columnar structure close to the interface hinders the flow in the melt pool and prevents the compositional homogenization. Based on Figure 4.16 and Figure 4.17, it is possible to establish a direct relationship between extent of the columnar structure adjacent to the interface and thickness of the iron-rich interfacial layer.

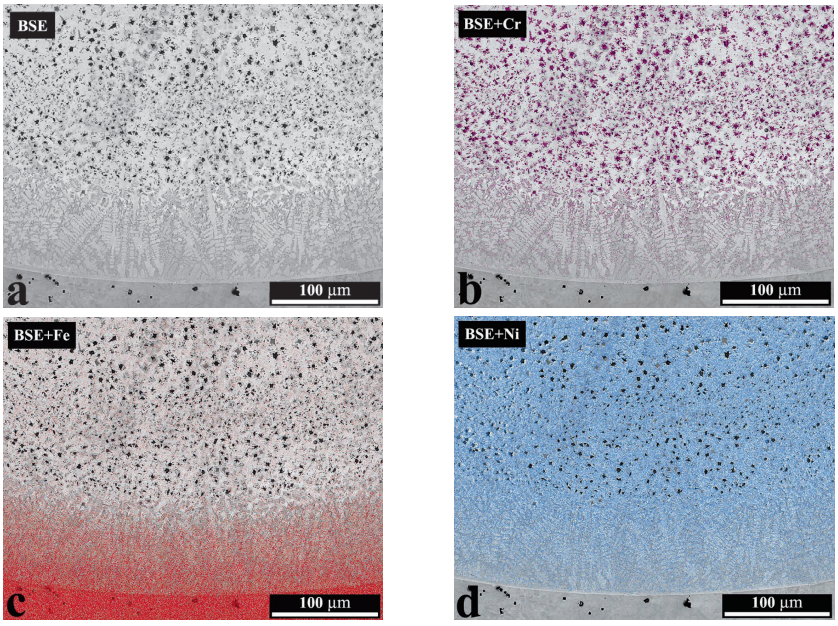

Figure 4.16. (a) SEM-BSE image of the precipitate-free interface layer, (b) to (d) EDS map for Cr, Fe and Ni superimposed on the SEM image.

In five-track samples, the effect of dilution demonstrated itself as the change of microstructure from the first to the second track (Figure 4.18(a)). EDS quantitative analysis showed that tracks 1 and 2 contained around 26 and 15 wt.% Fe. To confirm the role of Fe in the transition shown in Figure 4.18, the dominant Cr borides in the two microstructures were quantitatively characterized by EDS at a voltage of 5 kV. To compensate for limited detector accuracy for X-ray lines below 1 keV (e.g. B), a Standardless Element Coefficient (SEC) of 4 was applied in the *EDAX Genesis* software. The appropriate value of SEC was obtained based on previously identified CrB with around 50 atomic % of B. Higher Fe content of the first track favored Cr borides with a higher Fe fraction. This means that Fe content could influence the amount, size and type of borides. The observed changes in Cr borides and Ni-B-Si eutectics with Fe content can be attributed to different compositions of the initial melt which can modify the solidification path of the alloy.

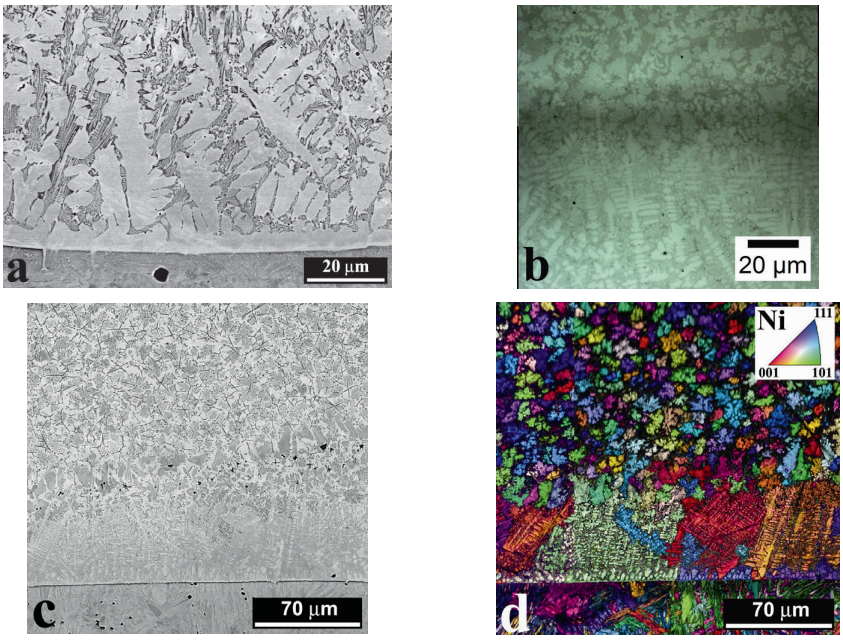

Figure 4.17. (a) SEM-BSE image showing the planar layer at the interface and the change to columnar structure, (b) OM image of the CET region, (c) SEM-BSE image of the interface region and (d) IPF+IQ map (boundary misorientation: 5 °) showing the CET from bottom to the top of the track shown in (c)

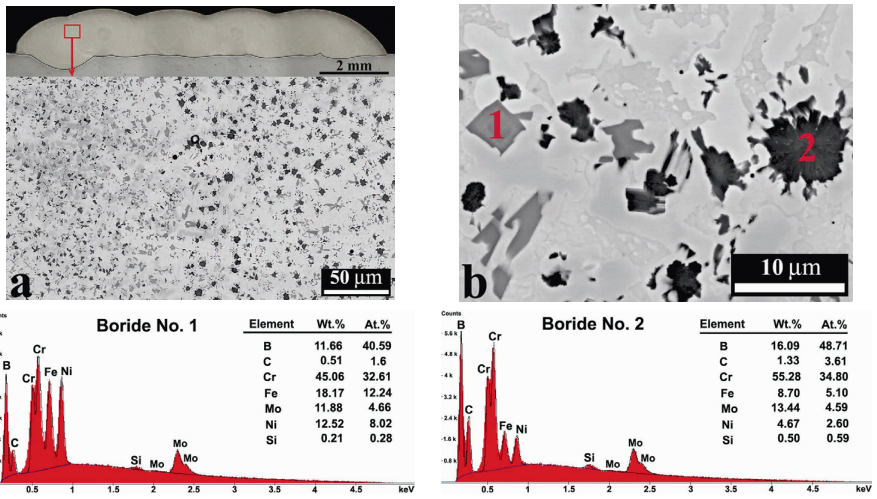

Figure 4.18. (a) Change of the microstructure across the interface between tracks 1 and 2, (b) close-up of the interface in (a) showing the main borides of each side and their chemical compositions.

4.5.2 Effects of cooling rate

4.5.2.1 DTA samples

The DTA thermograms were analyzed for their thermal events. Also, microstructure of the relevant DTA samples were observed by SEM. Figure 4.19 shows the DTA graphs along with the microstructure of the samples solidified at 10 and 100 K/min. Contrary to graph (b) which contains only three thermal events below 1200 ^{o}C, the graph in (a) has several peaks in the temperature range of 1500-1200 ^{o}C as well as the same peaks in (b). The diversity of the phases in the microstructure of Figure 4.19(c) confirms that solidification of Colmonoy 69 at a slower rate generated multiple borides with different morphologies. On the other hand, increasing the cooling rate suppressed the blocky borides and most of the microstructure consisted of floret-shape structures in a matrix of Ni along with eutectics. An interesting feature of Colmonoy 69 is its very wide solidification range (more than 500 degrees).

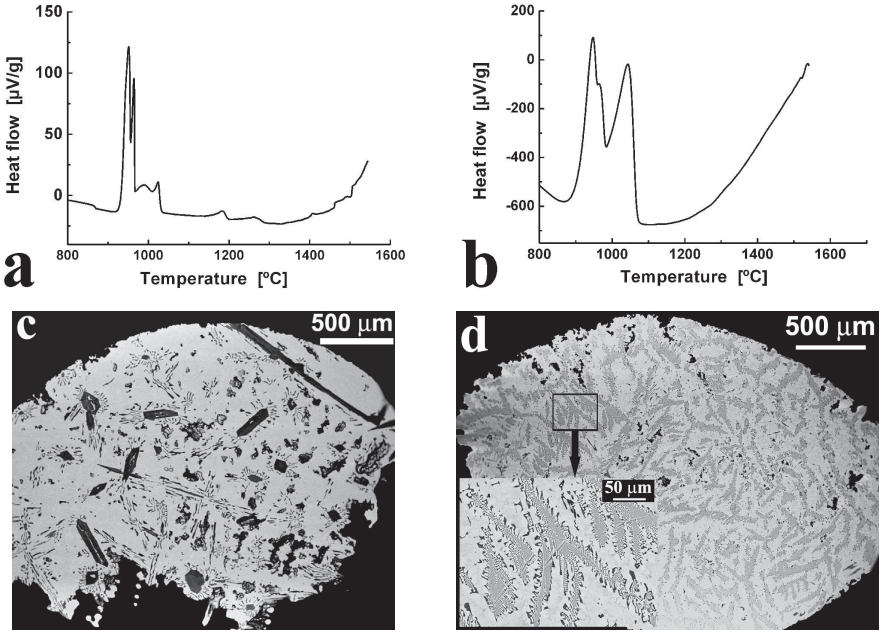

Figure 4.19. DTA graphs showing the thermal response of Colmonoy 69 cooled at (a)10 K/min and (b) 100 K/min. SEM microstructural images of the samples cooled at 10 and 100 K/min are shown in (c) and (d), respectively.

4.5.2.2 Single-track samples

Figure 4.20 shows the microstructure of single tracks deposited on preheated bars at deposition speeds of 5, 10 and 20 mm/s and on the cold bar at 5 mm/s. After deposition at 5 mm/s on preheated substrate, the microstructure consisted of blocky borides (mainly CrB). As shown in Figure 4.2(f), abrupt microstructural changes can occur in this alloy system. The same phenomenon happened from bottom to top of the single track deposited at 10 mm/s (Figure 4.20(b) and (c)). Microstructure of the track deposited at 20 mm/s on preheated bar contained very few blocky borides and majority of the microstructure consisted of floret-shape structures along with dendritic Cr_7C_3 (Figure 4.20(d)). The single track samples deposited on the cold bars at 5, 10 and 20 mm/s contained negligible amount of blocky borides. Figure 4.20(e) shows the SEM-BSE image from the microstructure of the single track deposited at the lowest cladding speed of this study (5 mm/s). The insets show that after a precipitate-free layer of columnar dendrites close to the interface, the microstructure contained only floret-shape structures plus numerous dendritic Cr_7C_3.

4.5.2.3 Powder particles

Figure 4.21(a) shows the SEM micrograph of the gas-atomized powder used in this study. The diameter of powder particles was in the range of 50-150 μm. Figure 4.21(b) to (d) show the microstructure of various powder particles. Although the powder particles were from the same batch and their diameters were comparable, different microstructures were formed during the atomization process. In the powder particle of Figure 4.21(b), CrB is the main boride precipitate along with some butterfly-shape Cr_5B_3 and flower-shape Cr_7C_3 as indicated by arrows. On the other hand, the powder particle in Figure 4.21(c) shows a mixture of several phases including large quantities of Cr_5B_3 as well as floret-shape structures and some CrB. The powder particle of Figure 4.21(d) has a microstructure consisting of the same phases as in (b) and (c) but in much larger numbers and significantly smaller sizes which shows that this particle experienced a significant amount of undercooling. The cooling rate of powder particles with a diameter of around 100 μm is between 10^3-10^5 K/s during gas atomization[35]. The microstructural images of Figure 4.21(b) to (d) show that even with the same chemistry and diameter, the melt droplets of Colmonoy 69 can develop significantly different phases and

microstructures. The morphology of constituent phases in the powder particles are very similar to that of the same phases formed during laser deposition.

4.6 Sequence of phase formation

Microstructural evidence and Thermo-Calc simulation were employed to predict the sequence of phase formation reactions in the intended alloy. Establishing a clear correlation between the experimental evidence and the simulation results requires more comprehensive Thermo-Calc analyses. Nevertheless, the general sequence of the phase formations can be predicted.

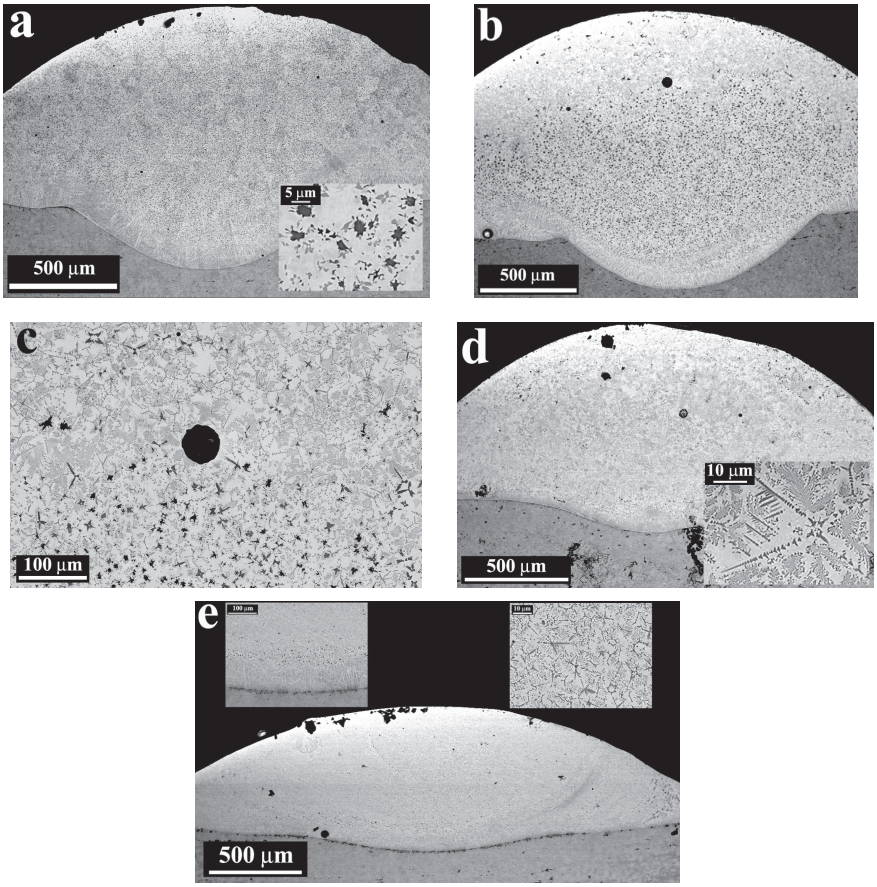

Figure 4.20. Microstructure of single-track samples deposited on preheated substrate at (a) 5 mm/s, and (b) 10 mm/s. (c) Close-up of the microstructural transition at the top of sample (b). (d) Microstructure of single-track sample deposited on preheated substrate at 20 mm/s, (e) Microstructure of single-track sample deposited on cold substrate at 5 mm/s.

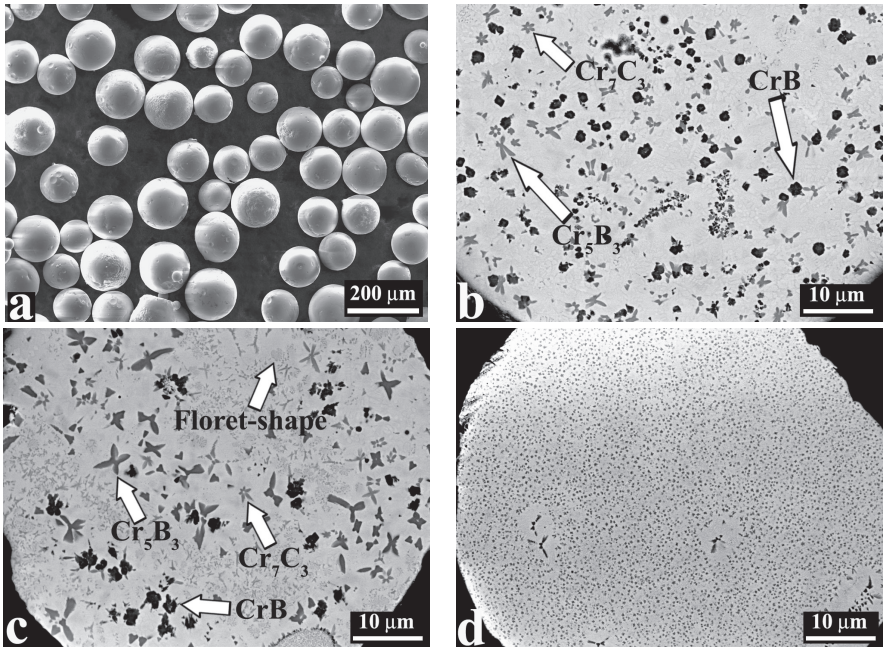

Figure 4.21. (a) SEM micrograph of the gas-atomized Colmonoy 69 powder particles, (b) to (d) BSE images showing the cross-section of several powder particles with various microstructures.

4.6.1 Peritectic transformation of CrB

The SEM-BSE image of Figure 4.22(a) shows a microstructure in which several boride precipitates are enveloped in other precipitates. Such a configuration is usually formed during peritectic reactions which the Cr-B system contains a number of them (Figure 4.1(c)). Based on the knowledge obtained so far about the prevalent types of borides in this system and also based on the contrast of the phases in the BSE image, it is possible to predict that the darker borides are CrB and the ones surrounding them are Cr_5B_3. In fact, the peritectic reaction of $L + CrB \rightarrow Cr_5B_3$ can be found in the binary Cr-B phase diagram at around 1900 ^oC as highlighted in Figure 4.22(b). EDS/EBSD phase identification was done to conclusively determine the type of the phases involved in these structures. Figure 4.22(c) shows the SEM image (70 ^{o} tilted) of a boride enveloping another precipitate with a darker contrast. According to the EBSD phase map of Figure 4.22(d), the larger precipitate is a single crystal Cr_5B_3 which surrounds a polycrystalline CrB.

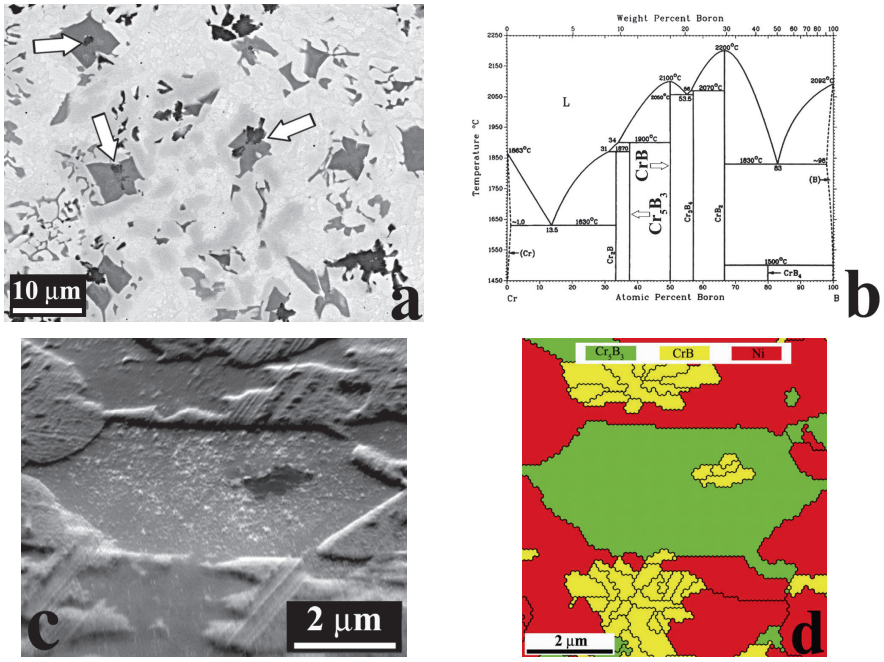

Figure 4.22. (a) SEM image showing multiple cases (highlighted by arrows) of boride precipitates enveloping another phase, (b) Cr-B phase diagram, (c) SEM image of one boride precipitate which surrounds another phase with a darker contrast, (d) EBSD phase map of the structure in (c) showing a CrB precipitate surrounded by Cr_5B_3 (boundary misorientation: 5 ^{o}).

It can be seen in Figure 4.22(a) that the peritectic transformation, i.e. thickening of the peritectic envelope[36] is in different stages for different precipitates. In some cases, CrB is almost entirely transformed to Cr_5B_3 while in other cases it is not even fully surrounded. This is because of the fact that once CrB is covered with a layer of Cr_5B_3, thickening of the Cr_5B_3 layer will be controlled by the diffusion of B, Cr and other elements through the layer. The microstructures represented in Figure 4.2(d) and Figure 4.22(a) show that Cr_5B_3 has formed either directly from the melt or through peritectic reaction.

4.6.2 Nucleation of Cr_7C_3 on Cr borides

Cr_7C_3 is the dominant type of carbide in this system as confirmed by EDS/EBSD and TEM results. Two morphologies of Cr_7C_3 could be found; a flower-shape one as shown in Figure 4.21(c) and dendritic ones as presented in Figure 4.23. The first morphology was common in microstructures with blocky borides while the dendritic morphology usually coexisted with floret-

shape structures (Figure 4.2(e)). An interesting feature of dendritic Cr_7C_3 was its nucleation on the existing CrB or Cr_5B_3 precipitates (Figure 4.23) showing that Cr_7C_3 formed at lower temperatures.

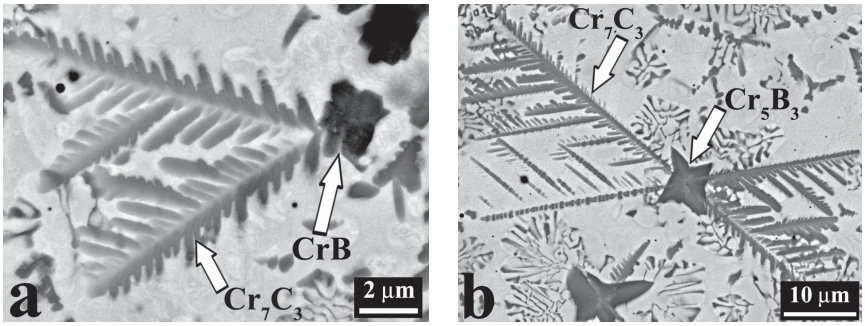

Figure 4.23. Nucleation of dendritic Cr_7C_3 on (a) CrB and (b) Cr_5B_3.

4.6.3 Thermo-Calc simulation

The equilibrium reactions for the actual composition of Colmonoy 69 were calculated using Thermo-Calc software. The phase fraction versus temperature graph is presented in Figure 4.24. Although other phases such as Cr_5B_3 or the eutectics were missing from the results, the simulation could predict CrB and Cr_7C_3. Formation of Cr_7C_3 at lower temperatures is in line with the microstructural observations in the previous section. Also the prediction on the wide solidification range of Colmonoy 69 agrees with the DTA results. The absence of low-temperature eutectic phases could be solved using Scheil solidification module which will be shown in the next chapter.

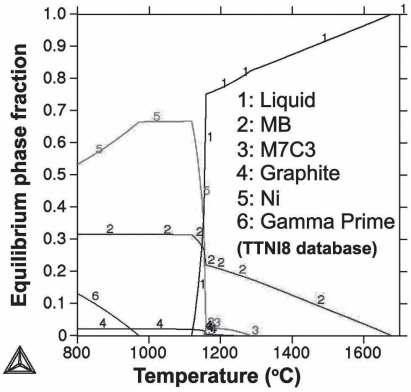

Figure 4.24. The equilibrium phase fraction versus temperature diagram for Colmonoy 69 calculated by Thermo-Calc.

4.7 Microstructure-hardness relationships

The implications of the microstructural changes for hardness of the deposits can be evaluated by measuring the microhardness from the bottom towards the top of the track in Figure 4.2(g). This track contained three distinctive regions: a precipitate-free layer of columnar dendrites of Ni next to the clad-substrate interface, a layer containing blocky borides and finally, majority of the deposit consisting of floret-shape structures and Cr_7C_3 dendrites. The hardness graph of Figure 4.25(a) similarly shows three regions: close to the interface with a hardness of around 500 HV, a second region of around 750 HV and a final part with the highest hardness of around 900 HV.

Observation of the individual hardness indents confirmed that the three hardness ranges in Figure 4.25(a) correspond to the three microstructural regions in Figure 4.2(g). The highest values of hardness belonged to the indents which were positioned entirely on the eutectic structures. The hardness indent of Figure 4.25(b) shows an example in which hardness was measured equal to 1073 HV. It seems that the eutectic structures contribute significantly to the hardness of this alloy. Consequently, the content and distribution of the eutectic phases should be explored in more details.

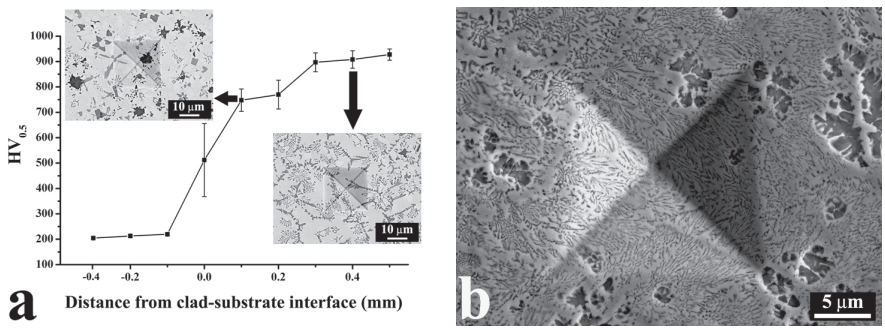

Figure 4.25. Variations of microhardness along the depth of the track shown in Figure 4.2(g), (b) An indent entirely located on the eutectic phases with a hardness of 1073 HV.

The eutectic phases in Colmonoy 69 coatings could be observed under SEM after etching as shown in Figure 4.8(a). It was also possible to clearly observe the eutectic network on the as-polished samples under OM (Figure 4.26). On the other hand, this network could not be properly distinguished in the SEM-BSE images. Hence, to observe all constituent phases of this alloy system, it was necessary to observe both as-polished and etched samples under SEM (in SE and BSE modes) as well as OM. The dark

phases in Figure 4.26 are Cr borides which are surrounded by Ni dendrites with a lighter contrast. The areas between the Ni grains are the eutectic phases. Although the details of the eutectic structures cannot be resolved Figure 4.26, the OM images provide the possibility of measuring the total area percentage of the eutectic phases. This percentage was calculated by image analysis to be approximately 20 and 35 for the microstructures in Figure 4.26(a) and (b), respectively. These numbers show that the microstructures with blocky borides or floret-shape structures are not only different in the type of their boride phases, but also in the amount of the eutectics which form at the latest stages of solidification. In Colmonoy 69 deposits, the highest hardness belonged to the microstructure shown in Figure 4.26(b) which contained the highest percentage of eutectics. Boride and carbide precipitates of Colmonoy 69 all have high hardness values (~ 2000 HV)[37,38]. So, the difference in the hardness of various microstructures of this alloy is most probably caused by variations in the percentage of eutectic phases in different microstructures.

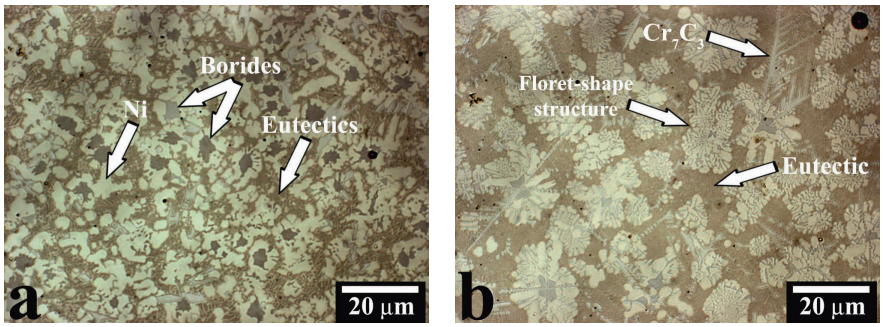

Figure 4.26. OM images of the microstructures shown in Figure 4.2(c) and (e). The difference in the amount of eutectics is noticeable.

It was shown that increasing the level of dilution diminished the content of both eutectics and precipitates in the microstructure of Colmonoy 69 deposits. Unsurprisingly, hardness of the deposits decreased at higher dilutions as shown in Figure 4.27.

4.8 Discussions

4.8.1 Mechanisms of microstructural evolution

The observed microstructures in laser deposited Colmonoy 69 coatings can be classified into two general categories: the ones with primary Cr boride/carbides which can be found in Cr-B and Cr-C phase diagrams (e.g.

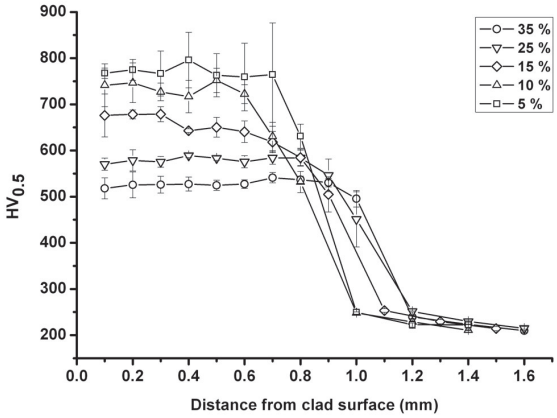

Figure 4.27. Hardness variations as a function of dilution.

CrB and Cr_5B_3) along with lower contents of Ni-B-Si eutectics (Figure 4.2(b) to (d), Figure 4.26(a)) and the one containing floret-shape structures and higher contents of Ni-B-Si eutectics (Figure 4.2(e) and Figure 4.26(b)). As both of these microstructures were also observed in the DTA samples, analysis of the relationship between thermal conditions and microstructural evolution can be started with the DTA samples in which the solidification conditions are relatively well-known.

The solidification path of this alloy is particularly complex and involves formation of several borides and carbide, Ni solid solution dendrites and Ni-B-Si binary and ternary eutectics. Due to this multiplicity of phases and the absence of an accurate multi-component phase diagram for this alloy system, a precise interpretation of DTA curves is not easy. The primary phases in this system are Cr borides and carbide. Absence of the thermal events in the DTA curve of the sample cooled at 100 K/min (Figure 4.19(b)) shows that increasing the cooling rate in this system can suppress the primary phase formation reactions. At higher cooling rates, most of the boron content was consumed to produce floret-shape structures as shown by the magnified section of Figure 4.19(d). These structures were characterized to be mixtures of Ni and Cr_5B_3 which could form through a metastable eutectic reaction at around 1100 ^{o}C. This temperature roughly corresponds to the onset temperature of the first peak in the DTA graph of Figure 4.19(b). The DTA peaks at temperatures less than 1000 ^{o}C belong to the Ni-B-Si binary and ternary eutectic reactions and do not show substantial differences for the two cooling rates. This means that the largest impact of the cooling rate on solidification pathway of this alloy was during formation of boride phases. In

other words, higher cooling rates suppressed the primary borides, i.e. blocky CrB and butterfly-shape Cr_5B_3 and encouraged the metastable reaction of boride formation at lower temperatures.

By extending the outcomes from analysis of the DTA samples to the single tracks deposited on both preheated and cold substrates, similar trends for the effect of cooling rate on phase formation could be observed. Figure 4.20 shows that transition from the first category of microstructures to the second one can occur inside a single track from bottom to top of the melt pool. At higher deposition rates, such a transition happened earlier, i.e. closer to the deposit-substrate interface. Consequently, while the single track deposited at 5 mm/s on preheated bar only contained the first category of microstructure (Figure 4.20(a)), the track deposited at 10 mm/s had a mixed microstructure (Figure 4.20(b) and (c)) and the one deposited at 20 mm/s entirely consisted of floret-shape structures plus dendritic carbides (Figure 4.20(d)). During deposition on cold substrates, the cooling rate has been so high that the primary borides were almost entirely suppressed (Figure 4.20(e)), even at the slowest deposition rate.

The microstructures presented in Figure 4.20(a) and (d) were formed at the lowest and the highest cladding speeds or substrate temperatures, respectively. Hence, they can be used to establish the microstructure-cooling rate relationships. The cooling rate at the middle of single-tracks deposited on preheated substrates at 5 and 20 mm/s was estimated by a simple laser melting model presented by Berjeza[39] using the parameters presented in Table 4.2. The cooling rates for microstructures presented in Figure 4.20(a) and (d) were estimated to be around $3.9*10^3$ K/s and $6.6*10^4$ K/s, respectively. These values are in the same range as calculated previously by Finite Element Modeling for laser-deposited coatings[3,13].

Table 4.2. The input parameters to estimate the cooling rates using the model presented by Berjeza[39] for single-track samples deposited on the substrate preheated to 500 ^oC. The thermal properties are extracted from [40].

Cladding speed (mm/s)	Laser power (W)	Beam diameter (mm)	Heat capacity (J/Kg.K)	Thermal conductivity at 1144 ^oK (W/m.K)	Density (g/mm3)
5	800	3.57	444	28.8	8.06
20	1400	3.57	444	28.8	8.06

Variations of solidification parameters from bottom to top of the melt pool as discussed in CHAPTER 1 can be used to explain the phase changes along the depth of single-track samples and CET in the Ni grains (Figure 4.17). The microstructural evolutions in the single-track samples showed that increasing the cooling rate both because of the variations in $G * V_n$ along the depth of the melt pool and as a result of deposition on cold substrates will suppress the blocky borides and encourage floret-shape structures. Furthermore, the reduction of G / V_n from bottom to top of the melt pool is responsible for CET in the Ni dendrites. The G / V_n ratio describes the level of interface instability and determines the solidification mode. As this ratio decreases, the planar solid-liquid interface becomes unstable. As a result, the microstructure can change from planar to cellular, then to columnar dendrites and finally to equiaxed dendrites[41] as observed in Figure 4.17.

Based on the findings for the relationships between the processing conditions and microstructures for DTA and single-track samples, it is possible to interpret the microstructural changes in the multi-track deposits. It was found that the microstructure consisting of floret-shape structures and dendritic Cr_7C_3 forms at higher cooling rates. This microstructure also occurred in the fourth and fifth tracks in the multi-track sample deposited at 5 mm/s (Figure 4.2) and even earlier in samples deposited at 10 and 20 mm/s. It seems reasonable to conclude that the cooling rate has increased as multi-track deposition on preheated bars proceeded. In other words, the effect of substrate cooling was more pronounced than the effect of heat accumulation so that the substrate cooled down below the initial preheating temperature of 500 ^{o}C. The cooling rate required for the microstructural transition was reached earlier at higher deposition speeds because the interface growth velocity (V_n) and hence the cooling rate ($G * V_n$) are directly proportional to the deposition speed[42].

4.8.2 Phase selection phenomena

Contrary to the CET which is a morphological change as a result of different levels of interface instability, transition of the boride precipitates from CrB to Cr_5B_3 and finally to floret-shape structures (mixtures of Cr_5B_3 and Ni) is a phase change. As the composition of the melt was approximately constant in most of the experiments, position of the melt in multi-component phase diagram did not significantly change. On the other hand, the two categories of

microstructures did not co-exist in the samples, i.e. in every condition one category was preferably formed. This means that the transitions in the type of the boride phases in this system as a consequence of variations in the thermal conditions can be regarded as a series of phase selection processes.

Formation of all the observed phases consists of nucleation and growth steps. Hence, the phase selection phenomena can be examined in terms of relative nucleation and growth kinetics of the competing phases. The phase selection phenomena can be nucleation-controlled, growth-controlled or both[43]. In alloy systems with numerous phases, competition in the nucleation-controlled regime is largely determined by the relative magnitudes of ΔG^*, i.e. the energy barrier to nucleation which can be represented as follows[44]:

$$\Delta G^* = \frac{16\pi\gamma_{SL}^3 T_m^2 f(\theta)}{3L_f^2 \Delta T^2} \qquad \textit{Eq. 4.1}$$

in which γ_{SL}, T_m, $f(\theta)$, L_f and ΔT are solid-liquid interface energy, melting temperature, factor related to the contact between nucleus and the catalytic surface, latent heat of fusion per unit volume and undercooling below the equilibrium melting point. *Eq. 4.1* shows that many parameters can play a role in determining which phase nucleates more easily. There is not enough thermodynamic data to fully compare the nucleation energy barrier of various borides and carbides observed in Colmonoy 69 coatings. But based on the microstructural evolutions and possibility of sudden changes in the type of constituent phases, it seems reasonable to assume that substantial differences exist between the properties of the observed phases such as their interfacial energy or preferred level of undercooling.

All transformations including solidification, either rapid or slow, involve some degrees of departure from global equilibrium[44]. During solidification of a liquid metal, the non-equilibrium effects or the level of liquid metastability can be evaluated by the amount of undercooling below the equilibrium melting point[45]. In fact, among the above-mentioned parameters, the solidification microstructure is closely related to the level of undercooling at the onset of nucleation[46]. While the amount of undercooling can be accurately controlled and measured in some processes (e.g. solidification of suspended liquid droplets[46]), the same measurement is not easy to perform during deposition on a substrate followed by continuous rapid cooling as happens in laser cladding process. However, the connection between undercooling and cooling rate can be used to predict the variations of undercooling during the laser deposition process. In general, increasing the

cooling rate tends to enhance undercooling[47]. As a result, the observed microstructural evolutions in samples solidified with higher cooling rates can be correlated to their higher level of undercooling.

Both nucleation and growth of the competing phases could be influenced by the level of undercooling. There are many examples for nucleation-controlled phase selection with increasing undercooling[44]. Similarly, growth of the phases can also be affected. If one phase grows much more rapidly than the other at higher undercoolings, that phase will finally dominate the microstructure. Sometimes, the ease of diffusion plays a role in selection of the final phase or microstructure, especially in alloys[47]. An example of this can be observed in the studied coatings in which the blocky Cr_5B_3 precipitates give way to the floret-shape structures as seen in Figure 4.28(a) and (b). The dark layers in the floret-shape structures are Cr_5B_3 which could form during a metastable eutectic reaction[34]. The thickness of these layers is around 100 nm and they are separated by layers of Ni solid solution. The diffusion length for the alloying elements is much shorter in such morphology in comparison to bulky Cr_5B_3 precipitates. This may explain why floret-shape structures became dominant although the bulky Cr_5B_3 particles were able to nucleate. EBSD data showed that when floret-shape structures overtake the blocky Cr_5B_3 precipitates, Cr_5B_3 layers inside the florets keep the same crystallographic orientation as the primary Cr_5B_3 precipitates. In other words, a new nucleation process did not happen and only the transition of the original phase to a more kinetically favorable structure occurred. Figure 4.29(a) presents an example of the transition from blocky Cr_5B_3 precipitates to floret-shape structures. The [001] IPF map of Figure 4.29(c) shows that there are two Cr_5B_3 grains at the center and the layers of Cr_5B_3 on each side follow the orientation of one of the two grains during their growth. This is an example of growth competition and shows that if the growth kinetics of the primary phase is not fast enough, it may be replaced or overtaken by another more rapid structure[47].

Not all floret-shape structures were formed by transition from blocky Cr_5B_3 precipitates. In many cases, they were formed directly from the melt as shown in Figure 4.28(c). These observations suggest that the floret-shape structures had a better chance of nucleation and/or growth at higher levels of undercooling.

Figure 4.28 and Figure 4.29 suggest that the transition in the boride formation reaction can happen during both nucleation and growth. In other words, the floret-shape phases can form either directly from the highly

undercooled melt or by outgrowing the blocky Cr_5B_3. Previous research showed that when the interface attachment kinetics of the competing phases are comparable, then the competitive nucleation principles apply but if there is a significant difference of two or three orders of magnitude in the interface growth kinetics, the phase selection process will be growth-controlled[43]. The differences in the interface attachment kinetics can be caused by several factors including the level of order in the phase (e.g. an ordered intermetallic phase versus a disordered solid solution) and the complexity of the crystal structure[43]. The layers of Cr_5B_3 in the floret-shape structures have the same crystal structure, level of structural order and even crystal orientation as the blocky Cr_5B_3. As a result, their interfaces with the melt should have similar mobility. However, the growth of their interfaces can still be influenced by the ease of diffusion as a result of their different length scales.

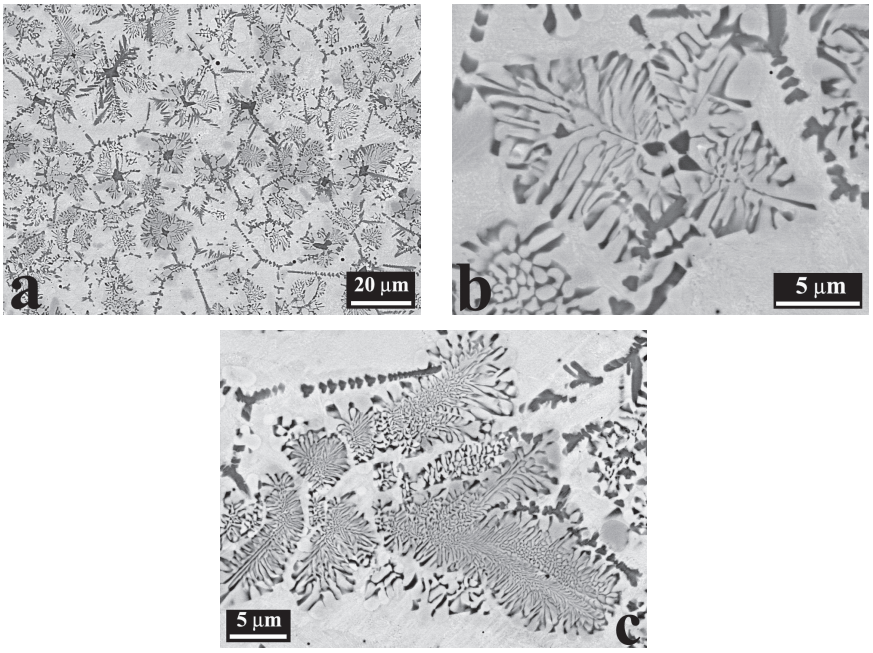

Figure 4.28. (a) SEM-BSE image showing how the floret-shape structures dominated the microstructure although many started as blocky Cr_5B_3. The dendritic phase is Cr_7C_3 (b) A close-up of a floret-shape structure which started as a blocky Cr_5B_3, (c) Direct formation of a floret-shape structure from the melt.

Most of the observed phases in this alloy system can be found in the relevant binary and ternary equilibrium phase diagrams[2,30,34]. While from the thermodynamics point of view all of the observed phases can form (either as

stable or metastable phases), at the end the kinetic and diffusion processes determined which of the possible phases and microstructures actually appeared. If the alloy composition has the potential to follow various phase formation pathways, different phase selection phenomena can occur as observed in the Colmony 69 laser deposited coatings. The wide solidification range of Colmonoy 69 can also provide the opportunity for the competing phase formation reactions to occur. Further analysis and experiments are necessary to clarify the exact mechanisms of phase selection during rapid solidification of Ni-Cr-B-Si hardfacing alloys.

Regarding the sequence of phase formation reactions, some conclusions can be made based on microstructural evidence and Thermo-Calc simulation. The peritectic transformation indicates that CrB was the first phase to solidify followed by Cr_5B_3. Furthermore, nucleation of Cr_7C_3 on either CrB or Cr_5B_3 as presented in Figure 4.23 shows that this phase formed at a lower temperature (as also calculated by Thermo-Calc) and nucleates on the existing CrB or Cr_5B_3 precipitates. Similarly, envelopes of Ni around the borides precipitates (Figure 4.26) can be regarded as a sign of their lower temperature of formation. If primary CrB or Cr_5B_3 was suppressed at higher undercoolings, Cr_7C_3 would be accompanied by the floret shape structures. The Ni-B-Si eutectics were the last phases to form in this alloy system under all conditions. They always formed a continuous network and filled the spaces between the precipitates and Ni dendrites or the floret shape structures.

As mentioned before, the two categories of microstructures did not co-exist. The microstructure with the blocky borides formed at a higher temperature range in comparison to that of the floret-shape structures. Formation of blocky borides depleted the melt out of boron and as a result, the first category of microstructures was free from floret-shape structures. On the other hand, the floret-shape structures could form only if formation of blocky borides was inhibited by increasing the cooling rate, i.e. providing the melt with more undercooling.

The DTA graphs of Figure 4.19 shows that the higher cooling rates mostly influenced formation of boride phases at higher temperatures. However, as nucleation and growth of the boride phases at the early stages of solidification determine the amount of boron remaining in the melt pool, the boride phase selection processes may have implications for the Ni-B eutectic reactions as well. In the microstructure of Figure 4.26(a), the dominant type of boride phase is CrB which contains around 17 wt.% of boron. On the other hand, the thin layers of Cr_5B_3 in the floret-shape structures of Figure 4.26(b)

contain around 11 wt.% of B[2]. Formation of a boride phase with lower boron content will keep more boron available for the Ni-B eutectic reactions at the final stages of solidification. This will increase the content of Ni-B-Si eutectics and also the portion of the harder Ni-B eutectic phases[30]. So, the higher percentage of the eutectic structures in the microstructure of Figure 4.26(b) in comparison to that of Figure 4.26(a) can be attributed to the different boride formation reactions of these two microstructures.

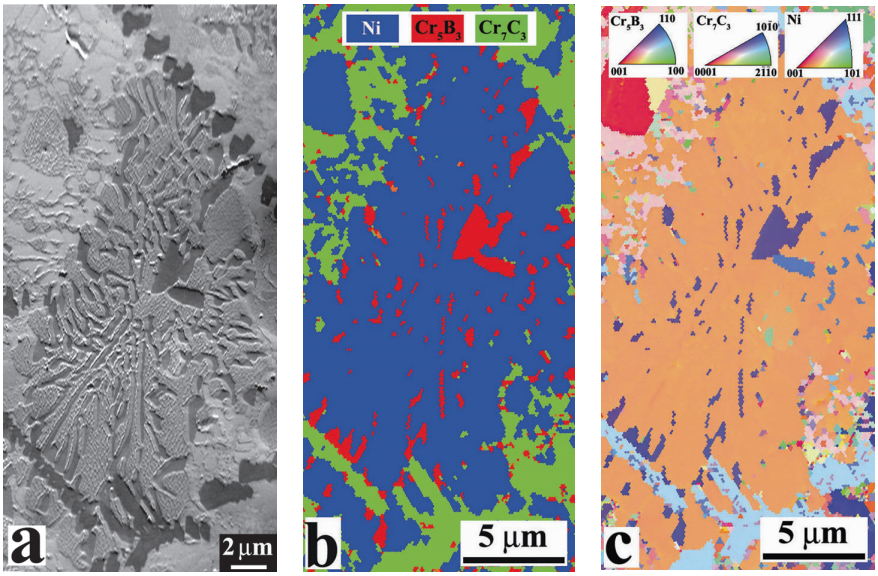

Figure 4.29. SEM image of a blocky Cr_5B_3 surrounded by a floret-shape structure, (b) phase map and (c) [001] IPF map of the area in (a). In (c), the way orientation of Cr_5B_3 layers follows that of the blocky precipitates is noticeable.

4.9 Issue with laser deposition of Colmonoy 69

The most important issue with laser deposited Colmonoy 69 coatings was high cracking susceptibility of the deposits. This issue (as will be discussed in detail in CHAPTER 5) was also the main motivation behind compositional modification of existing alloys and development of new alloys (CHAPTERS 5 & 6). The issue of high cracking tendency was also observed for coatings deposited from Colmonoy 56 (another high-alloy grade of Ni-Cr-B-Si-C family). It seems that high cracking tendency during laser deposition is a general characteristic of high-alloy grades of Ni-Cr-B-Si-C.

The second issue with laser deposited Colmonoy 69 coatings which was extensively addressed in the current chapter was microstructural instability. This means that microstructure of laser deposited Colmonoy 69 coatings is sensitive to variation of deposition conditions (deposition rate, substrate temperature, etc.) and their functional properties would not be uniform. The above-mentioned issues are more evident when these alloys are deposited by a process such as laser cladding which involves rapid solidification and fast solid-state cooling. Hence, some of the existing commercial Ni-Cr-B-Si-C alloys might need compositional adjustments to make them more suitable for laser deposition and similar technologies. Examples of such compositional modifications will be presented in the next chapters.

4.10 Conclusions

The microstructure and hardness of laser deposited Colmonoy 69 single- and multi-track coatings were studied experimentally. Detailed microstructural characterization and phase identification of submicron Ni-B-Si eutectic phases, micro-sized Cr boride and carbides and Ni dendrites were performed. Microstructural evolutions in the samples deposited at various cooling rates confirmed that higher cooling rates facilitated the preferential nucleation and growth of the floret-shape mixtures of Ni and Cr_5B_3 via a metastable reaction in comparison to precipitation of primary CrB and Cr_5B_3. Variation in the type of the borides also influenced the nature and proportion of the Ni-B-Si eutectics. Furthermore, higher iron contents as a result of higher dilution from the steel substrate diminished both precipitates and eutectics and reduced hardness of the deposits. Microstructural evidence such as peritectic transformation of CrB and nucleation of Cr_7C_3 on Cr borides indicated that the phase formation reactions started with precipitation of primary CrB and then Cr_5B_3 followed by Cr_7C_3, Ni solid solution dendrites and Ni-B-Si eutectics. Alternatively, the primary borides were substituted with the floret-shape mixtures of Ni and Cr_5B_3 at higher cooling rates.

Acknowledgements

Dr. Jiancun Rao (former colleague at Materials Science Group, University of Groningen, currently associate professor at Harbin Institute of Technology, China) is gratefully thanked for the TEM analyses. Dr. Kornel Csach

(Institute of Experimental Physics, Slovak Academy of Sciences, Slovakia) and Ake Jansson (Thermo-Calc Software) are appreciated for performing the DTA experiments and Thermo-calc simulation, respectively. Wall Colmonoy Ltd. (The UK) is acknowledged for providing Colmonoy 69 powder.

References

1. Liyanage, T.; Fisher, G.; Gerlich, A. P. Influence of Alloy Chemistry on Microstructure and Properties in NiCrBSi Overlay Coatings Deposited by Plasma Transferred Arc Welding (PTAW). *Surface and Coatings Technology* **2010**, *205*, 759–765.
2. *ASM Handbook-Alloy Phase Diagrams*; Baker, H., Ed.; 10th ed.; ASM International: Ohio, 1992; Vol. 3.
3. Kim, J. D.; Peng, Y. Temperature Field and Cooling Rate of Laser Cladding with Wire Feeding. *KSME International Journal* **2000**, *14*, 851–860.
4. El-Dasher, B. S.; Deal, A. Application of Electron Backscatter Diffraction to Phase Identification. In *Electron Backscatter Diffraction in Materials Science*; Schwartz, A. J.; Kumar, M.; Adams, B. L.; Field, D. P., Eds.; Plenum, 2000.
5. Dingley, D. Progressive Steps in the Development of Electron Backscatter Diffraction and Orientation Imaging Microscopy. *Journal of Microscopy* **2004**, *213*, 214–224.
6. Nowell, M. M.; Wright, S. I. Phase Differentiation via Combined EBSD and XEDS. *Journal of Microscopy* **2004**, *213*, 296–305.
7. Wright, S. I.; Nowell, M. M. EDS Assisted Phase Differentiation in Orientation Imaging Microscopy. *Materials Science Forum* **2006**, *509*, 11–16.
8. Kral, M. V.; McIntyre, H. R.; Smillie, M. J. Identification of Intermetallic Phases in a Eutectic Al-Si Casting Alloy Using Electron Backscatter Diffraction Pattern Analysis. *Scripta Materialia* **2004**, *51*, 215–219.
9. Laigo, J.; Tancret, F.; Gall, R. Le; Furtado, J. EBSD Phase Identification and Modeling of Precipitate Formation in HP Alloys. *Advanced Materials Research* **2007**, *15-17*, 702–707.
10. Kim, Y. H.; Kwun, S. I. Phase Analysis in the Region Brazed with Ni-14Cr-10Cr-3.5Al-2.5Ta-2.8B Filler Metal Using Electron Backscatter Diffraction. *Materials Science Forum* **2008**, *569*, 93–96.
11. Chen, C.-L.; Thomson, R. C. The Combined Use of EBSD and EDX Analyses for the Identification of Complex Intermetallic Phases in Multicomponent Al-Si Piston Alloys. *Journal of Alloys and Compounds* **2010**, *490*, 293–300.
12. Wang, D.; Liang, E.; Chao, M.; Yuan, B. Investigation on the Microstructure and Cracking Susceptibility of Laser-clad V2O5 /NiCrBSiC Alloy Coatings. *Surface and Coatings Technology* **2008**, *202*, 1371–1378.
13. Jendrzejewski, R.; Kreja, I.; Śliwiński, G. Temperature Distribution in Laser-clad Multi-layers. *Materials Science and Engineering A* **2004**, *379*, 313–320.
14. Sudha, C.; Shankar, P.; Rao, R. V. S.; Thirumurugesan, R.; Vijayalakshmi, M.; Raj, B. Microchemical and Microstructural Studies in a PTA Weld Overlay of Ni-Cr-Si-B Alloy on AISI 304L Stainless Steel. *Surface and Coatings Technology* **2008**, *202*, 2103–2112.
15. Chaliampalias, D.; Vourlias, G.; Pavlidou, E.; Skolianos, S.; Chrissafis, K.; Stergioudis, G. Comparative Examination of the Microstructure and High Temperature Oxidation Performance of NiCrBSi Flame Sprayed and Pack Cementation Coatings. *Applied Surface Science* **2009**, *255*, 3605–3612.
16. Serres, N.; Hlawka, F.; Costil, S.; Langlade, C.; MacHi, F. Microstructures of Metallic NiCrBSi Coatings Manufactured via Hybrid Plasma Spray and in Situ Laser Remelting Process. *Journal of Thermal Spray Technology* **2011**, *20*, 336–343.

17. Paul, C. P.; Jain, A.; Ganesh, P.; Negi, J.; Nath, A. K. Laser Rapid Manufacturing of Colmonoy-6 Components. *Optics and Lasers in Engineering* **2006**, *44*, 1096–1109.
18. Wang, D. -s.; Liang, E. -j.; Chao, M. -j.; Yuan, B. Investigation on the Microstructure and Cracking Susceptibility of Laser-clad V2O5 /NiCrBSiC Alloy Coatings. *Surface and Coatings Technology* **2008**, *202*, 1371–1378.
19. Lim, L. C.; Ming, Q.; Chen, Z. D. Microstructures of Laser-clad Nickel-based Hardfacing Alloys. *Surface and Coatings Technology* **1998**, *106*, 183–192.
20. Gurumoorthy, K.; Kamaraj, M.; Rao, K. P.; Venugopal, S. Microstructure and Wear Characteristics of Nickel Based Hardfacing Alloys Deposited by Plasma Transferred Arc Welding. *Materials Science and Technology* **2006**, *22*, 975–980.
21. Gurumoorthy, K.; Kamaraj, M.; Rao, K. P.; Rao, A. S.; Venugopal, S. Microstructural Aspects of Plasma Transferred Arc Surfaced Ni-based Hardfacing Alloy. *Materials Science and Engineering A* **2007**, *456*, 11–19.
22. Xu, G.; Kutsuna, M.; Liu, Z.; Zhang, H. Characteristics of Ni-based Coating Layer Formed by Laser and Plasma Cladding Processes. *Materials Science and Engineering A* **2006**, *417*, 63–72.
23. Das, C. R.; Albert, S. K.; Bhaduri, A. K.; Sudha, C.; Terrance, A. L. E. Characterisation of Nickel Based Hardfacing Deposits on Austenitic Stainless Steel. *Surface Engineering* **2005**, *21*, 290–296.
24. Klimek, L.; Pietrzyk, B. Electron Backscatter Diffraction as a Useful Method for Alloys Microstructure Characterization. *Journal of Alloys and Compounds* **2004**, *382*, 17–23.
25. Li, Q.; Zhang, D.; Lei, T.; Chen, C.; Chen, W. Comparison of Laser-clad and Furnace-melted Ni-based Alloy Microstructures. *Surface and Coatings Technology* **2001**, *137*, 122–135.
26. Cullity, B. D.; Stock, S. R. *Elements of X-Ray Diffraction*; 3rd ed.; Prentice Hall, 2001.
27. Pecharsky, V. K.; Zavalij, P. Y. *Fundamentals of Powder Diffraction and Structural Characterization of Materials*; Springer US: Boston, MA, 2009.
28. Palizdar, Y.; Cochrane, R. C.; Brydson, R.; Leary, R.; Scott, A. J. Accurate Analysis of EBSD Data for Phase Identification. *Journal of Physics: Conference Series* **2010**, *241*, 012104.
29. Tokunaga, T.; Nishio, K.; Hasebe, M. Thermodynamic Study of Phase Equilibria in the Ni-Si-B System. *Journal of Phase Equilibria* **2001**, *22*, 291–299.
30. Kanichi, T.; Hidaka, K. Hard Facing Nickel-Base Alloy **1984**.
31. Kaul, R.; Ganesh, P.; Albert, S. K.; Jaiswal, A.; Lalla, N. P.; Gupta, A.; Paul, C. P.; Nath, A. K. Laser Cladding of Austenitic Stainless Steel with Nickel Base Hardfacing Alloy. *Surface Engineering* **2003**, *19*, 269–273.
32. Kesavan, D.; Kamaraj, M. The Microstructure and High Temperature Wear Performance of a Nickel Base Hardfaced Coating. *Surface and Coatings Technology* **2010**, *204*, 4034–4043.
33. Conde, A.; Zubiri, F.; Damborenea, Y. J. De Cladding of Ni-Cr-B-Si Coatings with a High Power Diode Laser. *Materials Science and Engineering A* **2002**, *334*, 233–238.
34. Campbell, C. E.; Kattner, U. R. Assessment of the Cr-B System and Extrapolation to the Ni-Al-Cr-B Quaternary System. *Calphad* **2002**, *26*, 477–490.
35. Upadhyaya, G. S. *Powder Metallurgy Technology*; Cambridge International Science Pub.: Cambridge, 2002.

36. StJohn, D. H.; Hogan, L. M. The Peritectic Transformation. *Acta Metallurgica Et Materialia* **1977**, *25*, 77–81.
37. Pierson, H. O. *Handbook of Refractory Carbides and Nitrides: Properties, Characteristics, Processing, and Applications*; Noyes Publications: Park Ridge, N.J., 1996.
38. Gilman, J. J. *Chemistry and Physics of Mechanical Hardness*; Wiley series on processing of engineering materials; Wiley: Hoboken, N.J, 2009.
39. Berjeza, N. A.; Velikevitch, S. P.; Mazhukin, V. I.; Smurov, I.; Flamant, G. Influence of Temperature Gradient to Solidification Velocity Ratio on the Structure Transformation in Pulsed- and CW-laser Surface Treatment. *Applied Surface Science* **1995**, *86*, 303–309.
40. *ASM Ready Reference: Thermal Properties of Metals*; Cverna, F., Ed.; ASM materials data series; ASM International: Materials Park, Ohio, 2002.
41. Kou, S. *Welding Metallurgy*; Wiley-Interscience: New Jersey, 2003.
42. Kurz, W.; Trivedi, R. Rapid Solidification Processing and Microstructure Formation. *Materials Science and Engineering A* **1994**, *179-180*, 46–51.
43. Li, M.; Ozawa, S.; Kuribayashi, K. On Determining the Phase-selection Principle in Solidification from Undercooled Melts - Competitive Nucleation or Competitive Growth? *Philosophical Magazine Letters* **2004**, *84*, 483–493.
44. Perepezko, J.; Brewer, L.; Schaefer, R. Chapter 1 Principles Underlying Coatings and Surface Modification Science. *Materials Science and Engineering* **1985**, *70*, 9–22.
45. Herlach, D. M. Solidification from Undercooled Melts. *Materials Science and Engineering A* **1997**, *226-228*, 348–356.
46. Perepezko, J. H.; Sebright, J. L.; Höckel, P. G.; Wilde, G. Undercooling and Solidification of Atomized Liquid Droplets. *Materials Science and Engineering A* **2002**, *326*, 144–153.
47. Perepezko, J. H. Nucleation-controlled Reactions and Metastable Structures. *Progress in Materials Science* **2004**, *49*, 263–284.

Chapter 5

TACKLING THE CRACKING PROBLEM of Ni-Cr-B-Si-C COATINGS *

The focus of this chapter is on defining a procedure to select alloying elements for microstructural refinement of Ni-Cr-B-Si-C laser-deposited coatings and assessing the effectiveness of such a refinement as a toughening mechanism. It is shown that addition of Nb in specific quantities induces a significant microstructural refinement while preserving the original hardness. However, cracking susceptibility of the microstructurally-refined deposits was not decreased because the continuous network of hard eutectics still provided easy routes for crack growth. Hence, an effective toughening mechanism for Ni-Cr-B-Si-C alloy deposits should include not only refinement of the hard precipitates, but also modification of the eutectic structure.

---

* This chapter has been published in the following journal papers:

I. Hemmati, J.C. Rao, V. Ocelík, J.Th.M. De Hosson, Phase formation and properties of vanadium-modified Ni-Cr-B-Si-C laser deposited coatings, Journal of Materials Science 48 (2013) 3315–3326.

I. Hemmati, V. Ocelík, J.Th.M. De Hosson, Advances in Laser Surface Engineering: Tackling the Cracking Problem in Laser-Deposited Ni-Cr-B-Si-C Alloys, JOM 65 (2013) 741-748.

I. Hemmati, V. Ocelík, J. Th. M. De Hosson, Toughening mechanism for Ni-Cr-B-Si-C laser deposited coatings, Materials Science & Engineering A 582 (2013) 305-315.

V. Ocelík, M. Eekma, I. Hemmati, J.Th.M. De Hosson, Elimination of Start/Stop defects in laser cladding, Surface & Coatings Technology 206 (2012) 2403-2409.

I. Hemmati, R. M. Huizenga, V. Ocelík, J. Th. M. De Hosson, Microstructural design of hardfacing Ni-Cr-B-Si-C alloys, Acta Materialia 61 (2013) 6061-6070.

5.1 Introduction

IN the previous chapter, high cracking tendency and microstructural instability were mentioned to be the main issues in laser cladding of high-alloy grades of Ni-Cr-B-Si-C such as Colmonoy 69. The underpinning mechanisms for the latter issue were also discussed. Complicated phase formation reactions of Ni-Cr-B-Si-C alloys and their possibility of following various solidification paths imply that a very precise control of deposition conditions is needed to obtain the desired microstructure. This in turn necessitates a thorough understanding of how various microstructures shown in CHAPTER 4 are formed. Even if the issue of microstructural instability was resolved, the cracking problem still remains. Hence, the focus of this chapter is on tackling the cracking problem of laser-deposited Ni-Cr-B-Si-C coatings.

In laser-deposited coating, cracking occurs either during solidification or/and during the solid-state cooling[1]. In the former case, interdendritic phases (e.g. sulfides in steels) can not resist the tensile stress in the clad layer which results in interdendritic fracture. In the case of laser-deposited Ni-base coatings, cracking occurs during the solid-state cooling when the residual tensile stress exceeds the Ultimate Tensile Strength (UTS) of the clad material[1].

Residual stresses are stresses which remain in the sample after external forces are removed[2]. These stresses originate from misfit between different regions of the sample as a result of nonuniform plastic deformation or sharp thermal gradients. Such a misfit can also occur because of phase transformation, radiation or electromagnetic field exposure[2]. In the case of laser-deposited coatings, the major source of residual stresses is the differential thermal contractions of the coating and the substrate (each constrained by the other) caused by steep temperature gradients and different thermal expansion coefficients of coating and substrate materials[2–4]. Thermal stresses in a clad layer can be generally expressed as follows:

$$\sigma_{th} = \frac{E.\Delta\alpha.\Delta T}{1-\nu} \qquad \textit{Eq. 5.1}$$

where E and ν are elastic modulus and Poisson's ratio of the clad material, and $\Delta\alpha$ and ΔT are differences in linear thermal expansion coefficient and temperature between clad and its substrate, respectively[4]. In many cases, $\Delta\alpha$ is a function of temperature and hence, σ_{th} should be calculated by integration over the intended temperature range[5]. In the case of coatings on a

substrate, σ_{th} is tensile when thermal expansion coefficient of the coating is larger than that of the substrate, for example in deposition of Ni-base alloys on carbon steel (α for Ni-base alloys and carbon steel are in the ranges of 13.3-16.8 and 11.3-12.2 (10^{-6} K^{-1}), respectively[4]). In addition, increasing the cladding speed or deposition on substrates at lower temperatures increases σ_{th}. This happens because sharper temperature gradients will be established between clad and its substrate and hence, larger ΔT (and probably $\Delta\alpha$) will be generated[3,6–8].

Initiation and propagation of cracks in laser-deposited coatings depend on the magnitude of residual tensile stress, mechanical properties of the clad layer (mainly toughness) and to a lesser extent on the amount of defects (e.g. large pores) in the clad layer. Cracking phenomenon is mainly caused by a combination of high residual tensile stresses and low fracture toughness. Consequently, two main approaches can be followed to solve the cracking problem in laser-deposited coatings, i.e. decreasing residual tensile stresses in the deposits or increasing the fracture toughness of the deposited alloy. The former approach has been used extensively using preheating and/or postheating. A good example of this is the induction preheating as mentioned in CHAPTER 1. Although preheating is an effective and widely-used method to prevent cracking, it makes the process cumbersome and more expensive. It would be more preferable if the hardfacing alloy itself is so tough that the deposited coating can resist the thermal stresses without cracking. In hardfacing coatings where having high hardness is essential; this should ideally be realized without a significant loss of hardness.

In engineering materials, there is an inverse relationship between the hardness and fracture toughness, i.e. hard materials usually have low resistance against cracking[9]. As a result, developing high-hardness and high-toughness hardfacing alloys poses a sort of paradox. In normal circumstances, obtaining crack-free coatings with a relatively high level of hardness would be difficult unless the magnitude of the residual stresses is reduced substantially by proper preheating and/or postheating. However, if the hardness-toughness paradox is resolved (at least partially), hard and tough coatings can be deposited by laser cladding with little or no preheating of the substrate.

The main objective of this chapter is to explore whether a Ni-Cr-B-Si-C alloy can be developed, which has a combination of high hardness and high toughness capable of producing crack-free laser-deposited coating. To realize this goal, microstructural aspects of the cracking process are explored to find

a suitable toughening mechanism. In addition, other approaches such as preheating/postheating and elimination of stress concentration sites in the clad layers are employed as needed.

5.2 Strategies to prevent cracking

The following three approaches were adopted to prevent cracking in Ni-base alloy deposits. The focus was on Colmonoy 69 although other alloys were also explored.

5.2.1 Preheating

Previous research showed that in high-alloy Ni-Cr-B-Si-C laser-deposited coatings, most of the cracks form in the temperature range of 400-600 ^{o}C[1]. As a result, variations in the cracking rate of Colmonoy 69 coatings deposited on steel substrates preheated to 500 ^{o}C were studied. In the subsequent experiments (on Colmonoy 69 and other alloys), preheating temperatures of both higher and lower than 500 ^{o}C were used based on the previous outcomes.

5.2.2 Removing defects and stress concentration sites

It was observed that sharp corners at the beginning and end of the clad layer as well as defects such as large pores facilitate the cracking process (as highlighted by arrows in Figure 5.1) because these can act as local stress concentration sites. The large pores in the clad layer can be removed by optimizing the deposition parameters and the use of starting powders without significant number of hollow particles. Furthermore, some strategies were tested to remove the sharp corners at the sides of the clad layers.

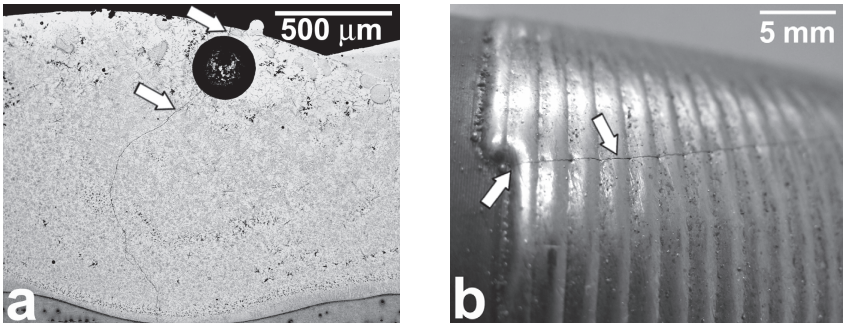

Figure 5.1. (a) Crack propagation through a large pore (Backscatter Electron image), (b) Crack initiation from the sharp corner at clad starting point.

5.2.3 Microstructural refinement

As aforementioned, the focus of the current chapter is on understanding how to improve the toughness of high-alloy Ni-Cr-B-Si-C coatings. The goal is to obtain crack-free coatings preferably without further precautions such as preheating. This should also be reached without a significant loss of hardness. To get an idea on how to achieve these goals, microstructural aspects of the cracking phenomena in laser-deposited Colmonoy 69 coatings were studied in detail using Scanning Electron Microscopy (SEM) in Secondary Electron (SE) and Backscatter Electron (BSE) imaging modes. It was observed that Cr boride and carbide precipitates (e.g. CrB, Cr_5B_3 and Cr_7C_3) actively contributed to generation and propagation of cracks in the microstructure of Colmonoy 69 coatings as shown in Figure 5.2. The constituent phases of Colmonoy 69 coatings were characterized in detail in CHAPTER 4. Hence, in the current chapter and the next one, types of the relevant phases are mentioned based on morphology and contrast in the SEM images.

Figure 5.2 shows that cracking of Colmonoy 69 coatings consists of a series of cracking phenomena in which the crack expands from one precipitate to the neighboring one. The role of large Cr boride and carbide precipitates as crack nucleation sites and easy routes for crack growth has also been mentioned in previous research[10–12].The stress concentration at the tip of an individual fractured Cr-rich precipitate will determine the probability of crack propagation. The maximum stress σ_m at the crack tip in a brittle phase is directly proportional to the crack length, and can be described as[13]:

$$\sigma_m = 2\sigma_a \left(\frac{a}{2\rho_c} \right)^{0.5} \qquad \textit{Eq. 5.2}$$

where σ_a is the applied stress, ρ_c crack tip radius of curvature and a length of the crack, i.e. size of the precipitate.

Given the active contribution of Cr-rich precipitates to the cracking phenomena, it is expected to observe improvements in cracking susceptibility of the deposits with refined precipitates, i.e. smaller a. So, one idea to reduce the cracking susceptibility of the intended coatings is to refine their microstructure, i.e. to reduce the structural scale of the Cr-rich boride and carbide precipitates. These precipitates form by nucleation and growth. If the number of the nuclei is increased, the same amount of precipitates will form at a higher number and hence, at smaller sizes. So, providing the precipitates with some nucleation sites could potentially refine them. Other boride and

carbide phases forming at higher temperatures than their Cr-rich counterparts could be good candidate nucleating agents. For this purpose, three Early Transition Metals (ETMs) were added to Colmonoy 69 either during powder production step or during laser cladding using two powder feeding hoppers. The results of these modifications constitute the majority of this chapter.

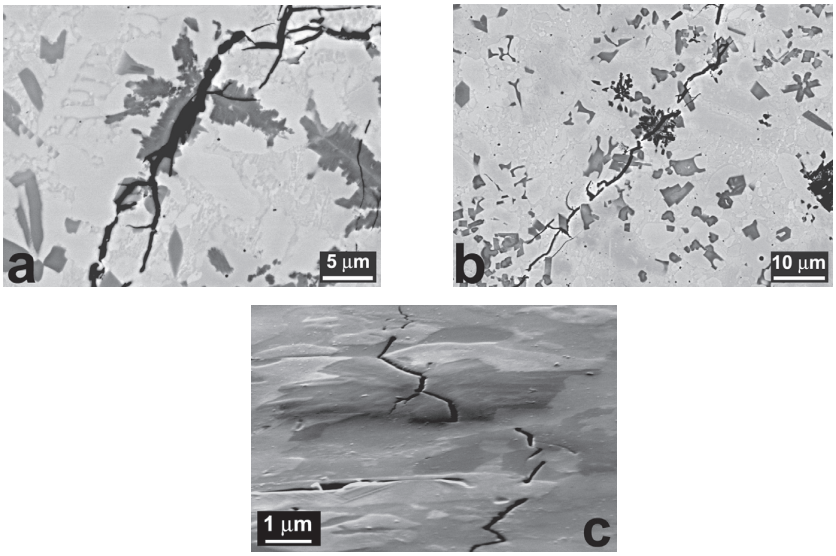

Figure 5.2. The role of Cr-rich precipitates in crack propagation in Colmonoy 69 laser-deposited coatings: (a) and (b) BSE images, (c) SE image (70 ^{o} tilted).

5.2.3.1 Theoretical backgrounds for selection of refining elements

In this section, the procedure for selection of potential refining elements for Ni-Cr-B-Si-C alloys will be explained and the outcomes will be summarized as a number of rules. The procedure can also be applied to produce in-situ formed nucleation agents in similar alloy systems. In order to find potential refining elements, the focus will be on ETMs as most of them are strong boride and carbide formers[14–16].

It has been previously suggested that the primary criterion to select the refining element for Ni-Cr-B-Si-C alloys is that the element should have a high affinity for B or C[17,18], i.e. the Gibbs free energy of formation (ΔG_f) for borides or carbides of that element should be more negative than those of Cr-rich precipitates[19]. This would allow for spontaneous and preferential formation. Such borides or carbides could subsequently act as nucleation sites for Cr-rich precipitates. Figure 5.3 shows the ΔG_f values for borides and

carbides of several ETMs. It can be seen that vanadium borides have some of the largest values of ΔG_f in all ETMs. In fact, vanadium addition is the limit for the idea of microstructural refinement in Ni-Cr-B-Si-C alloys according to the ΔG_f criterion alone.

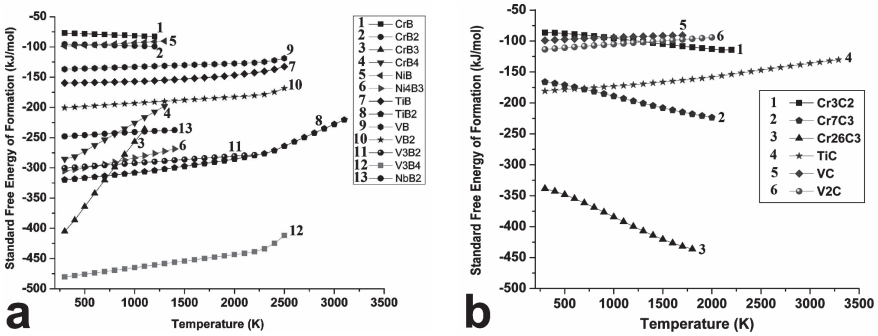

Figure 5.3. The Gibbs free energy of formation for (a) borides and (b) carbides of some transition metals[20].

The outcome of vanadium addition to Colmonoy 69, which will be discussed in section 5.4.2 showed that other criteria such as mutual solid solubility of the precipitates or their temperature of formation should also be considered. Hence, the original criterion of the refining element, i.e. forming boride/carbide phases with large negative values of ΔG_f was revised and expanded to the set of rules as explained below.

A refining element for Ni-Cr-B-Si-C alloys should fulfill at least the following three criteria, which will be subsequently elaborated and applied to select the potential candidate ETM refining elements more precisely:

(i) Affinity of the refining element for B or C should be higher than affinity of Cr for these elements, i.e. it should have the possibility of preferential formation of borides or carbides during solidification.

(ii) The boride or carbide precipitates of the refining element should have a limited solid solubility in their Cr-rich counterparts.

(iii) The boride or carbide precipitates of the refining element should form at a higher temperature in comparison to Cr-rich precipitates.

The affinity of ETMs for C is the highest for valence number of 4 and decreases for higher valences as explained by Cottrell[14]. According to Table 5.1, titanium (Ti), zirconium (Zr) and hafnium (Hf) should have the highest affinity for C. In addition, tantalum (Ta) and niobium (Nb) should be stronger carbide formers than Cr. The data on heats of formation (ΔH) of carbides

such as ZrC, TiC, HfC and NbC confirm such predictions[14,20]. Similarly, the affinity of Ti, Zr, Nb and Hf for boron is stronger than that of Cr[16,20].

If a solid solution forms between Cr borides/carbides and boride/carbides of other ETMs, the ETM atoms substitute Cr atoms. Hume-Rothery (H-R) rules for substitutional solid solutions (size, electronegativity and valence or electron concentration factors[21]) and their derivatives such as the methods developed by Darken and Gurry[22] and Chelikowsky[23] were used as guidelines to judge the extent of solid solubility [24].

The difference of electronegativity between Cr and the rest of the ETMs is less than 0.4 (Table 5.1). Hence, according to the Darken-Gurry criteria[24], electronegativity will play a negligible role in determining the level of solid solubility when Cr and the other ETMs are substituted in each others compounds. The valences of transition metals are variable and complex and due to the valence complication caused by partially filled *d* orbitals, the transition metal alloys generally do not follow the valence rule when alloyed with other transition metals[24]. As a result, atomic size seems to be the predominant factor in determining the extent of solid solubility. However, the phase constitution of the V-modified system showed that the crystal structure of the phases should also be considered (section 5.4.2). In other words, while the size factor for vanadium calculated as $\Delta r_V = (r_{Cr} - r_V)/r_{Cr}$ is equal to 5.5 % (well within the favorable range[21]), VC and Cr_7C_3 had little solubility as a result of their different crystal structures. Hence, similarity of the crystal structures should also be considered.

Several ETMs were skipped because of various reasons. Modification of Ni-Cr-B-Si-C alloys by Ti[17] and Ta[18] have been previously done without success. Mo and W were also skipped because none is a strong carbide or boride former[14]. On the other hand, Zr and Hf are very strong carbide and boride formers (Table 5.1 and ref. [16]) and have the most unfavorable size factors (i.e. favorable for limited solubility in Cr-rich phases). The industrial-grade Zr contains Hf as a natural impurity. So, pure Hf was also skipped. Zr borides and carbide (e.g. ZrB_2 and ZrC) have crystal structures different from their Cr-rich counterparts[15,16]. Consequently, a strong segregation of Cr-rich and Zr-rich precipitates is expected (as already confirmed experimentally[25]). Finally, Nb has a high affinity for boron and carbon (Table 5.1 and ref. [16]) and an unfavorable size factor. Nb may form multiple borides/carbides which all have very limited solubility in their Cr-rich counterparts[26,27]. Hence, Zr- and Nb-rich precipitates are expected to remain as independent phases and provide potential nucleation sites.

Table 5.1. Properties of Early Transition Metals (ETMs) from group IV to VI. r, Δr, E and V are atomic size, size factor ($\Delta r_{ETM} = (r_{Cr} - r_{ETM}) / r_{Cr}$), Electronegativity and Valence, respectively[15].

ETM	r (nm)	Δr_{ETM} (%)	Electron configuration	E	V
Cr	0.126	-	$[Ar]3d^5 4s^1$	1.6	6
V	0.133	5.5	$[Ar]\ 3d^3\ 4s^2$	1.6	5
Ti	0.146	15.8	$[Ar]\ 3d^2\ 4s^2$	1.5	4
Mo	0.138	9.5	$[Kr]\ 4d^5\ 5s^1$	1.8	6
Nb	0.145	15	$[Kr]\ 4d^4\ 5s^1$	1.6	5
Zr	0.159	26.1	$[Kr]\ 4d^2\ 5s^2$	1.4	4
W	0.139	10.3	$[Xe]4f^{14}\ 5d^4\ 6s^2$	1.7	6
Ta	0.145	15	$[Xe]4f^{14}\ 5d^3\ 6s^2$	1.5	5
Hf	0.158	25.3	$[Xe]4f^{14}\ 5d^2\ 6s^2$	1.3	4

Zr or Nb boride/carbides should also precipitate at a high enough temperatures. Both Zr and Nb form borides/carbides at very high temperatures (e.g. above 3000 ^oC). However, the temperatures of boride/carbide precipitation, especially for Zr, drop very quickly by slight variations in the alloy composition[28–30]. So, the phase formation reactions should be evaluated for the specific alloy. For this purpose, the sequence of phase formation reactions in the alloys modified by 5 wt.% of Zr or Nb were simulated using *Thermo-Calc*® software (version S, database TTNI version 6.3). In addition to calculations based on the lever rule, the Scheil module was employed to investigate the phase formation reactions in non-equilibrium solidification conditions based on the well-known Scheil-Gulliver model[31] with B and C as fast-diffusing elements.

The results of thermodynamic calculations over the entire solidification range are shown in Figure 5.4. For both Zr and Nb additions, the calculated precipitation reactions based on equilibrium and Scheil solidification models were very similar. However, predictions for low-temperature reactions including eutectic ones (e.g. formation of Ni_3B) were different. In the case of Zr-modified system, ZrB_2 is expected to solidify first and for the Nb-modified deposits, NbC should form simultaneously with CrB. So, both Zr and Nb could form phases at the earliest stages of solidification

which may provide heterogeneous nucleation sites for the Cr-rich precipitates. Based on the above-mentioned discussions, Nb and Zr were selected for the second round of compositional modifications.

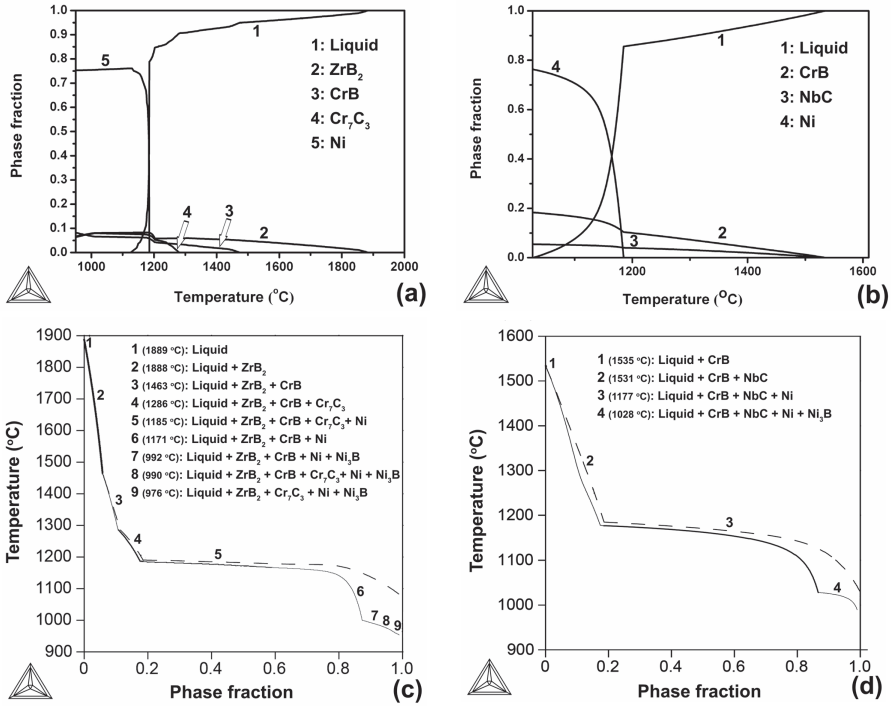

Figure 5.4. Calculated equilibrium phase fraction versus temperature for alloys modified by (a) 5 wt.% Zr or (b) 5 wt.% Nb. (c) and (d) show the solidification sequence of the same alloys as in (a) and (b) according to the Scheil-Gulliver solidification model.Dashed lines show the equilibrium reactions.

5.3 Experimental procedure

Two series of cladding experiments were done. The first series concentrated on deposition strategies to eliminate the cracking caused by the sharp corners at the beginning and at the end of the clad layer (Figure 5.1(b)). These experiments were done in the framework of a research project to eliminate start/stop defects (e.g. cracking, inhomogeneous clad thickness and hardness) in cladding of closed loops such as those encountered in laser cladding of valve seats. Figure 5.5 graphically represents the applied strategies. A schematic longitudinal cross section of the start/stop zone and variations of the main processing parameters during cladding of a circular track are

presented. The first strategy is called “laser after motion” in which the laser beam appears after substrate started to move and the beam is stopped when the substrate is still in motion. In the second approach called “gradient power”, laser power is gradually increased at the beginning and gradually decreased at the end of the process. “Variable defocus” is the third approach. It follows the same idea as the previous one, but gradual change of the laser beam intensity is realized via changing of laser beam defocus while keeping the laser power constant. The forth strategy is remelting of the start-stop zone using laser beam without powder injection. The outcomes of this section were used to remove the sharp edges at the beginning and the end of clad layers.

Laser cladding experiments of this part were carried out on 40-mm-diameter AISI 304 stainless steel bars using two different commercial powders: tool steel MicroMelt 23 (MM23) and Co-base Eutroloy 16012. Chemical compositions of these two powders and the substrate material are shown in Table 5.2. Samples were deposited at 5 mm/s using the IPG Fiber laser and side-cladding powder injection nozzle. Thickness, interface profile, microstructure, hardness and composition of clad layers in the overlapping areas were analyzed using Optical Microscopy (OM), Scanning Electron Microscopy (SEM), Energy Dispersive Spectroscopy (EDS) and Vickers hardness measurements.

The second series of experiments was focused on depositing modified Colmonoy 69 coatings. These modifications were done by addition of V, Zr or Nb. V-modified Colmonoy 69 powders containing 2 and 5 wt.% of V were produced by Wall Colmonoy Ltd. (The UK) using gas atomization. V-modified powders were deposited using laser powers of 800-1600 W at cladding speeds of 5, 10 and 20 mm/s on substrates at room temperature and preheated to 200 ^{o}C and 500 ^{o}C. In all cases, the powder feeding rate and laser power were adjusted to obtain clad layers with 0.9-1.1 mm thickness and less than 10% dilution.

Additions of up to 5 wt.% Zr or up to 10 wt.% Nb were made during the laser cladding process by simultaneous injection of Colmonoy 69 and industrial-grade Zr (Zr+Hf > 99 wt.%) or Colmonoy 69 and commercially-pure Nb powders. The powder feeding system consisted of two hoppers and a mixing cyclone just before the powder injection nozzle. Zr- and Nb-modified coatings were deposited at 5 mm/s on S355 steel bars at room temperature as well as preheated to 500 ^{o}C. The laser powers of 800 W (for preheated substrates) and 900 W (for cold substrates) were used. Thickness and dilution of the clad layers were the same as those for V-modified deposits.

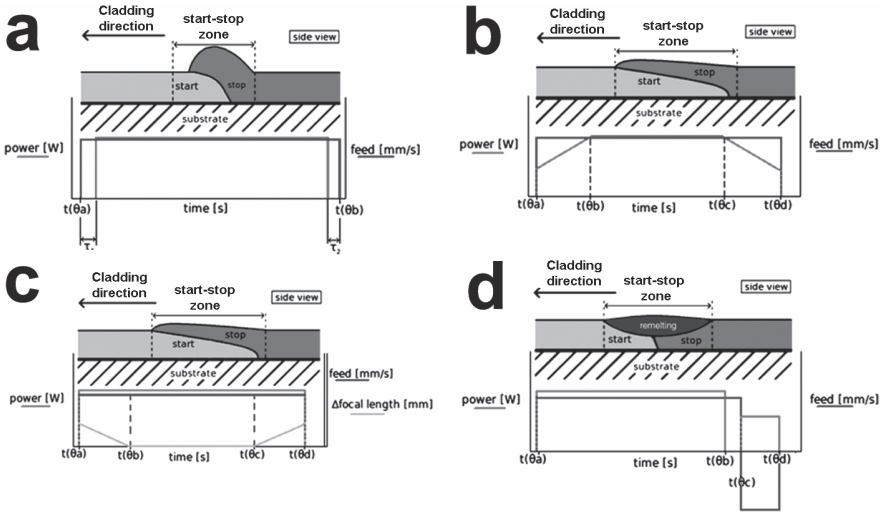

Figure 5.5. Four different strategies to treat the start/stop zone: (a) Laser after motion, (b) Gradient power; (c) Variable defocus, and (d) Remelting.

Table 5.2. Nominal chemical composition (in wt. %) of Eutroloy 16012, MicroMelt 23 (MM 23) and steel substrate.

Material	Co	Fe	Cr	W	C	Si	Ni	Mo	V	Mn	Cu
Eutroloy 16012	Bal.	<1	29.5	8.5	1.6	1.2	<1	-	-	-	-
MM 23	-	Bal	4.2	6.5	1.3	0.6	0.28	5	3.1	0.37	0.16
SS304	-	Bal	17.8	-	<0.08	0.7	8.0	-	-	1.7	0.6

Microstructure and compositional distribution of the modified coatings were studied by SEM and EDS. SEM microstructural analyses were performed using both SE and BSE imaging modes (and their combination). The effect of vanadium addition on phase constitution of the V-modified coatings was studied by Transmission Electron Microscopy (TEM). Thin foils for TEM observation were prepared by conventional mechanical grinding with SiC abrasive papers and finalized by ion milling at 4 kV in PIPS 691 system (Gatan Inc., USA). The grinding steps were performed on the deposits from bottom and top to ensure that the magnetic substrate (ferritic steel) and the iron-rich layers close to the clad-substrate interface were removed and the thin foils were collected from the center of the deposit. A JEM 2010F TEM operating at 200 kV equipped with an EDS system (127 eV resolution, Bruker

Co., USA) was used for high-resolution TEM observations, selected area electron diffraction (SAED) and compositional analyses. The TEM-EDS analyses were performed under the nano-beam setting with the fine electron beam size of 0.5 nm in diameter.

Mutual solubility of the phases in Zr- and Nb-modified coatings was evaluated by quantitative SEM-EDS. To ensure the accuracy and reliability of the EDS measurements, the following steps were taken:

(i) Large precipitates were analyzed to reduce the matrix effects.

(ii) An accelerating voltage of 5 kV was used to increase the amount of boron and carbon X-ray signals and maximize the sensitivity of the detector for low-energy X-ray of these elements.

(iii) Standardless Element Coefficients (SEC) of 4 for boron and 2 for carbon were applied in the *EDAX Genesis*® software to compensate for the limited detector accuracy for X-ray lines below 1 keV.

(iv) The Halographic Peak Deconvolution (HPD) function in the *EDAX Genesis*® software was used for comparing the model EDS spectra with the experimental ones in order to distinguish the overlaps between B-K and Zr-M or B-K and Nb-M peaks.

Furthermore, a combination of EDS and Electron Backscatter Diffraction (EBSD) was used for identification of Zr- and Nb-rich precipitates according to the procedure explained in CHAPTER 4.

An attempt was made to measure the fracture toughness of Colmonoy 69 coatings using Palmqvist indentation technique[32] which was not very successful. Hence, the cracking rate was measured as number of cracks per unit area of the clad layer after counting the cracks under a low-magnification (20x) OM. Finally, Hardness of the coatings was measured using Vickers indenter at a load of 4.9 N.

5.4 Results

5.4.1 Processing strategies

The proposed strategies were evaluated based on their effects on hardness, thickness and shape of the interface between substrate and coating (substrate interface) and inside the coating between overlapping tracks. The results are summarized in Table 5.3. The gradient power and variable defocus showed improvements in all criteria in comparison to the standard deposition method, i.e. movement of the substrate after laser irradiation. To deposit multi-track coatings, gradient power and remelting were used to smooth the sharp edges

at the beginning and the end of clad layer. However, the improvements in cracking of the clad layers were not significant or consistent.

Table 5.3. Evaluation of the experimental strategies to remove the start/stop defects. +, - and N denote positive, negative or neutral effect of the method in comparison to the standard deposition technique.

Strategy	I. Hardness change		II. Uniform thickness		III. Substrate interface		IV. Coating interface	
	MM23	Co	MM23	Co	MM23	Co	MM23	Co
Laser after motion	−	−	−	−	−	−	−	−
Gradient power	+	+	+	+	+	+	+	+
Variable defocus	+	+	+	+	+	+	+	+
Remelting	−	+	−	+	N	N	+	+

5.4.2 V-modified coatings

5.4.2.1 Microstructure and phase identification

Samples were observed by SEM with special attention to microstructural variations. In a five-track coating (with 33% track overlapping), the first track had a different microstructure from the rest of the tracks as shown in Figure 5.6. The boride and carbide precipitates are visible as dark phases in the BSE images. In comparison to microstructure of Colmonoy 69 coatings, no significant refinement in precipitates could be observed. Instead, morphology of the borides was changed from blocky to elongated and needle-shape. Type of the phases will be identified later.

A sharp microstructural transition was present between the first and the second tracks (Figure 5.7(a)) because of the higher dilution, i.e. higher Fe content of the first track. According to the EDS measurements, while Fe content in the first track was more than 20 wt.%, it dropped to 14 wt.% just across the microstructural boundary. The microstructural effects of dilution could also be found adjacent to the clad-substrate interface. Regardless of V content or cladding speed, there was a precipitate-free interfacial layer as visible in Figure 5.7(b) in all of the samples. EDS mapping confirmed that there was a direct relationship between the extent of this precipitate-free zone and the thickness of Fe-rich layer as shown in Figure 5.7(c). The Fe content in the precipitate-free layer was measured to be around 40 wt.%. Apart from dilution-related changes, microstructure of V-modified deposits (with the same vanadium content) was mostly homogenous and insensitive to variations in deposition rate or substrate temperature.

To assess the effects of vanadium addition on microstructure and phase formations and to answer the question of whether or not V-rich phases formed, coatings with 5 wt.% of V were studied in more detail by higher magnification SEM imaging and EDS elemental mapping. SEM observations revealed details of the microstructure which were not visible in the lower magnification image of Figure 5.6. It can be seen in Figure 5.8(a) that microstructure of coatings modified by 5 wt.% of V contained many rod-shape precipitates which were covered with semicircular bumps on the sides. The image of Figure 5.8(a) is a combination of SE and BSE detector signals. Figure 5.8(b) to (f) are the EDS maps for various elements taken from the area shown in Figure 5.8(a) and superimposed on the SE+BSE image. It can be seen that the bumpy structures are rich in V and C and hence are vanadium carbide. The rods are rich in Cr, B and contain some V. This means that the rods are chromium borides with some dissolved vanadium. The fine scale of these phases made reliable quantitative EDS measurements difficult. Hence, the rod-shape borides and the bumpy carbides were further analyzed by TEM.

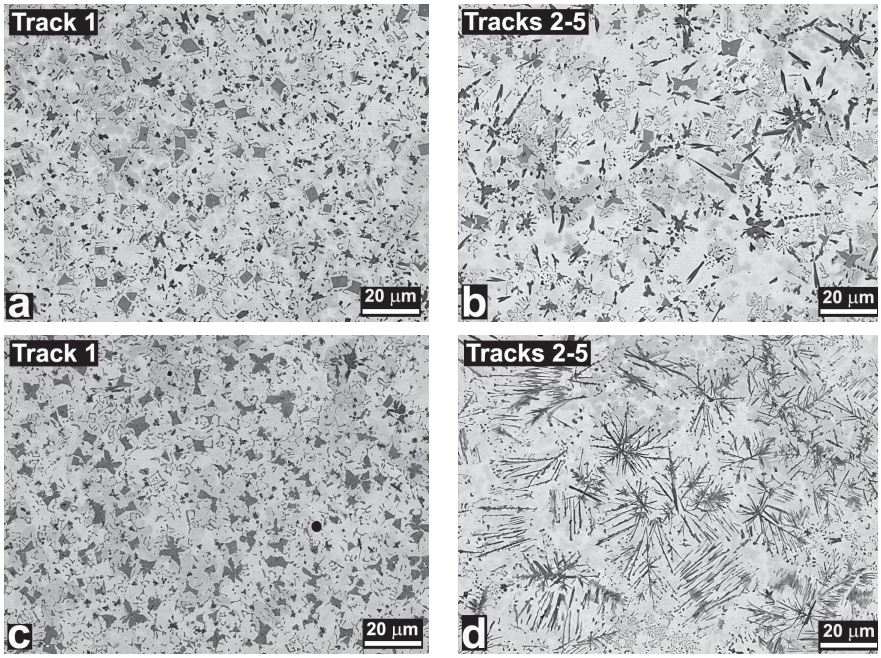

Figure 5.6. SEM-BSE images showing the microstructure of different tracks in the samples containing 2 wt.% V (a and b) and 5 wt.% V (c and d).

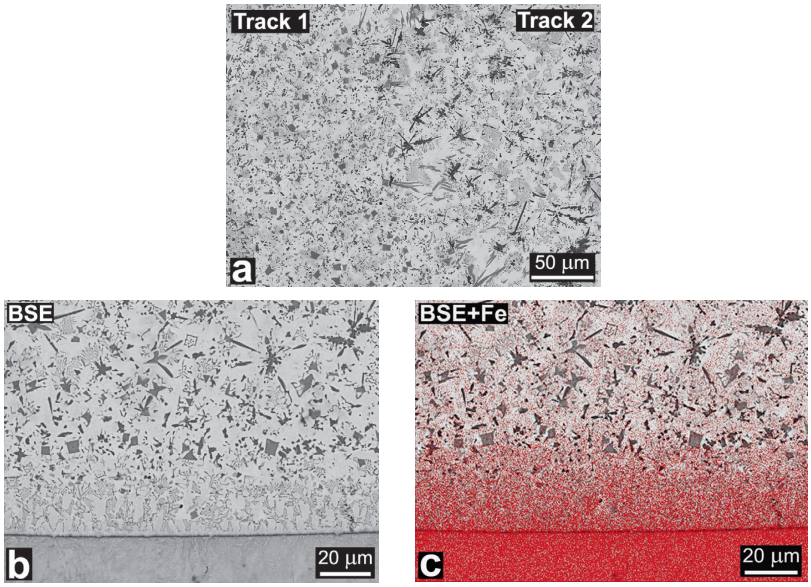

Figure 5.7. (a) and (b) SEM-BSE images showing the microstructural change from the first to the second track and the precipitate-free zone adjacent to the clad-substrate interface in the coatings containing 2 wt.% V. (c) EDS map of iron for the region shown in (b).

Figure 5.9(a) shows the typical microstructure of the rod-shape boride precipitates surrounded by bumpy carbides in the modified coatings as observed by TEM. There were many defects inside the rod, as shown in the enlarged micrograph of Figure 5.9(b). The white arrow in Figure 5.9(b) points out a newly grown rod or the end of another rod. The stacking faults are obvious in the image and can also be recognized from the streaks between the spots in the diffraction pattern of Figure 5.9(c) which was taken from the direction perpendicular to the rod. The diffraction pattern of Figure 5.9(c) is the combined electron diffraction patterns from both the rod and bump in Figure 5.9(a). Figure 5.9(d) is a close-up of the diffraction pattern in which the streak lines are more visible. TEM-EDS data shown in Table 5.4 confirmed that the bump was rich in V and C and the rod mostly consisted of Cr and B with some V. The ratio of Cr to V content of the rod-shape borides was close to 2:1. By combining the EDS data and the diffraction patterns obtained from several orientations by a series of specimen tilting, the rod and the bump could be identified as CrB and VC, respectively. It should be mentioned that the diffraction pattern from the rod could also be assigned as $(Cr_{0.5}V_{0.5})B$ phase (ICSD#613569) in the same axis as CrB in Figure 5.9(c).

The crystallographic orientation relationship (OR) between CrB and the VC can be deduced from Figure 5.9(c) as follows:

$$(010)[101]CrB \,//\, (100)[001]VC$$

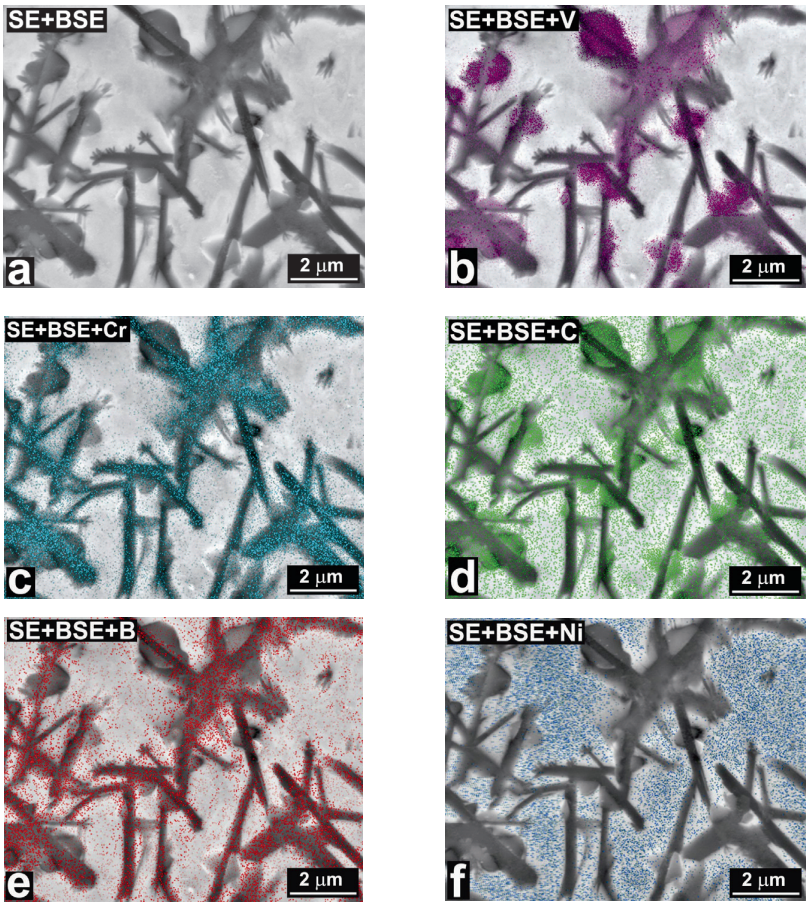

Figure 5.8. (a) High magnification SEM image showing the microstructural details of the deposits containing 5 wt.% V, (b) to (f) EDS maps for different elements in the area shown in (a).

Figure 5.10(a) presents a TEM bright field image showing the internal structure of a boride rod in more detail. The zig-zag contrast was visible inside the rod when the TEM specimen was tilted to some specific orientation during observation. Two distinct areas could be recognized inside the rod: the ones with stripes or banded structures marked as 'A', and the smooth areas labeled as 'B'. The diffraction pattern from area 'A' could be indexed as $(Cr_{0.5}V_{0.5})B$ and the one from area 'B' as CrB. Although the diffraction

pattern of $(Cr_{0.5}V_{0.5})B$ and CrB were very similar, the phases assigned to areas 'A' and 'B' had a smaller error. The EDS data showed that area 'A' contained more vanadium than area 'B' with a ratio of Cr:V close to 2:1. This means that while the area 'A' was a mixed Cr and V boride, its chemical formula was not exactly $(Cr_{0.5}V_{0.5})B$. Therefore, the areas 'B' and 'A' will be regarded as CrB and $(Cr_{1-x}V_x)B$. Figure 5.10(b) shows the diffraction pattern obtained from the whole rod in which components from both areas 'A' and 'B' are present. The bigger spots near the center of the diffraction pattern entirely overlap. But there is a very small shift between the diffraction spots farther away as indicated by the arrows in Figure 5.10(b) and shown more clearly in the magnified image of Figure 5.10(c). The small shift between diffraction spots is caused by minute differences between lattice parameters of CrB and $(Cr_{1-x}V_x)B$ (or with some approximation $(Cr_{0.5}V_{0.5})B$) as presented in Table 5.5. The two structures of areas 'A' and 'B' were also rotated over an angle of 0.8 ° around the axis parallel to the viewing direction, most probably in order to match their lattices and reduce the mismatch stress.

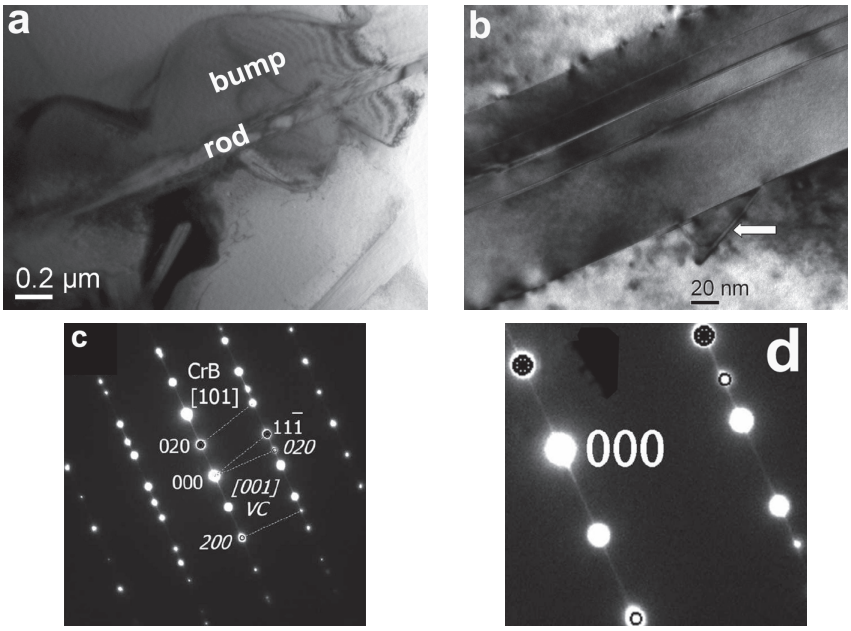

Figure 5.9. (a) TEM bright-field image showing the microstructure of deposits containing 5 wt.% of V, (b) magnified image of the rod, (c) combined electron diffractions of the rod-shape boride and the bumpy carbide, (d) a magnified section of (c) showing the streaks between diffraction spots more clearly.

Table 5.4. Composition of the phases labeled in Figure 5.9(a) (atomic %).

Phase	B	C	Si	V	Cr	Fe	Ni	Mo
bump	-	58.4	-	30	7	-	0.8	3.8
rod	35.3	0.8	0.8	15.6	35.7	1.9	2.2	7.8

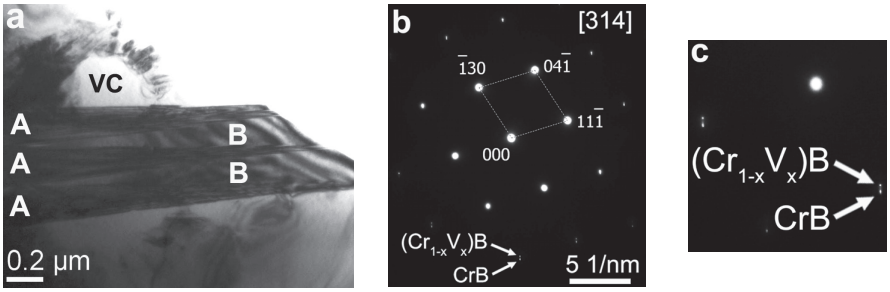

Figure 5.10. (a) TEM image revealing the internal structure of the boride rods in V-modified coatings. Areas labeled as 'A' and 'B' can be indexed as $(Cr_{1-x}V_x)B$ and CrB, respectively. (b) Diffraction pattern obtained from the whole rod with patterns from both areas 'A' and 'B'. (c) a magnified section of (b) in which slight difference of the diffraction patterns from areas 'A' and 'B' is visible.

Table 5.5. Crystallographic data of some carbides and borides of Cr and V.

Phase	System	Space group	Lattice parameter (nm)			XRD PDF#
			a	b	c	
CrB	Orthorhombic	Cmcm (63)	0.2978	0.7879	0.2935	89-3587
VB	Orthorhombic	Cmcm (63)	0.310	0.817	0.298	89-2308
$(Cr_{0.5}V_{0.5})B$	Orthorhombic	Cmcm (63)	0.302	0.800	0.296	613569 (ICSD)
Cr_7C_3	Orthorhombic	Pnma (62)	0.4526	0.7010	1.2142	89-7244
VC	Cubic	Fm-3m (225)	0.4165			73-0476

5.4.2.2 Hardness and cracking rate

The nature of cracks in the coatings deposited on cold or preheated substrates was different. V-modified coatings (as well as coating from Colmonoy 69) deposited on cold substrates massively fractured as shown in Figure 5.11(a) with interconnected zigzag cracks which propagated through the whole width of the deposits. As a result, calculating the cracking rate was somehow meaningless. Deposition on preheated bars reduced the number of cracks and changed their shape to regular transversal ones (Figure 5.11(b)).

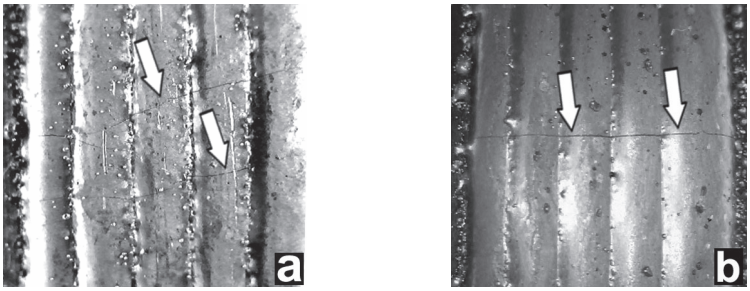

Figure 5.11. Transversal cracking in the coatings deposited on (a) cold substrates and (b) preheated substrates. Cracks are highlighted by arrows.

While it was not possible to obtain crack-free coatings from the original composition even after preheating the substrate to 500 ^{o}C, the V-modified coatings deposited on 500 ^{o}C preheated substrate were all crack-free. Figure 5.12(a) compares the cracking rate of V-modified coatings deposited on 200 ^{o}C preheated substrates with that of the coatings from Colmonoy 69 deposited on 500 ^{o}C preheated substrates. Addition of vanadium certainly reduced the cracking tendency of Colmonoy 69 coatings. The cracking rates were increased at higher deposition speeds and decreased with more V addition. The coatings modified with 5 wt.% V especially showed improvements in their cracking susceptibility. Figure 5.12(b) presents the hardness variations as a function of changes in the V content and level of dilution for the coatings deposited on 200 ^{o}C preheated substrates. Increasing the V content or dilution reduced hardness of the deposits. Lack of substantial hardness variations along the depth of the deposits is a sign of microstructural homogeneity. Hardness of the V-modified coatings was at the lower end of that of Colmonoy 69.

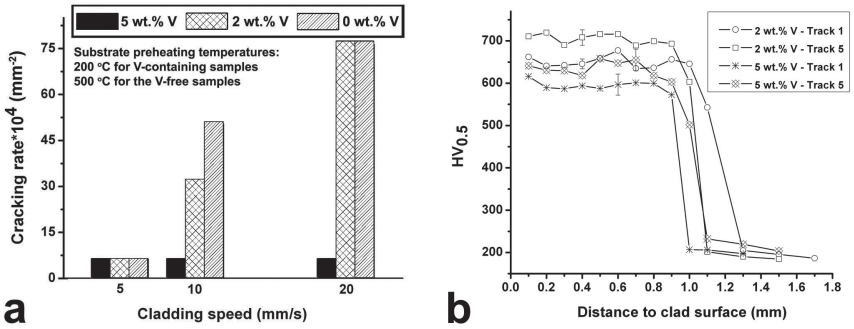

Figure 5.12. Effects of vanadium content on (a) cracking rate and (b) hardness of the deposits. In (b), an example of the error bars is shown for each graph.

5.4.3 Zr-modified coatings

5.4.3.1 Microstructures

Figure 5.13 shows the microstructure of samples containing 2 and 5 wt.% Zr. Lower contents of Zr mainly influenced the eutectic structure of the alloy. Upon additions of more Zr, new precipitates were formed which are visible with a bright contrast in the SEM image of Figure 5.13(b). Zr-rich precipitates are located at the edges of Cr borides, indicating that they were present as insoluble components and inactive particles for nucleation during solidification. No microstructural refinement was induced by Zr addition.

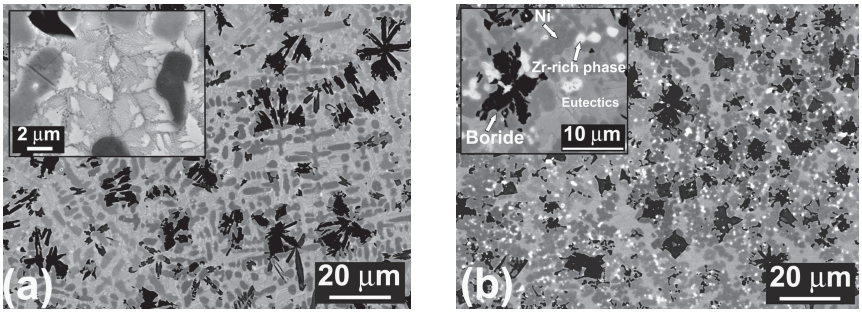

Figure 5.13. SEM-BSE images showing the microstructure of Zr-modified coatings containing (a) 2 wt.% and (b) 5 wt.% Zr. The insets show the microstructural details.

5.4.3.2 Phase identification

A combination of EDS and EBSD was used to evaluate mutual solubility of Zr- and Cr-rich phases and to identify their types. For EDS characterization of Zr-rich precipitates, a careful HPD has to be done because of the proximity of B-K (at 0.188 keV) and Zr-M (at 0.153 keV) characteristic X-ray lines[33]. The HPD profiles including B-K, Zr-M and both were generated and superimposed on the experimental EDS spectra. As shown in Figure 5.14(a), the HPD profiles confirmed that the lowest-energy peak of the spectra does not belong to B and fits much better to Zr-M. As a result, the lowest-energy EDS peak was assigned to Zr-M although Zr-L line was chosen for the quantification procedures. Afterwards, EDS spectra were obtained from the Zr- and Cr-rich precipitates shown in Figure 5.14(b) and quantified. The ratios of Cr:B and Zr:C atomic percentages in precipitates #1 and #2 were both close to unity. Hence, they were most probably of CrB and ZrC type, respectively.

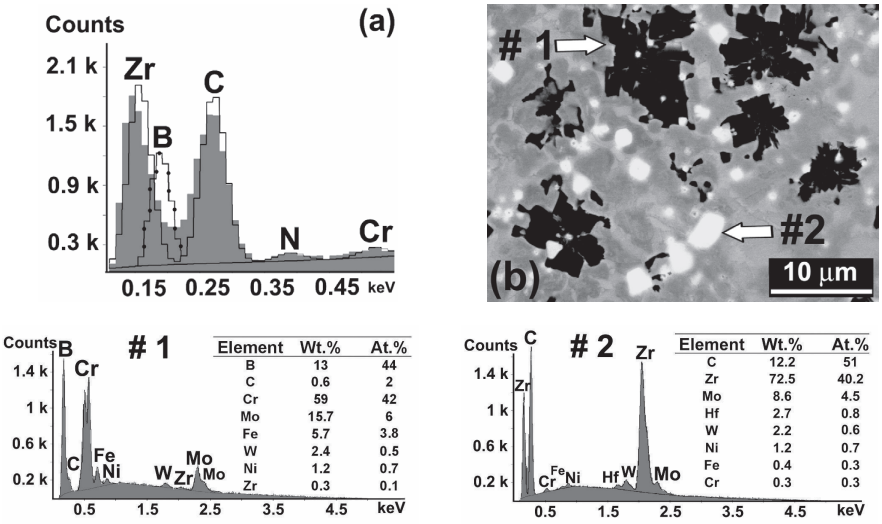

Figure 5.14. (a) The HPD profile including Zr M-line and B K-line, (b) EDS quantitative analysis of the precipitates labeled as #1 and #2 in the SEM image.

EBSD patterns were obtained and indexed by a list of candidate phases developed from the database of *International Center for Diffraction Data (ICDD)*. Both Zr carbides and borides were included in the list of candidate phases. Figure 5.15(a) shows the BSE image form the microstructure of Zr-modified deposits. EBSD pattern of the Zr carbide precipitates (bright particles) could be reproducibly and precisely (with a solution error of less than 0.5 ^{o}) indexed as ZrC as shown in Figure 5.15(b). The patterns from Cr-rich precipitates (the dark phase) could be indexed as CrB. Figure 5.15(c) shows the combination of phase and image quality maps taken from the area shown in Figure 5.15(a). Formation of ZrC precipitates on CrB and the Ni dendrite arms surrounding them are clearly visible.

The map of Figure 5.15(c) implies that the interdendritic areas consist of ZrC which is not true. The interdendritic areas contained Ni and Ni-Si-Zr eutectics (according to EDS analyses). The submicron scale of the layers in interdendritic eutectic structure means that EBSD patterns could come from more than one phase. This resulted in low quality patterns, which had a Ni component in most cases. Ni and ZrC are crystallographically very similar; both (Oh)[m3m] symmetry point group, lattice parameters: 0.4693 nm for ZrC (ICDD #350784) and 0.356 nm for Ni. Hence, their diffraction patterns could be misindexed as one another. In areas with a high quality EBSD pattern, i.e.

when the signal came from ZrC or Ni dendrites, it was possible to reliably distinguish them by limiting the number of indexed bands to 10. However, in eutectic areas, diffuse Ni patterns were misindexed as ZrC but with a lower image quality, i.e. darker shade in the image quality map.

Based on the EDS/EBSD results, the only Zr-rich precipitate in the Zr-modified deposits was ZrC and not Zr borides such as ZrB_2 as predicted by initial *Thermo-Calc*® simulations (Figure 5.4(a)). As a result, it was necessary to recalculate the solidification of Zr-modified alloy by excluding ZrB_2 from the list of possible phases. The recalculated phase fractions graph presented in Figure 5.15(d), precisely matches the experimental observations in terms of type and sequence of phase formation, i.e. absence of Cr_7C_3 and formation of ZrC at lower temperatures in comparison to CrB.

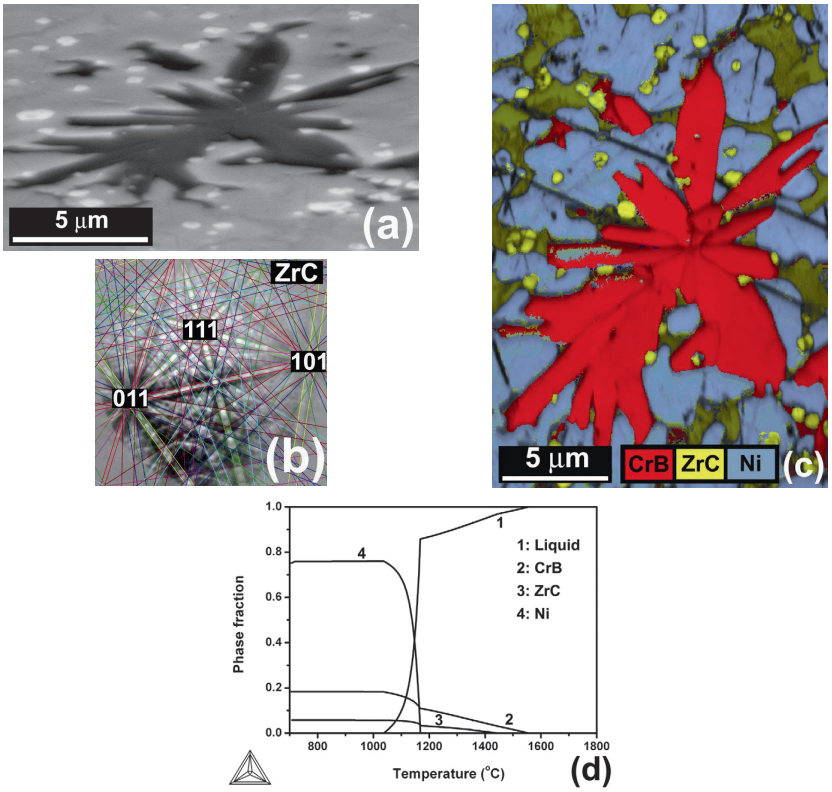

Figure 5.15. (a) SEM-BSE image (70 º tilted) of the microstructure of coatings containing 5 wt.% Zr, (b) EBSD pattern obtained from bright precipitates visible in (a) which can be indexed as ZrC. (c) The combined phase and image quality maps from the area in (a), (d) Re-calculated equilibrium phase fractions based on the phase identification results.

5.4.3.3 Hardness

Figure 5.16 shows the hardness of Colmonoy 69 deposits modified by 2 wt.% and 5 wt.% of Zr. In comparison to the hardness of Colmonoy 69 (CHAPTER 4), Zr-modified coatings had lower levels of hardness which was decreasing with higher additions of Zr. The possible mechanism of hardness variation by compositional modifications in this alloy system will be discussed later.

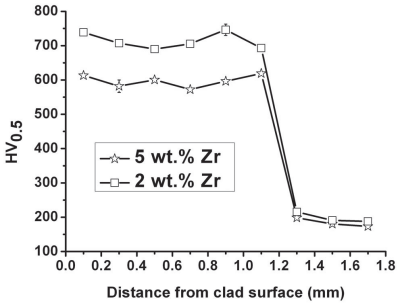

Figure 5.16. Hardness graphs for deposits modified by 2 wt.% or 5 wt.% Zr.

5.4.4 Nb-modified coatings

5.4.4.1 Microstructure

Figure 5.17 compares the microstructures of Colmonoy 69 coatings with that of the coatings modified by around 4 wt.% of Nb. It is clearly visible that addition of Nb significantly refined the microstructure. The mechanism of this refinement was providing the system with many Nb-rich nucleation agents on which the Cr borides were formed (Figure 5.17(c)). A true microstructural refinement only happened for specific amounts of Nb addition (in this case, around 4 wt.% Nb). Further additions of Nb coarsened the microstructure of the deposits (Figure 5.17(d)). Also, large quantities of eutectic phases appeared for higher Nb additions. Figure 5.18 shows that addition of Nb can also homogenize the microstructure to a large extent and remove the multiple microstructural changes observed for Colmonoy 69 (CHAPTER 4).

5.4.4.2 Phase identification

The same procedures as for Zr-modified deposits were followed to determine the type and to assess the mutual solubility of borides/carbides of Cr and Nb. The issues which had to be solved before proceeding with EDS or EBSD analyses were similar. For example, the X-ray M-line of Nb (at 0.171 keV)

was very close to the K-line for B (at 0.185 keV)[33]. Hence, a careful HPD was needed. The image of Figure 5.19 shows a colony of rods formed on a Nb-rich precipitate. Quantification of the EDS spectra proved that ratios of Nb:C in location #1 and that of Cr:B in location #2 were both close to unity. Hence, precipitates #1 and #2 were expected to be NbC and CrB.

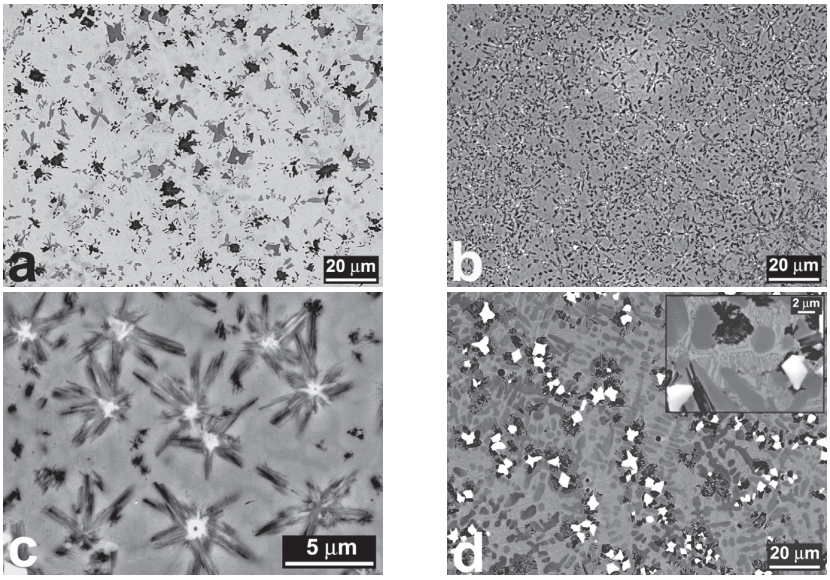

Figure 5.17. Microstructures of (a) Colmonoy 69 and (b) Colmonoy 69 plus 4 wt.% Nb. In (c), details of the refined microstructure in (b) are shown. In (d) coarse microstructure of the deposits with 9 wt.% of Nb is presented.

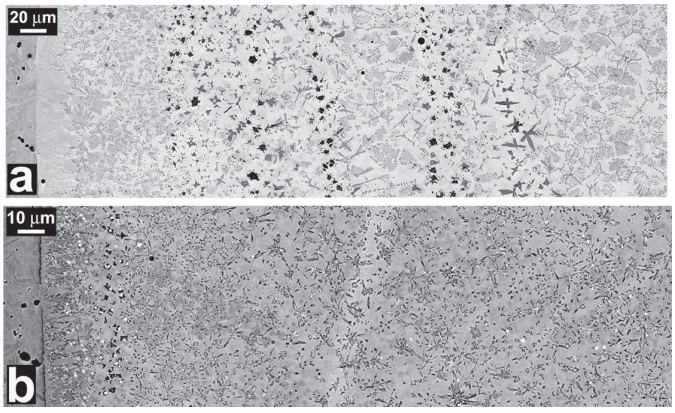

Figure 5.18. (a) Heterogeneous microstructure along the depth of a Colmonoy 69 coating, (b) homogenous microstructure of coatings modified by 4 wt.% Nb (both image are SEM-BSE).

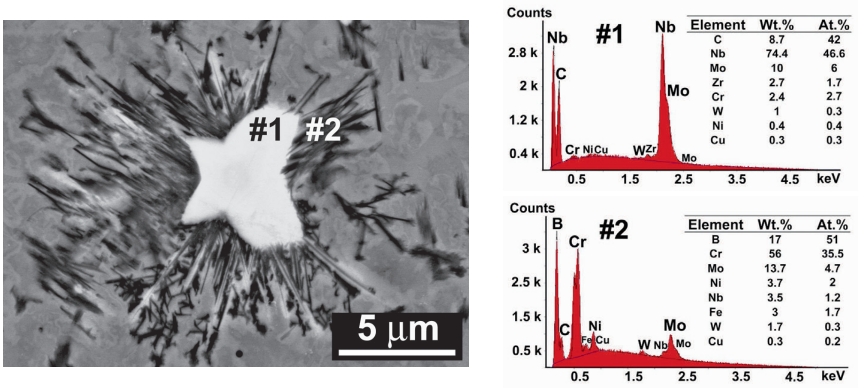

Figure 5.19. EDS quantitative analysis of Nb- and Cr-rich precipitates labeled as #1 and #2 respectively in the SEM-BSE image.

With the same considerations as in section 5.4.3.2 , EBSD patterns from Nb carbide precipitate were indexed as NbC (Figure 5.20(b)). Phase constitution was determined by EBSD scanning as shown in the phase map of Figure 5.20(c). The interdendritic regions of the Nb-modified deposits were usually indexed as NbC in the EBSD phase maps, which was an artifact caused by fine Ni layers in the eutectic areas and the crystallographic similarity of Ni and NbC (Cubic crystals, (Oh)[m3m] symmetry point groups, lattice parameters of 0.356 nm for Ni and 0.447 nm for NbC).

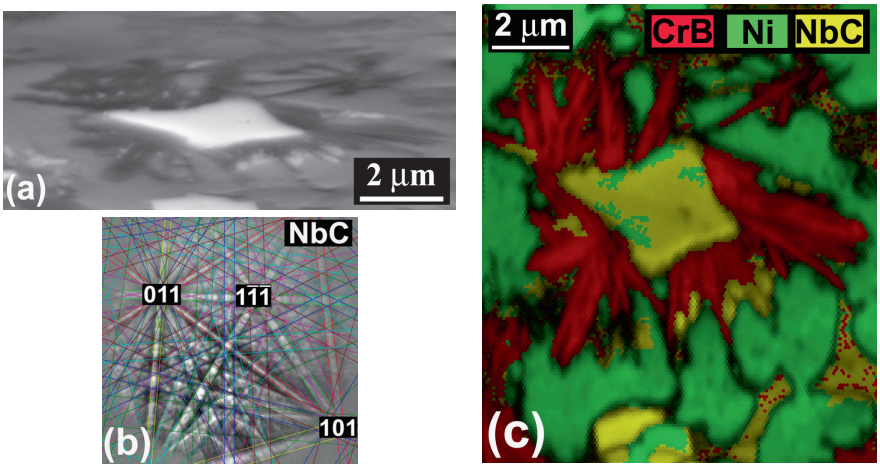

Figure 5.20. (a) SEM-BSE image (70 º tilted) of the microstructure of Nb-modified coatings, (b) EBSD pattern obtained from bright carbide precipitate in (a) which can be indexed as NbC. (c) The phase map (combined with image quality map) showing the type of constituent phases in the area in (a).

5.4.4.3 Hardness and cracking rate

Ni-Cr-B-Si-C alloys are developed for wear applications. Consequently, refinement of their microstructure should be ideally done without deteriorating their high hardness. It can be seen in Figure 5.21(a) that this goal was largely reached by addition of Nb as the microstructural refinement shown in Figure 5.17 was obtained at almost the same level of hardness as that of the original composition.

An interesting feature of the hardness graph in Figure 5.21(a) is that the deposits with different Nb additions have almost the same hardness. This may seem strange because Nb added NbC to the microstructure which has a hardness of around 2000 HV[34]. So, hardness of the coatings should normally increase for higher Nb additions. Nevertheless, the important contribution of the eutectic structure to overall hardness of Ni-Cr-B-Si-C alloys should not be ignored. The eutectic structure of Ni-Cr-B-Si-C alloys with the ratio of Si/B less than 3 mostly consists of hard Ni-Ni_3B eutectics (CHAPTER 4). Addition of Nb not only produced hard NbC precipitates, but also modified the eutectics. EDS maps showed that the interdendritic eutectics of Nb-modified coatings were rich in Ni and Si and contained some Nb. Hardness of the eutectic areas in Nb-modified coatings measured by single Vickers indentations using a force of 0.1 N ($HV_{0.1}$) was in the range of 800-900 HV. This means that a possible increase in hardness because of additional NbC could be compensated by a reduction in hardness of the eutectics phases. Hence, the overall hardness remained mostly unchanged. In the previous compositional modifications of Ni-Cr-B-Si-C alloys, both increase (with Ta[18] addition) and decrease (with Ti[35] or V[19] additions) in the hardness of original alloys were reported. Reduction in hardness of V- and Zr-modified Colmonoy 69 deposits was also observed in the current work. These different reports can be explained by the way Ta, Ti, V, Zr or Nb influence the eutectic structure. Otherwise, all of these elements produce very hard carbide and boride precipitates which should normally increase the hardness.

As the hardness remained unchanged by Nb-addition, changes in cracking susceptibility of the samples with and without Nb can be attributed to their microstructures. Figure 5.21(b) shows the effect of Nb addition on cracking tendency of the samples deposited on 500 ^{o}C preheated bars. It can be seen that cracking susceptibility of the microstructurally-refined deposits, i.e. those with around 4 wt.% of Nb, was basically the same as that of Colmonoy 69 samples. Addition of more Nb even increased the cracking rate.

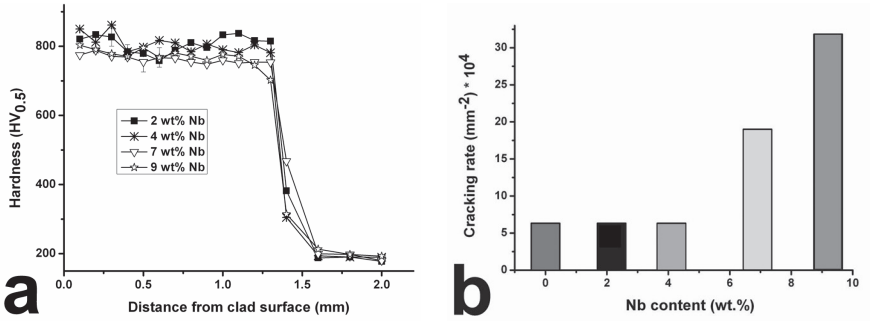

Figure 5.21. Variations of (a) hardness and (b) cracking rate as a function of Nb content. The colors and markers in (b) refer to the respective hardness curves in the graph of (a).

The cracking susceptibility of the deposits was evaluated by measuring the cracking rate of multi-track coatings, i.e. the number of transversal cracks per unit area of the deposits. It is well-known for laser-clad coatings that the cracking tendency of the coatings depends not only on the intrinsic properties of the coating material such as toughness of the alloy, but also on extrinsic properties of the deposit including thickness, area, defects (e.g. pores), deposition rate and temperature of the substrate among others[1]. Consequently, assessing the cracking tendency of the coating materials based on counting the number of cracks will be meaningful only under very similar extrinsic conditions and hence will have a very limited scope.

To overcome such a limitation, indentation by Vickers diamond pyramid indenter under known loads (higher than some threshold necessary to generate cracks) was tried to measure toughness[32]. If the material is relatively hard and brittle, cracks will be generated at four corners of the indents. The fracture toughness can then be measured using the following equation[32]:

$$K_{IC} = \left(\frac{1}{3\left(1-\upsilon^2\right)\sqrt{\pi}\sqrt[3]{\sqrt{2}\pi \tan\psi}} \right) \sqrt{H} \sqrt{\frac{P}{4a}} \qquad \textit{Eq. 5.3}$$

where υ is Poisson's ratio, ψ is the half-angle of Vickers indenter (68 degrees), H is the hardness, P the applied load and $4a$ the total linear crack length. This technique has been previously used to measure the fracture toughness of several metallic and composite materials such as W-Co[36], borided steel[37] and Plasma Transferred Arc (PTA) welded Fe-based hardfacing alloys[32].

The idea behind indentation test for our samples was to measure the toughness on a local scale, i.e. on a specific track. Such a local measurement

was needed because of variations in microstructure of Colmonoy 69 deposits as explained before. To perform the test, first the upper limit of the indentation load was found as described previously[32] to be around 1500 N and several indentations were made on tracks (at transversal cross-sections) with different microstructures using lower forces. Indentations made at a load of 125 N did not generate any corner cracks and those made at loads of 250 and 500 N contained very small corner cracks. However, massive and sudden cracks were generated at a load of 1000 N or higher for all microstructures. In the end, it was not possible to obtain a sufficient number of acceptable indents for a reliable measurement of fracture toughness. Most of the indents had to be rejected because of proximity to clad-substrate interface and clad surface or closeness to defects such as pores and cracks. Figure 5.22 shows an example of a rejected indent in which effects of the substrate and the diluted layer depicted as a plastic deformation crack-free zone around the lower part of the indent as well as the corner cracks reaching clad surface or being stopped by cracks produced during deposition are visible.

The conclusion is that much thicker deposits are needed for such measurements. In addition, indentations should be made on the top surface of the polished clad layers and not on their cross-section. Ultimately, the cracking rate was used to evaluate the cracking susceptibility of clad layers with similar extrinsic characteristics, i.e. constant size, geometry and type of the substrate, similar heating and cooling conditions, similar clad thickness and length and the same deposition rate.

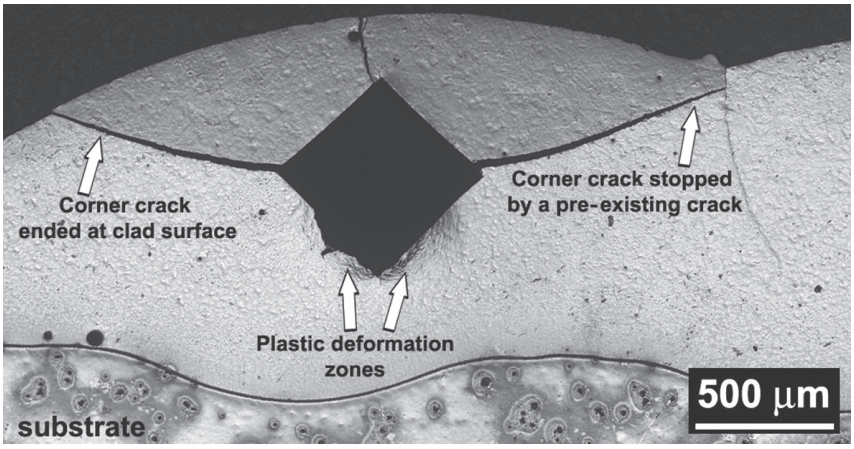

Figure 5.22. An example of indentations made on the transversal cross section of a Colmonoy 69 coating. This indentation has to be rejected because of the influence from ductile substrate, clad surface and the preexisting crack.

5.4.5 Analysis of the crack growth paths

The fact that cracking susceptibility of the microstructurally-refined deposits was generally the same as that of samples with much coarser microstructures shows that the initial analysis about the role of hard precipitates in cracking susceptibility of Ni-Cr-B-Si-C deposits may be inaccurate. As a result, the cracking phenomenon should be analyzed in more details.

The crack growth paths in Colmonoy 69 and Nb-modified Colmonoy 69 were re-examined by SEM and OM. SEM-BSE images of the crack propagation path (e.g. Figure 5.23(a)) suggested that the main contributors to crack growth in Ni-Cr-B-Si-C deposits are Cr-rich precipitates as also reported by other researchers[19]. This was in line with the previous observation of crack growth path from which the idea of refining the boride/carbide precipitates emerged. However, the role of the other constituent phases, i.e. eutectics and Ni dendrites could not be deduced from BSE images because these phases could not be properly distinguished by BSE imaging.

The fracture modes of Cr-rich precipitates, eutectics and Ni dendrites were assessed by observing the fracture surfaces of Colmonoy 69 deposits. To obtain the fracture surfaces, single tracks of Colmonoy 69 were deposited with zero dilution. Some of the tracks were detached and fractured during deposition. In Figure 5.23(b), the cleavage fracture of Cr_5B_3 and Cr_7C_3 precipitates and the ductile fracture of Ni with clear neck formation are noticeable. Type of the constituent phases was recognized based on their morphologies as characterized previously in CHAPTER 4. Figure 5.23(c) shows an area of the fracture surface consisting of Ni grains and interdendritic eutectic network. While the ductile behavior of Ni grains and their considerable plasticity are depicted by multiple necking, the eutectic network did not show much plasticity and fractured in a quasi-cleavage mode. These observations suggest that the eutectic structure in Colmonoy 69 deposits should have contributed to crack growth and clearly Ni was the only ductile component of the system.

Observation of the crack propagation path using OM revealed other details. Figure 5.24(a) shows the OM image of crack growth in the same area as in Figure 5.23(a). While the BSE image could not explain the twisting crack path, the OM image in Figure 5.24(a) clearly shows how cracks propagate not only in the Cr-rich precipitates, but also through the eutectic network (visible as a brown matrix). In addition, the OM image of Figure 5.24(a) reveals the role of Ni dendrites (bright areas) in deflecting the cracks

and forcing them to bridge. As OM proved to be more capable of revealing the true nature of crack propagation, crack growth path in the refined microstructure of Nb-modified deposits was observed using OM as shown in Figure 5.24(b). The Cr borides in the microstructure shown in Figure 5.24(b) are much smaller and are not anymore a major contributor to crack propagation. However, similar to Colmonoy 69 deposits, the continuous network of eutectic phases still provided the easy route for cracks to propagate. These observations confirm the pivotal role of the network of hard eutectics in cracking of Ni-Cr-B-Si-C deposits.

Microstructure of the coatings with different amount of Nb was re-examined by OM as optical microscopy proved to be a useful tool for microstructural analysis of these alloys, especially to study the crack growth paths as shown above. Figure 5.25 presents the OM microstructural images of deposits with 4 and 9 wt.% of Nb. The differences between the scale of constituent phases and quantity of the interdendritic eutectic are obvious. In comparison to SEM micrographs (both SE and BSE), OM images give a better overview of the microstructure in these alloys and are especially helpful to observe their eutectic structure.

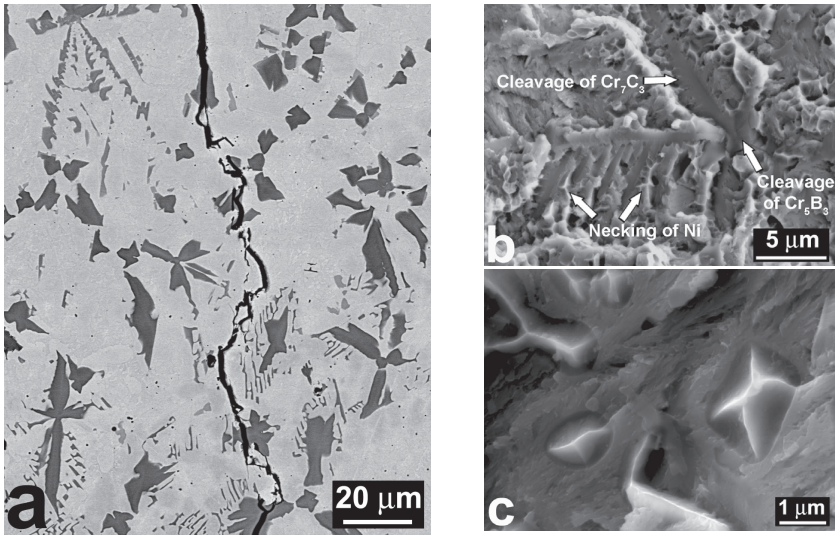

Figure 5.23. (a) SEM-BSE image showing an example of crack growth path in Colmonoy 69 coatings. The cracks apparently follow the precipitates (dark phases). (b) Fracture surface of Colmonoy 69 coatings showing different fracture modes for Ni and Cr-rich precipitates. (c) Fracture surface showing ductile failure of Ni in comparison to the quasi-cleavage fracture of the interdendritic eutectics.

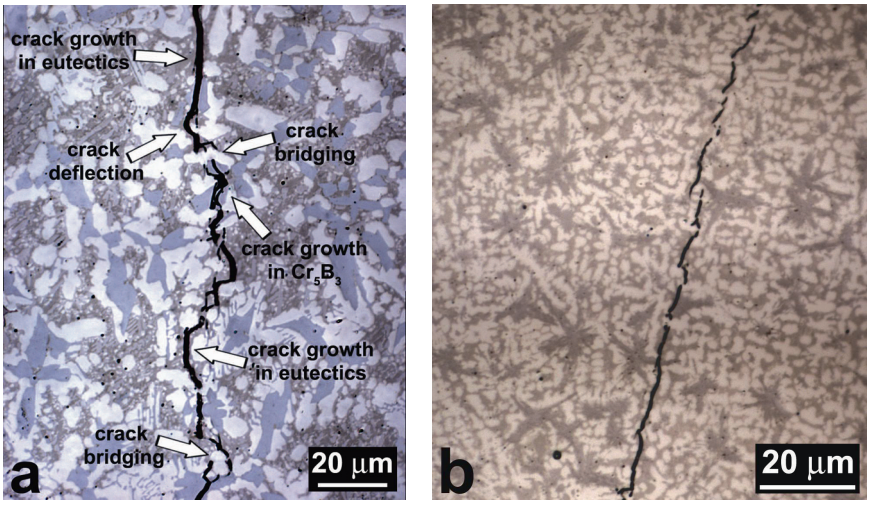

Figure 5.24. (a) OM image of the area shown in Figure 5.23(a) in which more details about the crack growth path are visible as indicated by arrows, (b) crack growth in the refined microstructure of Nb-modified deposits.

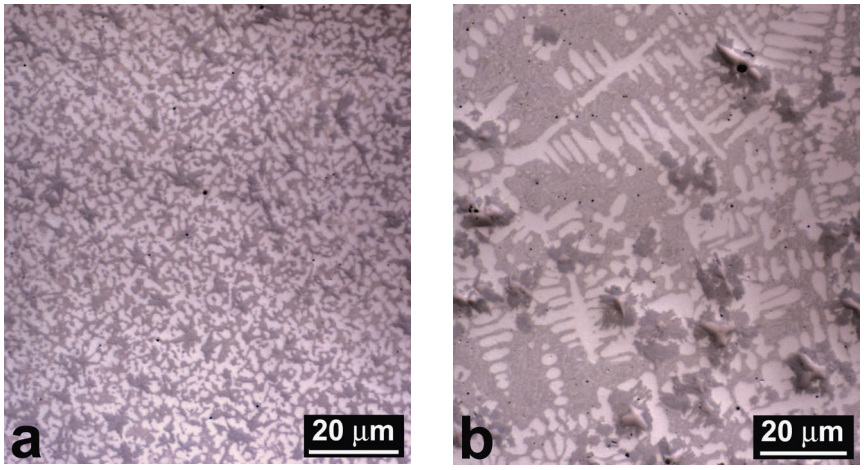

Figure 5.25. OM microstructural images from coatings modified by (a) 4 wt.% and (b) 9 wt.% of Nb.

5.5 Discussions

5.5.1 Microstructural evolutions

It was shown that the proposed procedure to select refining elements based on their ability to form precipitates at high temperatures which can remain as

independent phases and act as heterogeneous nucleation sites was able to refine the microstructure of Ni-Cr-B-Si-C alloys. The set of proposed rules in section 5.2.3.1 can be further analyzed based on the phase formation reactions and microstructural evolutions in V- , Zr- and Nb-modified deposits.

Addition of vanadium modified the morphology and nature of the boride phases and produced VC precipitates but did not refine the microstructure of Colmonoy 69 coatings. Consequently, the observed reduction in cracking susceptibility of V-modified coatings (Figure 5.12(a)) cannot be attributed to refinement of the hard precipitates as suggested by Wang et al.[19] because no significant microstructural refinement happened upon addition of vanadium. Instead, reduction in hardness may explain lower cracking tendencies. Furthermore, addition of vanadium reduced the sensitivity of Colmonoy 69 to fluctuations in the thermal conditions. Hence, microstructural variations were mostly eliminated.

The TEM and EDS findings can be used to explain the phase formation behavior of V-modified coatings and to answer the question of why the expected refinement did not occur upon V addition. Cr and V borides and carbide such as CrB, VB, Cr_7C_3 or VC all have negative values of ΔG_f which gives them the possibility of spontaneous formation during solidification and in fact all of them were present in the microstructure. However, their final characters were not the same. In other word, while VC existed as an independent phase, this was not the case for VB which went formed a solid solution with CrB and created precipitates consisting of layers of CrB and CrB-VB solid solution. This means that the final phase constitution of the system was affected by factors other than the thermodynamic possibility of spontaneous phase formation.

The structure of the rod-shape borides with alternating layers of CrB and $(Cr_{1-x}V_x)B$ can be explained based on the Cr-V-B ternary phase diagram. In Cr-V-B ternary system[27], a continuous solid solution forms between CrB and VB as a result of their identical crystal structures and very similar lattice parameters as presented in Table 5.5. In other words, although VB precipitated from the melt as an independent phase, ultimately it did not remain independent because of its tendency to form a continuous solid solution with the much more abundant CrB.

The interaction of borides in this system shows the importance of mutual solubility in final phase constitution. The situation for carbides can be explained in a similar way. In that case, VC and Cr_7C_3 form spontaneously but do not dissolve in each other because of their different crystal structures. It is

difficult for the carbides of Group VI like Cr_7C_3 with their hexagonal or orthorhombic structure to accommodate the cubic structure of Group V or IV carbide such as VC in solid solution[15]. This means that the independent existence of VC and Cr_7C_3 is in fact because of their limited mutual solubility.

Although VB did not remain in the microstructure as an independent phase and so it could not act as an effective nucleant, the independent VC particles also failed to induce the microstructural refinement. The reason for this failure can be found in the precipitation sequence of VC and the borides. It can be seen in Figure 5.8(a) that the VC particles formed on the sides of the existing boride phases. This means that VC formed after the boride rods. Such a sequence prevented the independent V-rich phase to perform its intended function as a nucleation site for the main precipitates of the system, i.e. borides. Consequently, addition of vanadium was unable to refine the microstructure of the deposits.

The case of Zr-modified coatings once more showed that the sequence of phase formation reactions must be considered. This is particularly important for the refinement process because an obvious prerequisite for an in-situ formed nucleating agent is its high temperature of formation. The re-calculated solidification sequence of the alloy modified by 5 wt.% of Zr addition in Figure 5.15(d) shows that ZrC started to form more than 100 ^oC after CrB. By that stage, the nucleation of CrB would have been largely completed. As a result, ZrC particles could not act as nucleation sites and addition of Zr did not induce any microstructural refinement.

Addition of Nb in specific quantities was shown to induce a true microstructural refinement in Colmonoy 69 deposits without deteriorating its hardness. Nb fulfilled the requirements of forming a phase at high temperatures with little solubility in Cr-rich phases which could act as nucleation agents for them. NbC precipitates provided nucleation sites for CrB rods and this substantially refined the microstructure. In addition, microstructural sensitivity of the original composition to variations of solidification conditions subsided by addition of Nb. Hence, no considerable microstructural heterogeneities could be found in the Nb-modified coatings. From the above-mentioned perspectives, Nb can be regarded as a useful alloying addition for the high-alloy grades of Ni-Cr-B-Si-C.

According to the ΔG_f data[20], it was expected to form new borides upon addition of Zr or Nb to the original alloy but none were formed. It should be noted that the reported ΔG_f data are usually measured or

calculated for reactions in which pure elements react or a single chemical reaction occurs to form that compound[20]. Formation of the same compounds may not necessarily happen in a multi-component system as they may not contribute to bringing the free energy of the whole system to its minimum. From this point of view, application of the thermodynamic calculation softwares to consider competing reactions in the multi-component system can be very helpful. An example of this was shown for the Nb-modified alloy in which the type and sequence of phase formations were predicted by *Thermo-Calc*® simulations with a reasonable precision (Figure 5.4(b) & (d)).

Nevertheless, such simulations cannot account for the non-thermodynamic effects which can become dominant, especially in processes as laser deposition which include rapid solidification. While ZrB_2 plus Cr_7C_3 was the most thermodynamically-favorable set in the alloy modified by 5 wt.% of Zr (Figure 5.4(a) and (c)), in reality Zr and C content of the alloy precipitated as ZrC. Such a phase selection phenomena was most probably nucleation-controlled as no borides were detected in the microstructure or predicted by the re-calculated solidification path (Figure 5.15(d)).

In an alloy system with numerous phases, competition in the nucleation-controlled regime will be largely determined by the relative magnitudes of ΔG^*, i.e. the energy barrier to heterogeneous nucleation which can be represented as:

$$\Delta G^* = \frac{16\pi\gamma_{SL}^3 T_m^2 f(\theta)}{3L_f^2 \Delta T^2} \qquad \textit{Eq. 5.4}$$

where ΔT is undercooling of the liquid phase, γ_{SL} solid-liquid interface energy, T_m equilibrium melting point, L_f latent heat of phase formation and $f(\theta)$ nucleation potency factor of the heterogeneous site for the wetting angle θ. *Eq. 5.4* shows that ease of nucleation depends not only on the latent heat of phase formation (L_f or i.e. ΔG_f), but also on other parameters such as the solid-liquid interface energy and the suitable level of undercooling below equilibrium melting point. Selection of the refining element based only on ΔG_f as suggested before[19] neglects the fact that ΔG_f values of a compound mostly show stability of that phase and not its ease of formation.

Although the proposed methodology and the rules can explain a good deal about the selection of effective alloying elements for microstructural refinement of Ni-Cr-B-Si-C alloys, they need further elaboration on certain

areas. The first one is explaining the role of kinetic effects in the phase selection processes as briefly mentioned above. This will become pivotal when the additional element can participate in multiple precipitation reactions, especially in rapid solidification processes such as laser deposition. The second point is to understand the nucleation mechanism in Nb-modified alloys. In the current work, the nucleating capability of NbC was attributed to its high temperature of formation and its lack of solubility in CrB which gave it the chance to remain as an independent phase. However, such an argument neglects the fact that a good nucleating agent should fulfill more conditions than just being physically available at the right temperature. For example, the surface energy between heterogeneous nucleation site and solid crystal should be lower than the surface energy between heterogeneous nucleation site and the melt[31]. Such a condition is in turn controlled by factors including the lattice mismatch and orientation relationship between the nucleant and growing crystal and the chemical nature of the surface layer on the nucleant[38].

5.5.2 The microstructural refinement-cracking relationship

Nb addition and the subsequent refinement of hard Cr-rich precipitates did not fulfill the expectations for enhancement of the coatings' toughness. The outcome was not in line with the findings of a previous research on the correlation between structural scale of the strengthening components and fracture toughness of wear-resistant Fe-base alloys in which the authors hypothesized that "the reduction of the structural scale of the microstructure would enhance the fracture toughness"[39]. In [39], it was shown that microstructural refinement of Fe-base wear resistant alloy deposits could enhance their fracture toughness while preserving hardness of the deposits. In this way, the so-called "hardness-toughness paradox" can be solved by preserving the quantity of hard components but reducing their scale. Although a similar phenomenon, i.e. microstructural refinement while preserving the level of hardness, happened in Nb-modified Colmonoy 69 coatings, the outcome was not consistent with the above-mentioned hypothesis.

This discrepancy can be explained based on the different phase constitution and microstructure of laser-deposited Ni-Cr-B-Si-C coatings. If the microstructure consists of strengthening components in a continuous matrix of ductile phase as in [39], then refinement of the strengthening components may enhance the fracture toughness. This is so because the ductile phase may effectively isolate cracks in the hard components by

providing plastic zones ahead of the cracks. In laser-deposited Ni-Cr-B-Si-C alloys such as Colmonoy 69 or Nb-modified Colmonoy 69, although carbide and boride precipitates were engulfed by Ni dendrites, a continuous network of eutectic structure filled the spaces between Ni dendrite arms.

Analysis of the crack growth paths and fracture surfaces showed that besides Cr-rich precipitates, the eutectic network also played an important role in the cracking process. In fact, as it can be seen in Figure 5.24, cracks often propagated through the continuous network of eutectics. This happened because the eutectic structure in Ni-Cr-B-Si-C alloys with the ratio of Si/B less than 3 (Si/B for Colmonoy 69: 1.33) mostly consists of Ni-Ni_3B which is very hard and brittle. Figure 5.23(c) clearly shows the large difference in plasticity between the eutectic structure and the ductile Ni grains. Although the eutectic network also contains lamella of ductile Ni, these lamellae are too thin to have any significant effect on the toughness. The eutectic phases in the Nb-modified alloy were not as hard as those of Colmonoy 69. However, they still formed an interconnected network which actively contributed to crack propagation as shown in Figure 5.24(b).

In a comprehensive work on the fracture mechanism and toughening of PTA-deposited Ni-Cr-B-Si-C alloys, Cockeram[10] concluded that crack bridging mechanism, i.e. necking and plastic deformation of Ni dendrites can explain the fracture behavior of Ni-Cr-B-Si-C alloys. Figure 5.24(a) confirms that Ni dendrites effectively deflect the propagating cracks and force them to bridge frequently which is in line with the findings of Cockeram. Toughening of a brittle matrix by crack bridging (ΔK_{CB}) can be described as[10,40]:

$$\Delta K_{CB} = C.E_d[V_f(\sigma_o / E_d)a_o]^{0.5} \qquad \textit{Eq. 5.5}$$

where C is a material-related constant and E_d, V_f, σ_o and a_o are the elastic modulus, volume fraction, yield stress and radius of the ductile phase (Ni dendrites), respectively. Measurement of the fracture toughness values for PTA-welded Ni-Cr-B-Si-C samples showed that in *Eq. 5.5*, V_f and a_o are the main parameters affecting the amount of crack bridging in these alloys[10]. This means that increasing the toughness of Ni-Cr-B-Si-C alloys requires higher percentages and/or coarser Ni dendrites. The phase formation behavior of Ni-Cr-B-Si-C alloys happens in such a way that increasing the percentage of Ni dendrites will inevitably decrease the fraction of the Ni-B-Si eutectics and hence reduce the overall hardness of the deposits (CHAPTER 4). In addition, laser-deposited samples usually have very fine Ni dendrites as a

result of their rapid solidification. Consequently, enhancing the crack bridging phenomena to toughen Ni-Cr-B-Si-C laser-deposited coatings while preserving their high hardness will be inherently difficult. In the Ni-Cr-B-Si-C alloy system, a sole microstructural refinement of the precipitates cannot be a viable toughening mechanism because although the ductile phase may deflect the cracks propagating to and from the precipitates, it cannot prevent them from using the continuous eutectic network as an easy growth path. Consequently, an effective toughening of these alloys will not happen unless the eutectic network is changed in type or its continuity is disrupted.

5.6 Conclusions

In this chapter, a new idea of reducing the structural scale of Cr-rich precipitates in Ni-Cr-B-Si-C hardfacing alloys by producing in-situ formed nucleation agents via controlled addition of refining elements was explored. It was proposed that the refining element should be able to spontaneously produce precipitates at high temperatures with little solid solubility in their Cr-rich counterparts. Colmonoy 69 alloy modified by V, Zr or Nb additions was deposited and studied. While no microstructural refinement occurred in V- and Zr-modified deposits, Nb addition can significantly refine the scale of Cr borides while preserving the original level of hardness. The mechanism of microstructural refinement in Nb-modified alloys was nucleation of CrB rods on NbC precipitates. Contrary to the expectations, microstructural refinement did not decrease the cracking tendency of Nb-modified coatings because not only the hard precipitates, but also the continuous network of hard eutectics contributed to the cracking process. Hence, toughening of Ni-Cr-B-Si-C alloys could not be reached solely by refinement of the hard precipitates. It was suggested that modifying the type of constituent phases in the eutectic structure or disruption of their continuous network is also needed to obtain high hardness-high toughness Ni-base hardfacing alloys.

Acknowledgements

Dr. Jiancun Rao (former colleague at Materials Science Group, University of Groningen, currently associate professor at Harbin Institute of Technology, China) is gratefully thanked for the TEM analyses. Mr. Richard Huizinga (TU Delft) is acknowledged for performing the Thermo-calc simulations. Wall Colmonoy Ltd. (The UK) is appreciated for providing Colmonoy 69 and V-modified Colmonoy 69 powders.

References

1. Wang, F.; Mao, H.; Zhang, D.; Zhao, X.; Shen, Y. Online Study of Cracks During Laser Cladding Process Based on Acoustic Emission Technique and Finite Element Analysis. *Applied Surface Science* **2008**, *255*, 3267–3275.
2. Kannatey-Asibu, E. *Principles of Laser Materials Processing*; Wiley series on processing of engineering materials; Wiley: Hoboken, N.J, 2009.
3. Brückner, F.; Lepski, D.; Beyer, E. Modeling the Influence of Process Parameters and Additional Heat Sources on Residual Stresses in Laser Cladding. *Journal of Thermal Spray Technology* **2007**, *16*, 355–373.
4. Huang, Y.; Zeng, X. Investigation on Cracking Behavior of Ni-based Coating by Laser-induction Hybrid Cladding. *Applied Surface Science* **2010**, *256*, 5985–5992.
5. Withers, P. J.; Bhadeshia, H. K. D. H. Residual Stress. Part 2 – Nature and Origins. *Materials Science and Technology* **2001**, *17*, 366–375.
6. Jendrzejewski, R.; Śliwiński, G.; Krawczuk, M.; Ostachowicz, W. Temperature and Stress Fields Induced During Laser Cladding. *Computers & Structures* **2004**, *82*, 653–658.
7. Jendrzejewski, R.; Kreja, I.; Śliwiński, G. Temperature Distribution in Laser-clad Multi-layers. *Materials Science and Engineering: A* **2004**, *379*, 313–320.
8. Jendrzejewski, R.; Śliwiński, G.; Krawczuk, M.; Ostachowicz, W. Temperature and Stress During Laser Cladding of Double-layer Coatings. *Surface and Coatings Technology* **2006**, *201*, 3328–3334.
9. Callister, W. D. *Materials Science and Engineering: An Introduction*; 7th ed.; John Wiley & Sons: New York, 2007.
10. Cockeram, B. V. The Fracture Toughness and Toughening Mechanisms of Nickel-base Wear Materials. *Metallurgical and Materials Transactions A: Physical Metallurgy and Materials Science* **2002**, *33*, 33–56.
11. Wang, D.; Liang, E.; Chao, M.; Yuan, B. Investigation on the Microstructure and Cracking Susceptibility of Laser-clad V2O5 /NiCrBSiC Alloy Coatings. *Surface and Coatings Technology* **2008**, *202*, 1371–1378.
12. Yu, T.; Deng, Q.-L.; Zhang, W.; Dong, G.; Yang, J. Study on Cracking Mechanism of Laser Clad NiCrBSi Coating. *J. Shanghai Jiaotong Univ. (Sci.)* **2012**, *46*, 1043–1048.
13. Knott, J. F. *Fundamentals of Fracture Mechanics*; Butterworth: London, 1973.
14. Cottrell, A. *Chemical Bonding in Transition Metal Carbides*; Institute of Materials: London, 1995.
15. Pierson, H. O. *Handbook of Refractory Carbides and Nitrides: Properties, Characteristics, Processing, and Applications*; Noyes Publications: Park Ridge, N.J., 1996.
16. Culter, R. A. Engineering properties of borides. In *Engineered Materials Handbook*; 1991; Vol. 4: Ceramics and glasses, pp. 787–803.
17. Chao, M.-J.; Liang, E.-J. Effect of TiO2-doping on the Microstructure and the Wear Properties of Laser-clad Nickel-based Coatings. *Surface and Coatings Technology* **2004**, *179*, 265–271.
18. Yu, T.; Deng, Q.; Dong, G.; Yang, J. Effects of Ta on Microstructure and Microhardness of Ni Based Laser Clad Coating. *Applied Surface Science* **2011**, *257*, 5098–5103.

19. Wang, D. S.; Liang, E. J.; Chao, M. J.; Yuan, B. Investigation on the Microstructure and Cracking Susceptibility of Laser-clad V2O5 /NiCrBSiC Alloy Coatings. *Surface and Coatings Technology* **2008**, *202*, 1371–1378.
20. Barin, I. *Thermochemical Data of Pure Substances*; 3rd ed.; VCH: Weinheim, New York, 1995.
21. Mizutani, U. *Hume-Rothery Rules for Structurally Complex Alloy Phases*; CRC Press: Boca Raton, FL, 2011.
22. Darken, L. S.; Gurry, R. W. *Physical Chemistry of Metals*; McGraw-Hill: New York, 1953.
23. Chelikowsky, J. Solid Solubilities in Divalent Alloys. *Physical Review B* **1979**, *19*, 686–701.
24. Zhang, Y. M.; Yang, S.; Evans, J. R. G. Revisiting Hume-Rothery's Rules with Artificial Neural Networks. *Acta Materialia* **2008**, *56*, 1094–1105.
25. Fedorov, T. F.; Kuz'ma, Y. B. Phase Equilibria in the System Zirconium-chromium-carbon. *Soviet Powder Metallurgy and Metal Ceramics* **1965**, *4*, 234–237.
26. Fedorov, T. F.; Popova, N. M.; Gorshkova, L. V.; Skolozdra, R. V.; Kuz'ma, Y. B. Phase Equilibria in the Systems Vanadium-chromium-carbon, Niobium-chromium-carbon, and Tantalum-chromium-carbon. *Soviet Powder Metallurgy and Metal Ceramics* **1968**, *7*, 193–197.
27. Kuz'ma, Y. B.; Telegus, V. S.; Kovalyk, D. A. X-ray Diffraction Investigation of the Ternary Systems V-Cr-B, Nb-Cr-B, and Mo-Cr-B. *Soviet Powder Metallurgy and Metal Ceramics* **1969**, *8*, 403–410.
28. Hugosson, H. W.; Jansson, U.; Johansson, B.; Eriksson, O. Phase Stability Diagrams of Transition Metal Carbides, a Theoretical Study. *Chemical Physics Letters* **2001**, *333*, 444–450.
29. Chen, H. M.; Zheng, F.; Liu, H. S.; Liu, L. B.; Jin, Z. P. Thermodynamic Assessment of B–Zr and Si–Zr Binary Systems. *Journal of Alloys and Compounds* **2009**, *468*, 209–216.
30. Tang, Z.; Kramer, M. J.; Akinc, M. Evaluation of Phase Equilibria in the Nb-rich Portion of Nb–B System. *Intermetallics* **2008**, *16*, 255–261.
31. Dantzig, J. A.; Rappaz, M. *Solidification*; EPFL Press: Lausanne, 2009.
32. Meacham, B. E.; Marshall, M. C.; Branagan, D. J. Palmqvist Fracture Toughness of a New Wear-resistant Weld Alloy. *Metallurgical and Materials Transactions A* **2006**, *37*, 3617–3627.
33. Zschornack, G. *Handbook of X-ray Data*; Springer: New York, 2006.
34. Gilman, J. J. *Chemistry and Physics of Mechanical Hardness*; Wiley series on processing of engineering materials; Wiley: Hoboken, N.J, 2009.
35. Chao, M.-J.; Liang, E.-J. Effect of TiO2-doping on the Microstructure and the Wear Properties of Laser-clad Nickel-based Coatings. *Surface and Coatings Technology* **2004**, *179*, 265–271.
36. Spiegler, R.; Schmadder, S.; Sigl, L. Fracture Toughness Evaluation of WC-Co Alloys by Indentation Testing. *Journal of Hard Materials* **1990**, *1*, 147–158.
37. Campos, I.; Rosas, R.; Figueroa, U.; VillaVelázquez, C.; Meneses, A.; Guevara, A. Fracture Toughness Evaluation Using Palmqvist Crack Models on AISI 1045 Borided Steels. *Materials Science and Engineering: A* **2008**, *488*, 562–568.
38. Murty, B. S.; Kori, S. A.; Chakraborty, M. Grain Refinement of Aluminium and Its Alloys by Heterogeneous Nucleation and Alloying. *International Materials Reviews* **2002**, *47*, 3–29.

39. Branagan, D. J.; Marshall, M. C.; Meacham, B. E. High Toughness High Hardness Iron Based PTAW Weld Materials. *Materials Science and Engineering A* **2006**, *428*, 116–123.
40. Ashby, M. F.; Blunt, F. J.; Bannister, M. Flow Characteristics of Highly Constrained Metal Wires. *Acta Metallurgica* **1989**, *37*, 1847–1857.

Chapter 6

DEVELOPMENT OF Ni-BASE COATINGS FOR MARINE APPLICATIONS *

This chapter aims at developing functional Ni-base coatings to protect components in marine applications with specific interest in hydraulic piston rods for dredging industry. As high-alloy grades of Ni-Cr-B-Si-C such as Colmonoy 69 (and Nb-modified Colmonoy 69) were too susceptible to cracking, other Ni-base alloys with lower hardness and less cracking tendency are deposited by laser cladding. Microstructure and corrosion/erosion performance of several commercial as well as newly developed alloys are investigated. In comparison to commercial alloys, coatings deposited from the developed alloy showed a good combination of hardness and toughness and better corrosion/erosion resistance. An important and exciting outcome of this chapter is that development of alloys with a combination of high hardness and high toughness could not only make the deposition step easier (as discussed in CHAPTER 5), but it will also result in coatings with enhanced erosion resistance.

---

* This chapter appears in the following journal papers:

I. Hemmati, V. Ocelík, J.Th.M. De Hosson, Effects of the alloy composition on phase constitution and properties of laser deposited Ni-Cr-B-Si coatings, *Physics Procedia* 41 (2013) 302-311.

I. Hemmati, V. Ocelík, J.Th.M. De Hosson, Microstructure and properties of Ni-base coatings for marine applications, in preparation for submission to Applied Surface Science, 2013.

6.1 Introduction

As discussed in CHAPTER 5, obtaining crack-free coatings from high-alloys grades of Ni-Cr-B-Si-C (such as Colmonoy 69) was not possible even after preheating the substrate up to 500 ^{o}C and refining the microstructure of the coatings. In the case of protective coatings on hydraulic piston rods for marine applications, obtaining crack-free coatings is essential. Hence, to produce coatings which could be used in practice, it was necessary to either increase the substrate preheating temperature before deposition of hard Ni-Cr-B-Si-C alloys (e.g. Nb-modified Colmonoy 69) or to deposit Ni-base alloys with lower levels of hardness. In the end, the second route was followed in order to develop final coatings for functional testing.

In the experiments, both small samples (5 tracks, 10 mm) and clad layers more than 200 mm in length were deposited. The former were used for microstructural analysis and hardness measurements and the latter to perform corrosion and erosion tests. Firstly, deposition of 10-mm-long and 215-mm-long clad layers of Nb-modified Colmonoy 69 was done on carbon steel substrates preheated to 650 ^{o}C. While shorter coatings were crack-free, the longer ones still contained a few cracks propagating through the whole coating. The conclusion was that if it is not possible to deposit 215 mm of crack-free Nb-modified Colmonoy 69 on 50-mm-diameter steel substrates after preheating to 650 ^{o}C, it will definitely not be possible to attain crack-free coatings on real hydraulic piston rods with larger diameters and few meters of length. So, high-alloy grades of Ni-Cr-B-Si-C including Nb-modified Colmonoy 69 were excluded from the list of candidate materials to develop laser-deposited hydraulic piston rod coatings.

The idea behind choosing hard Ni-Cr-B-Si-C alloys was to produce laser-deposited coatings with hardness levels approaching that of the current ceramic coatings (CHAPTER 1). However, the outcomes of cladding experiments showed that the second route, i.e. deposition of softer Ni-base alloys should be tried as well. The required hardness for hydraulic piston rod coatings (according to our industrial partner) was a minimum of 400 HV. Hence, three new Ni-base alloys, namely Nucalloy 488V, Eatonite 5, Colmonoy 33 along with Inconel 625 were selected for the new round of experiments. Based on findings of previous chapters, a new type of Ni-base alloy system was developed with a very good combination of hardness and toughness as well as superior corrosion/erosion performance. This chapter concentrates on deposition, characterization and qualification of these new

coatings with the objective of developing functional coatings for hydraulic piston rods used in marine applications such as dredging industry.

6.2 Selection of coating materials

Table 6.1 shows the compositions of four selected alloy powders. The idea behind selection of each alloy will be explained here. As mentioned in CHAPTER 1, Inconel 625 coatings do not have enough wear resistance for dredging applications (according to our industrial partner). However, this alloy is being widely used in marine applications (mostly for corrosion protection) and was included in the new round of experiments as a reference material. Nucalloy 488V is a Ni-Cr-B-Si alloy with a high Si/B ratio. The role of Si/B ratio in microstructure and properties of these alloys was discussed in CHAPTERS 4 & 5. According to manufacturer's datasheet, Nucalloy 488V has a hardness of around 500 HV. It is expected that Nucalloy 488V coatings have higher toughness levels (in comparison to Colmonoy 69 coatings) because of their tougher eutectic structure and lower boride content. Colmonoy 33 is another Ni-Cr-B-Si alloy with a high Si/B ratio. The expected hardness of Colmonoy 33 coatings is around 400 HV. By comparing the microstructure and properties of Nucalloy 488V and Colmonoy 33 coatings with those of previous Ni-Cr-B-Si-C alloy deposits, it is possible to investigate the effects of alloy chemistry on microstructure/properties of this alloy system. Eatonite 5 was selected because of its similarity to the coating material used previously to produce laser-clad piston rod coatings (*Eatonite™ ABC-L1* developed by Eaton[1]) as stated in CHAPTER 1. The alloy used in *Eatonite™ ABC-L1* coatings is not disclosed. But based on its hardness, it should be similar to Eatonite 5.

In addition to these commercially-available alloy powders, a new type of Ni-base alloy was developed based on the ideas obtained so far on how to enhance the toughness of laser-clad Ni-base coatings. The novelty of this system is that it is strengthened primarily not by boride/carbide precipitates or Ni-B-Si eutectics, but by intermetallics. As the new alloy system is going through the patent application process, more details could not be disclosed. In this chapter, microstructure and properties of a representative alloy (code-named XL-1) from the new system will be discussed. The new alloy has a good combination of hardness and toughness. Furthermore, subsequent tests proved that coatings deposited from the developed alloy have better corrosion and erosion resistance in comparison to their commercial counterparts.

Table 6.1. Nominal composition of the commercial coating materials investigated in this chapter (numbers in weight percent, balance is Ni).

Alloy	Cr	Mo	Fe	Si	W	Co	Al	Ti	Nb+Ta	B	C
Inconel 625	21.5	9	5	-	-	1	0.4	0.4	3.65	-	0.1
Nucalloy 488V	20.5	-	7.5	6	2	-	-	-	-	1	0.3
Colmonoy 33	6	-	1.8	4.3	-	-	-	-	-	1	0.2
Eatonite 5	29	8.5	8	1.2	-	-	-	-	-	-	2

6.3 Experimental procedure

Two series of samples were produced from each of the above-mentioned alloys:

(i) Single-track and five-track deposits (33% track overlapping, 10 mm long) for microstructural characterization and hardness measurements.

(ii) 215-mm-long clad layers for corrosion and slurry erosion tests.

Samples were deposited on 50-mm-diameter S355 carbon steel rods at various cladding speeds (5, 10, 20 and 40 mm/s) using powder injection by side cladding nozzle and 800-1000 W of laser power. Powder feeding rate and laser power were adjusted to produce coatings with a thickness of 0.9 and 1.1 mm and dilution of less than 10 percent for all alloys and cladding speeds. To deposit the second series of Nucalloy 488V, XL-1 and Eatonite 5 samples, substrates were preheated up to 200 ^{o}C to prevent cracking.

Samples for microstructural characterizations and hardness measurements were prepared by standard mechanical grinding and polishing. Microstructure was analyzed using Optical Microscopy (OM) and Scanning Electron Microscopy (SEM). In addition, elemental distributions were analyzed using Energy Dispersive Spectroscopy (EDS). EDS maps were taken at voltages of 5 kV for boron and carbon and 20 kV for other elements. Microhardness was evaluated using Vickers indenter at a load of 4.9 N.

Test coupons for corrosion and erosion tests were machined from Inconel 625, Nucalloy 488V, Eatonite 5 and XL-1 coatings. Corrosion performance of the coatings was evaluated by Open Circuit Potential (OCP) and Electrochemical Impedance Spectroscopy (EIS) measurements using Ivium instruments at room temperature and three-electrode cell: working

electrode (laser-clad coatings), platinum counter electrode and KCl saturated Ag/AgCl reference electrode in artificial seawater (made according to ASTM D1141-90 standard). The electrochemical cell was made by attaching a tube to the surface of the laser-clad and machine bars using silicone sealant and connecting the electrodes (as shown in CHAPTER 2). The values of OCP and impedance were recorded after 1 day, 1 week, 2 weeks and 4 weeks.

To start corrosion tests, the cells were set at open circuit and the potential (OCP) was recorded before EIS measurements. After observing a relatively stable potential, an AC voltage with amplitude of 20 mV was applied at frequency of 10^5-10^{-2} Hz. The applied potential was small enough to have a pseudo-linear behavior in the electrochemical cell. The exposure area of each sample was 10 cm^2 and duplicate samples were evaluated for each coating material. The measurements were carried out in a Faraday cage to prevent disturbance from foreign electromagnetic fields. The EIS data were fitted with equivalent circuits using *Zview* software (*Scribner Associates Inc.*) The equivalent circuit consisted of different elements such as resistor (to represent the resistance that charge carriers encounter, e.g. the resistance of the coating or the charge transfer resistance of the corrosion reaction), capacitor (to represent charge accumulation quantified by capacitance, e.g. coating or double layer capacitance), and constant phase elements (CPEs, to represent non-ideal dielectric behavior). A Non-Linear Least Squares (NLLS) fitting procedure was used to optimize the parameters of the equivalent circuit components. Only as many elements were used as necessary to achieve an optimal fitting of the result. The hierarchy of elements in the equivalent circuit was derived based on the condition of a stable fitting of the result with minimum systematical deviation between measured and fitted data. After the corrosion tests, surface of the test samples were observed by SEM.

Slurry erosion test was done in the pot-type erosion test set-up (CHAPTER 2) using the parameters listed in Table 6.2. Two Cylindrical test coupons were machined from Inconel 625, Nucalloy 488V, Eatonite 5 and XL-1 coatings and tested along with C22 steel samples as the reference. The amount of eroded material was determined by weighing the specimens before and after the test (accuracy: 0.1 mg). The erosive wear rate (E) of the specimens was calculated as:

$$E = \frac{\Delta m}{\rho . A t} \qquad \textit{Eq. 6.1}$$

where Δm , ρ , A and t are mass loss, density of the specimen, specimen area and test duration. The mass losses of the two test coupons from each

coating material were averaged and compared with the average mass loss of the reference steel samples to evaluate the improvements in erosion resistance. Finally, surface of the eroded samples were observed by SEM to analyze the wear mechanisms.

Table 6.2. Testing conditions of the slurry erosion test.

Apparatus	Pot-type slurry-erosion test set-up (TNO Eindhoven, The Netherlands)	
Specimens	Buttons: 10 mm diameter & 6 mm thickness two C22 steel (harness: 150 HV) reference samples two samples with laser-clad layers	
Parameters	Angle of impact	40 ^{o}
	Slurry	20 vol.% abrasive 80 vol.% water
	Abrasive	Standard TNO sand mean particle size: 700 μm
	Slurry temperature	15-25 ^{o}C
	Relative speed of erodent particles	8 m/s
	Test duration	2 hours

6.4 Results

6.4.1 Microstructure and elemental distribution

Figure 6.1 presents the microstructure of Colmonoy 33 and Nucalloy 488V deposits as observed by OM. Cr-rich precipitates are mostly disappeared and the content of interdendritic eutectics is dramatically reduced. Contrary to Colmonoy 69, microstructures of Colmonoy 33 and Nucalloy 488V samples deposited at different cladding speeds were all similar indicating that these two alloys are not as sensitive to variations of cooling rate. Also, no substantial variations could be observed in size of the dendrite arms in Colmonoy 33 and Nucalloy 488V samples.

Details of the constituent phases could only be revealed by SEM. Figure 6.2 shows SEM Backscatter Electron (BSE) microstructural images of Colmonoy 33 and Nucalloy 488V deposits. Figure 6.2(b) shows that the interdendritic areas in Colmonoy 33 coatings contain at least three

components: the cellular structure, the layered eutectic and the dark spots. In the microstructure of Nucalloy 488V samples, there were rod-shape phases (Figure 6.2(c)) which were not visible in the OM image. These phases were surrounded or connected by another phase (Figure 6.2(d)) visible as a brown interdendritic structure in the OM image of Figure 6.1(b).

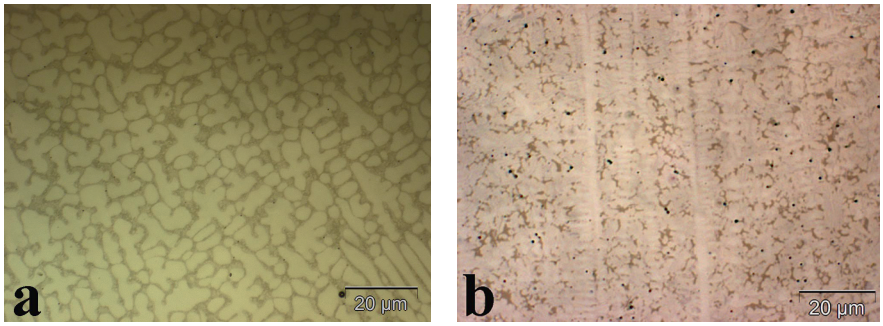

Figure 6.1. OM images showing the microstructure of (a) Colmonoy 33, and (b) Nucalloy 488V.

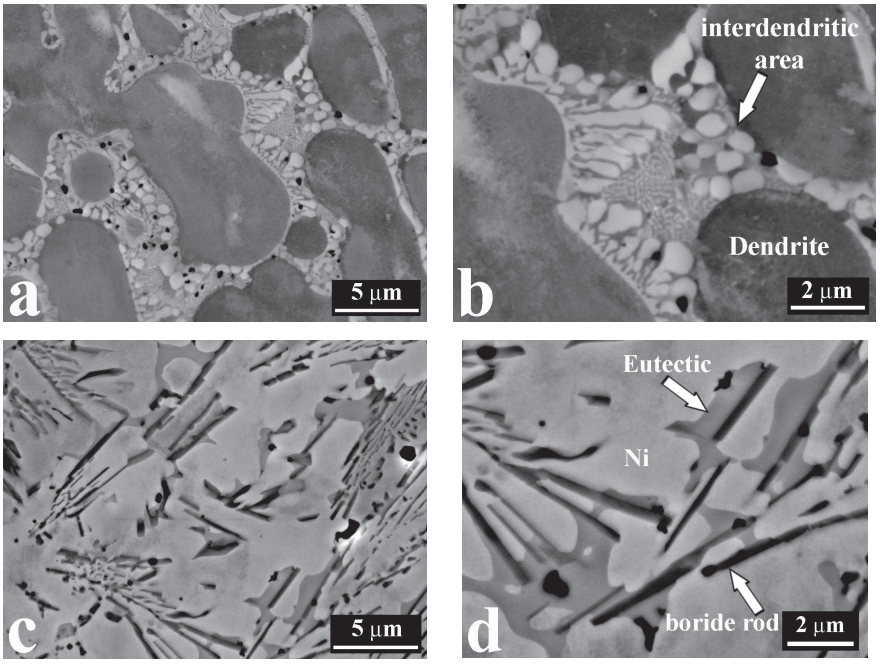

Figure 6.2. SEM-BSE images showing the microstructural details of Colmonoy 33 (a and b) and Nucalloy 488V (c and d) at different magnifications.Further details are highlighted by arrows.

EDS maps were obtained from several areas of Colmonoy 33 and Nucalloy 488V deposits to assess the distribution of different elements and to get an idea about possible type of the constituent phases visible in Figure 6.2. The EDS maps for microstructures shown in Figure 6.2(a) and Figure 6.2(d) are presented in Figure 6.3 and Figure 6.4, respectively. In Colmonoy 33, both dendrites and interdendritic phases were rich in Ni but segregation of Si and Cr in the interdendritic regions could be found. The interdendritic regions of Colmonoy 33 deposits contained Ni-Si eutectics and Cr-rich precipitates (most probably Cr borides). The resolution of EDS mapping was not high enough to accurately determine the composition of layers between the cellular phases and B or C in the dark Cr-rich precipitates. Nevertheless, the EDS maps show that a very limited amount of Cr-rich precipitates could still form in Colmonoy 33 samples.

In the case of Nucalloy 488V deposits, the rod-shape phases were rich in Cr and B and the phases covering and connecting them mostly consisted of Ni and Si. So, the microstructure of both Colmonoy 33 and Nucalloy 488V deposits consisted of Ni solid solution dendrites, Ni-Si eutectics and Cr-rich precipitates. The amount of Cr-rich precipitates is much higher in Nucalloy 488V deposits as a result of their higher Cr content.

Microstructure of Eatonite 5 coatings consisted of dendrites and interdendritic structure as shown in Figure 6.5. On the other hand, the microstructure of XL-1 coatings contained a very fine mixture of two different microstructures as represented in Figure 6.6. Identification of the constituent phases in XL-1 coatings using various techniques including Transmission Electron Microscopy and X-ray Diffraction showed that majority of the phase were intermetallic.

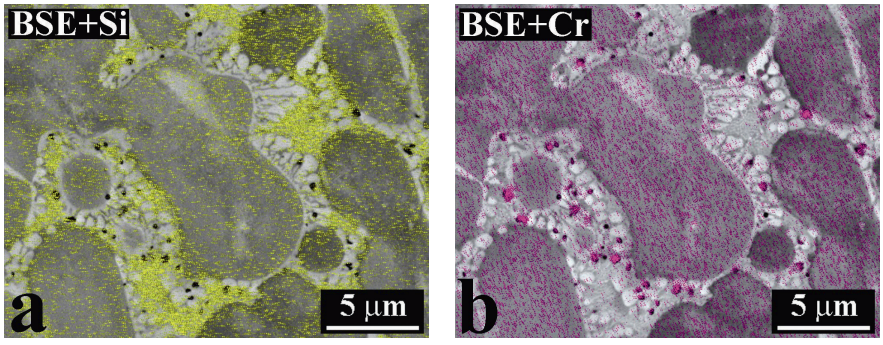

Figure 6.3. EDS maps for Si and Cr in the interdendritic region of Colmonoy 33 deposits shown in Figure 6.2(a). Ni was homogeneously distributed.

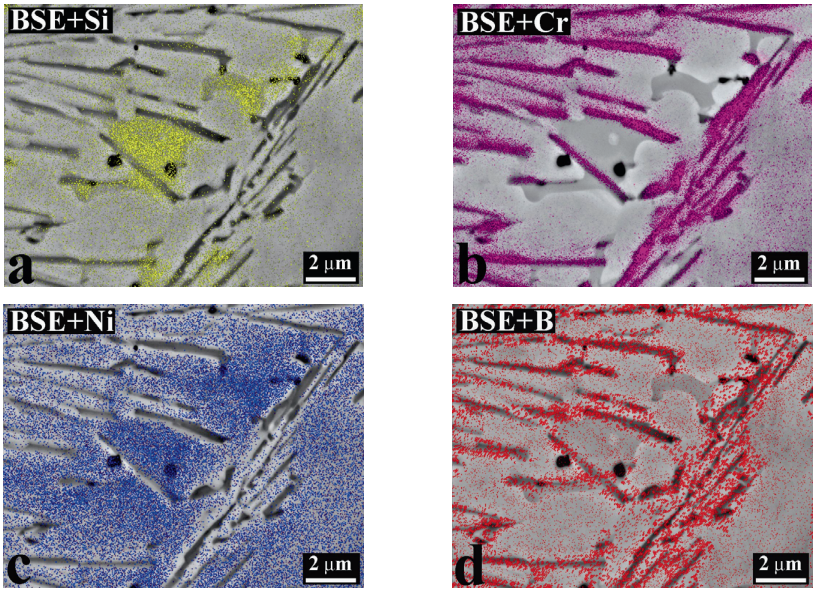

Figure 6.4. EDS maps showing the elemental distribution in the microstructure of Nucalloy 488V deposits presented in Figure 6.2(d).

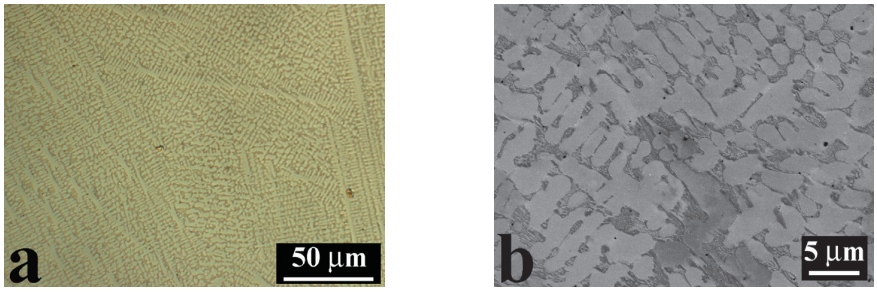

Figure 6.5. Microstructure of Eatonite 5 coatings observed by (a) OM. and (b) SEM.

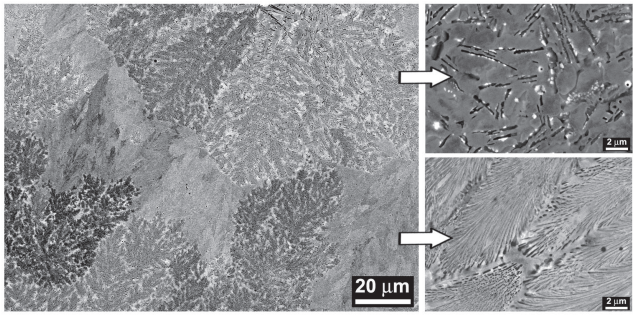

Figure 6.6. SEM-BSE image showing different microstructures of XL-1 coatings.

6.4.2 Hardness and cracking tendency

Figure 6.7 compares the hardness of coatings (with the same level of dilution) deposited from the Ni-base alloys studied in this chapter. It can be seen that Inconel 625 and XL-1 coatings has the lowest and highest hardness values, respectively. Although the hardness levels are less than those of Colmonoy 69 coatings (CHAPTER 4), all of the studied alloys (except for Inconel 625) fulfill the requirement of minimum hardness of 400 HV. In all cases, hardness of the deposits was decreased at higher dilutions. On the other hand, hardness was not affected by cladding speed. The only exception was Inconel 625 coatings which showed around 50 HV increase in hardness when cladding speed was increased from 5 to 40 mm/s.

In experiments of this chapter, the final goal was to obtain crack-free coatings for erosion/corrosion testing. Hence, preheating was used as needed and the cracking rates were not assessed in detail similar to what was done for Colmonoy 69 coatings. In 10-mm-long samples (5 tracks), it was possible to get crack-free coatings from all alloys and cladding speeds with the exception of Eatonite 5 coatings which started to crack from deposition speeds of 10 mm/s. For the 215-mm-long coatings, Inconel 625 and Colmonoy 33 coatings produced crack free coatings at all speeds. For the other alloys, substrates had to be preheated to around 200 ^{o}C to get crack-free coatings. XL-1 possessed the best combination of hardness and resistance to cracking.

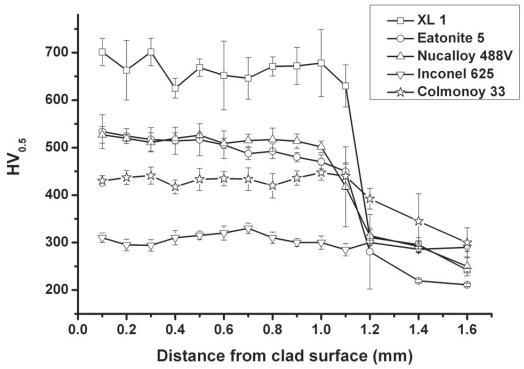

Figure 6.7. Hardness graphs for different alloys studied in this chapter.

6.4.3 Corrosion properties

Figure 6.8 shows the increasing trend of OCP values (vs. Ag/AgCl reference electrode) as a function of time. Within few days, the OCP values changed

from negative to positive in all cases. This increase of potential indicated that the surfaces gradually became passive after exposure to seawater. The OCP data shows that all of the coatings were dense and free from cracks and other defects which could provide paths for the electrolyte to reach the substrate. Otherwise, the OCP would have reached the corrosion potential of the substrate material within a short amount of time (e.g. 1 hour).

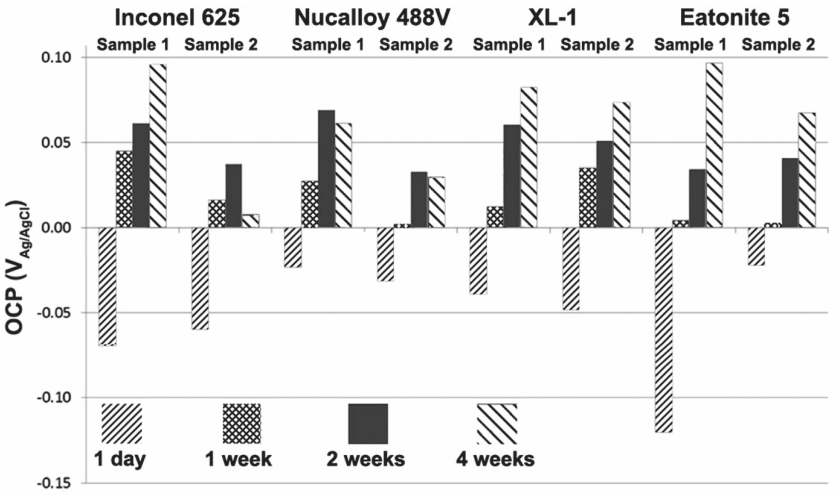

Figure 6.8. OCP values of the samples as a function of time.

Figure 6.9 shows the Bode impedance plots for the samples exposed to seawater for 1 day. The difference between impedance of various coatings is in the middle frequency range, which suggests that they have different capacitive behaviors. The impedance curves could be fitted with equivalent circuits shown in Figure 6.10. The data from Inconel 625, Nucalloy 488V and XL-1 samples could be fitted using circuit (a). On the other hand, the impedance data of the Eatonite 5 samples could only be fitted using circuit (b). In Figure 6.10, Rel, Qc, Rcp, Qdl and Wo are electrolyte resistance, constant phase element for the oxide layer, pore resistance, constant phase element for the double layer and Warburg element, respectively.

As it is usually the case, the equivalent circuits in Figure 6.10 contain the so called Constant Phase Element (CPE) which will be explained briefly. In reality, electrochemical systems have inhomogeneous properties. This can be caused by variations in roughness or reactivity of the electrodes and distributions of current, potential and reaction rates in the electrochemical cell. Under these conditions, ideal circuit elements may be inadequate to describe the electrical response. Therefore, usually impedance values of real

electrochemical systems cannot be well approximated by the impedance of an equivalent circuit involving only ordinary elements. It has been observed frequently that the use of electrical elements with distributed impedance (i.e. the CPEs) greatly aids the process of fitting experimental impedance data for a cell with distributed properties. The impedance of a CPE is defined as[2]:

$$Z = \frac{(i\omega)^{-n}}{Y_o} \qquad \text{Eq. 6.2}$$

where Z , i , ω , n and Y_o are, impedance (Ohm), imaginary number, angular frequency (rad/s), CPE factor and CPE constant, respectively. The CPE is quantified by the parameters Y_o and n . The relation of the CPE represents a wide variety of elements: for n = 1 an ideal capacitor is defined, for n = 0 the CPE represents an ideal resistor, for n = -1 the CPE is equivalent to an inductor and for n =0.5 a Warburg element is represented[2–4].

The data in Figure 6.9(a) and the equivalent circuits of Figure 6.10 suggest that after 1 day, the passive layer on Inconel 625, Nucalloy 488V and XL-1 coatings were denser than that of Eatonite 5 samples. This is in line with the OCP data in which the values for Eatonite 5 after 1 day of exposure to seawater were still negative. The same conclusion could be made from the phase data in Figure 6.9(b). The curve for XL1-sample 1 is very close to 90 degrees for a wide range of frequencies. This shows the mainly capacitive behavior of XL-1, i.e. lack of current or lack of electrochemical activity and hence very little or no corrosion. On the other hand, the phase shift angle for Eatonite 5 samples in the lower frequencies (the range representative for corrosion processes) is the least. This shows less capacitive nature and weaker passivation behavior of Eatonite 5. The equivalent circuit of Eatonite 5 coatings also shows that for this alloy, corrosion was controlled by diffusion (e.g. diffusion of oxygen through oxide layer).

After 4 weeks of exposure to seawater, the impedance at low frequency side increased for all samples and the capacitive behavior was more significant as depicted by an increase in the phase shift values for all samples (Figure 6.11). The impedance data for XL-1 and the other coatings could be fitted well using circuits (a) and (b) (in Figure 6.10), respectively. This means that the passive layer on XL-1 coatings was better than that on the other samples.

Observation of the surfaces after 4 weeks of exposure showed that the surface of Eatonite 5 samples were rougher than that of other samples (as

presented in Figure 6.12). This may have contributed to the poorer passivation behavior of Eatonite 5 because surface roughness decelerates the passivation process[2]. After laser cladding, all samples were machined using the same procedure. The rougher surface of Eatonite 5 samples was most probably caused by a higher volume of internal porosity created during the laser cladding process. Hence, deposition of coatings free from internal pores could contribute to corrosion resistance of the coatings.

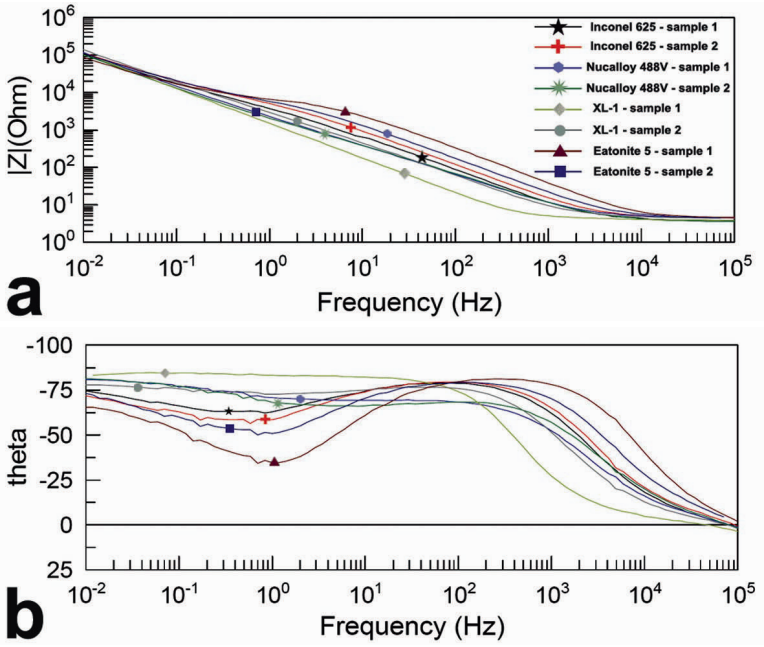

Figure 6.9. The Bode impedance plots of samples exposed to seawater for 1 day: (a) magnitude and (b) phase.

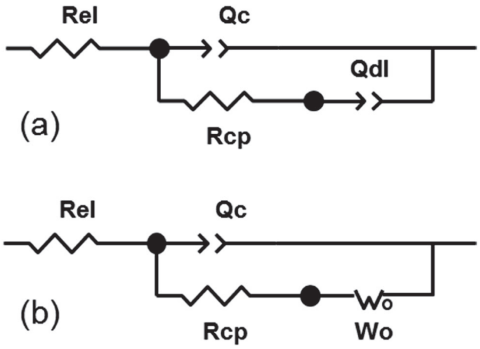

Figure 6.10. The equivalent circuits used to fit the impedance data.

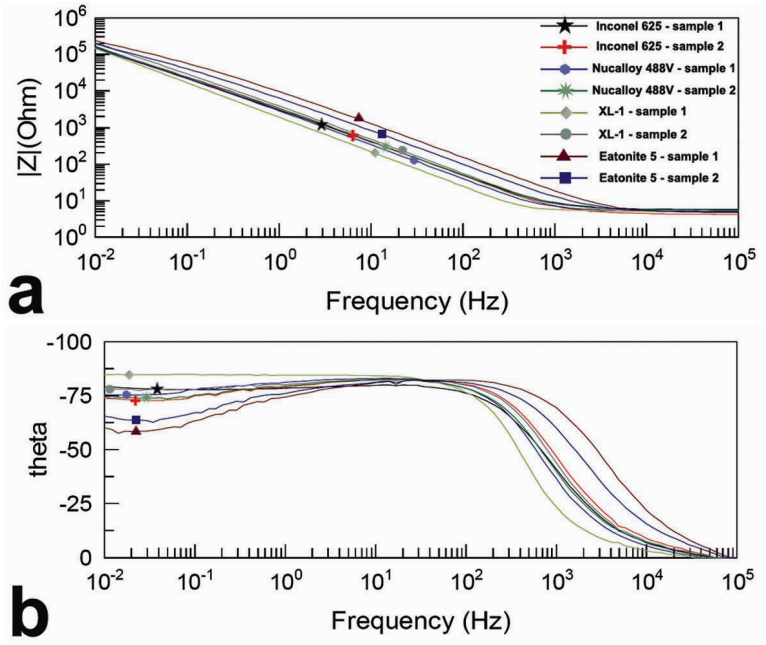

Figure 6.11. The Bode impedance plots of samples exposed to seawater for 4 weeks: (a) magnitude, and (b) phase.

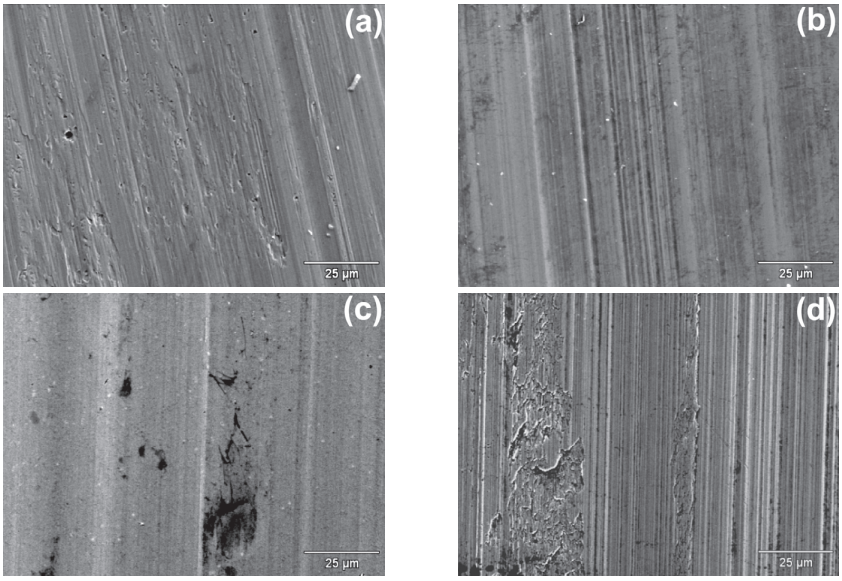

Figure 6.12. SEM images showing the surface of (a) Inconel 625, (b) Nucalloy 488V, (c) XL-1, and (d) Eatonite 5 after exposure to seawater for four weeks.

6.4.4 Erosion properties

While in some applications, the impact angle of the erosive material is largely constant (e.g. the flow of an erosive fluid in a pipeline), in other applications such as dredging, components are exposed to erodent particles hitting at varying impact angles. In that sense, the pot-type slurry erosion test rig in which the slurry mixture is agitated by the rotating sample holders can simulate the working conditions of such environments with a reasonable accuracy. Results of the previous researches showed that for most engineering materials (which consist of both hard and soft constituents), the maximum rate of erosion happens at intermediate angles of impingement[5,6]. Hence, an intermediate angle of impact (40 ^{o}) was chosen in the current work to expose the samples to the most severe erosion conditions.

Figure 6.13 shows the erosion rates and their relationship to hardness of the samples. Erosion rates of the samples were in the same range with XL-1 showing the lowest amount of wear. Hardness values are slightly less than those measured on smaller samples (presented in Figure 6.7). This could be caused by the higher dilution in larger samples or different hardness machine or the operator (measured in TNO Eindhoven). As can be seen in Figure 6.13(b), an increase of more than two times in hardness has just slightly decreased the erosion rate.

Figure 6.14(a) shows the improvements in erosion resistance in comparison to the reference steel. The value of erosion wear resistance provides a better estimate of erosion performance because it includes the slight variations in the test conditions (sand particle distribution, test temperature …). XL-1 showed a higher improvement in erosion resistance although the differences are again not significant. Interestingly, Inconel 625 was more effective in improving the erosion resistance in comparison to Eatonite 5 while the hardness of Eatonite 5 was two times higher (Figure 6.14(b)). In fact, hardness did not show a clear effect on erosion resistance of the coatings. This is in line with a previous report that increasing hardness in the range of 200-600 HV only marginally improved the erosion resistance[7].

Observation of the eroded surfaces by SEM showed that the most common erosion mechanisms were microcutting and plastic deformation as shown in Figure 6.15. These two erosion mechanisms were explained in details by Bitter[8]. In microcutting (Figure 6.15(a)), some material is removed by the particles scratching the surface. This also includes deformation, i.e. extruding of material to the sides of the crater. Depending on mechanical

properties of the material (e.g. work-hardening ability and toughness), these deformed platelets could be further deformed or fractured by the next impinging particles. The material could also be deformed by the erodent particles as shown in Figure 6.15(b). These different forms of damage happen when impinging particles hit the surface with their sharp corners or impact on their sides and roll over the surface for a short time.

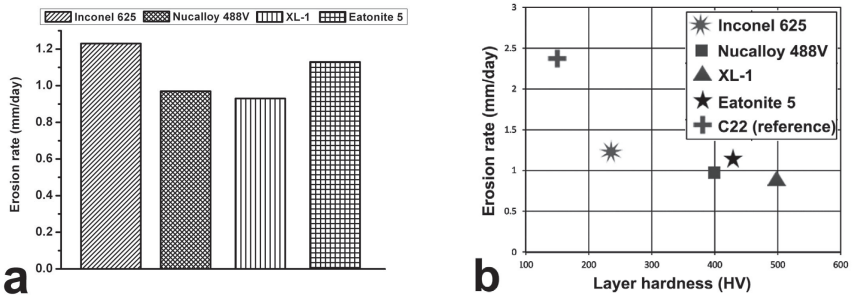

Figure 6.13. The mean slurry erosion rate of laser-clad coatings (a) and its relationship to hardness of the coatings (b).

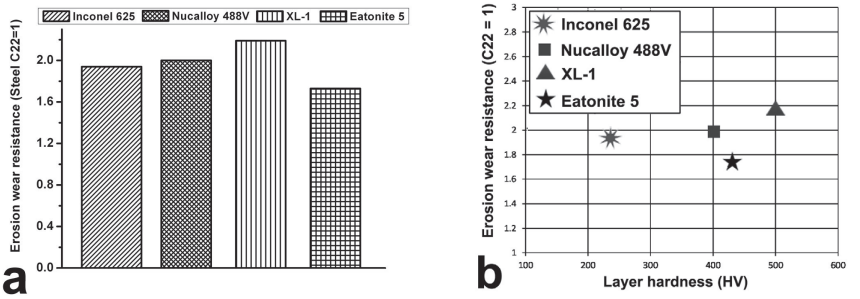

Figure 6.14. The mean slurry erosion resistance of laser-clad coatings (a) and its relationship to hardness of the coatings (b).

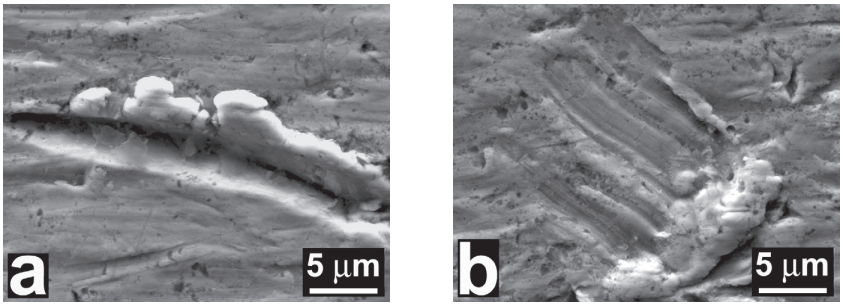

Figure 6.15. SEM images showing the features visible on the surface of eroded samples: (a) microcutting and (b) plastic deformation.

Figure 6.16 presents SEM images from the surface of eroded samples. The microcutting and plowing features along the impingement direction are visible. The extent of damage (i.e. number and depth of the craters and the amount of deformation) on the surface of Eatonite 5 is more than that for the other samples. On the other hand, the surface of Inconel 625 is more flat and contains much less craters. Inconel 625 had the lowest hardness among the studied coatings. Hence, it should have been the easiest to scratch by the erodent particles. However, it seems that the craters and platelets in Inconel 625 are forged (i.e. flattened) by the next impinging particles. Nucalloy 488V and XL-1 were somewhere in between the two above cases with XL-1 having a more flat surface containing smaller and shallower craters.

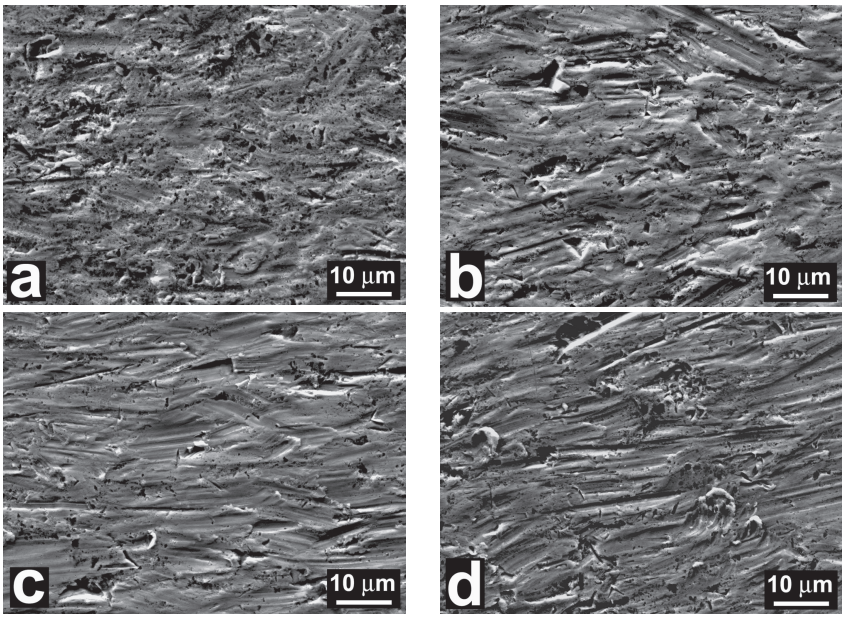

Figure 6.16. SEM images showing the eroded surfaces of (a) Inconel 625, (b) Nucalloy 488V, (c) XL-1, and (d) Eatonite 5.

6.5 Discussions

The following correlations could be established based on the results:

(i) The effects of alloy chemistry on microstructure and properties of Ni-Cr-B-Si-C alloys; and

(ii) The effects of microstructure/mechanical properties of the coatings on their corrosion/erosion performance.

In Ni-Cr-B-Si-C alloys, the Si/B ratio and the contents of Cr and B are the predominant compositional factors. Colmonoy 69, Colmonoy 33 and Nucalloy 488V present three examples across the compositional spectrum of this alloy family. Colmonoy 69 could be defined by a low Si/B ratio (~ 1.5) and a high quantity of both Cr and B. As discussed in CHAPTER 4, the microstructure of Colmonoy 69 contains many Cr-rich borides and carbides and a significant amount of interdendritic eutectic phases. These constituents form in three different stages starting with Cr-rich precipitates, then Ni solid solution dendrites and finally Ni-B-Si eutectics. Both quantity and nature of the eutectic phases have a substantial effect on hardness and toughness of laser-deposited Ni-Cr-B-Si coatings. For Si/B ratios of less than 3, the eutectic structure will mostly consist of Ni-Ni_3B (as shown in CHAPTER 4). When this ratio is increased to above 3, the primary eutectic reaction will change to Ni-Si type and Ni-Ni_3Si (which is less hard and brittle in comparison to the former case) becomes dominant[9]. This was confirmed by the EDS maps of Figure 6.3 and Figure 6.4 which showed that the interdendritic structures in Colmonoy 33 and Nucalloy 488V are rich in Si (and Ni).

If an increase in Si/B ratio is accompanied by a reduction in the Cr content as in Colmonoy 33, not only the nature of the eutectic phases changes, but also the Cr borides will be significantly diminished. According to the Ni-B and Ni-Si phase diagrams[10], B has a negligible solubility in Ni while Ni may dissolve up to 8.2 wt.% of Si. As a result, relatively high ratios of Si/B are needed to change the nature of the eutectic phases because a large part of the Si content will be dissolved in Ni dendrite. Insolubility of B in Ni also means that even at higher Si/B ratios (usually equivalent to low B contents), borides can still form if enough Cr is available. This is the case for Nucalloy 488V in which a high ratio of Si/B is combined with a high Cr content. The outcome is modification of the eutectic structures while keeping some of the Cr borides in the microstructure.

Colmonoy 69 and Colmonoy 33 are almost at the two compositional extremes of Ni-Cr-B-Si-C family with the former having a low Si/B ratio and high B and Cr contents and the opposite for the latter. These two extremes (and their similar alloys) could be called the “high-alloy” and “low-alloy” grades of the family, respectively. Hardness and toughness of these alloys are closely connected to their alloy content. In other words, the high-alloy grades are harder and more brittle than the low-alloy grades. In addition, the low-alloy grades are less sensitive to variations in thermal conditions during solidification. High cracking susceptibility is a major issue in laser cladding of

high-alloy grades of Ni-Cr-B-Si-C (CHAPTER 5). Despite considerable efforts made to solve this problem (in this work and in previous research), obtaining crack-free laser-deposited high-alloy Ni-Cr-B-Si-C coatings is still very difficult. As a result, these alloys are not very good candidates for production of laser deposited coatings over large areas such as the case for hydraulic piston rods.

The new alloy XL-1 was developed with the objective of producing high hardness and high-toughness Ni-base coatings by laser deposition or similar technologies. Testing of the functional properties proved that XL-1 coatings are superior to their commercial counterparts in terms of corrosion and erosion properties.

The OCP and EIS measurements showed that laser-clad coatings were free from cracks or open pores that could provide routes for electrolyte to reach the substrate. Absence of such routes is an important requirement for coatings intended for marine applications. If deposited properly, it is possible to obtain laser-clad coatings with no or very limited porosity (mostly at clad-substrate interface), very limited dilution and free from cracks. Hence, laser cladding is a promising technology to produce high-quality coatings for demanding applications.

The outcomes of the erosion test provided interesting insights into performance of the developed coatings. Generally speaking, the factors affecting erosion wear can be divided into three groups: properties of the target material (hardness, toughness, microstructure …), properties of the impinging particles (hardness, morphology, size) and test conditions (impact velocity, impingement angle…)[5]. The multitude of the controlling parameters in erosion process makes it difficult to establish a comprehensive model to explain the erosion behavior of different materials. In practice, most cases have to be evaluated individually using the experimental data for that specific case[11]. In the current work, the intended alloys were tested at constant conditions with the same type of the slurry. Hence, interpretation of the results could be done based on properties of the coating materials.

In erosion test, material removal occurs because of the cumulative effect of large numbers of particle impacts. Dissipation of the impact energy leads to either plastic damage accumulation and fracture (in ductile materials) or to progressive crack growth, fragmentation and removal of flakes (in brittle materials)[12]. In ductile materials, the impact energy is used for microcutting, i.e. formation of plowing-type craters (mostly at low impact angles) or

microforging and extrusion of protruding platelets (at high impact angles). The protruded material will be removed by the next impinging particles.

The outcomes of the erosion test showed that a higher hardness (at least in the range of 200-600 HV) will not necessarily result in better erosion resistance. For example, Inconel 625 showed a higher erosion resistance in comparison to the harder Eatonite 5. This means that erosion wear is not exclusively controlled by the hardness of the coatings. It has been previously suggested that for having a high erosion resistance, the coating material should have both high hardness and high toughness. Hardness is necessary to reduce the energy transferred from the erodent particles into the material and high toughness increases the material's ability to absorb this energy without fracture[13]. Ability of a material to absorb energy (toughness) could be defined as the area under the engineering stress-strain curve[14]. As a result, high toughness requires a combination of high strength and large ductility.

Although Inconel 625 has a relatively low hardness, its high toughness and work-hardening ability provides it with an unexpected level of erosion resistance. Previous research showed that the surface of Inconel 625 coatings becomes highly deformed during erosion testing. This was accompanied by a significant increase in the hardness of the deformed surface layer (almost doubled)[13] because of high work-hardening ability of Inconel 625[15]. Consequently, the deformed surface of Inconel 625 samples will behave like a material with a higher initial hardness. High work-hardening ability plays a predominant role in producing erosion resistance in many alloys including Hadfield steels, austenitic stainless steels (e.g. AISI 316), Ni and Co based coatings (e.g. Hastealloy 22, Ultimet, Stellite 6) and TiNi among others[13,16,17]. In the case of Inconel 625, the increase in surface hardness combined with its high toughness, provides the coating with erosion wear resistance better than that of a harder but more brittle alloy such as Eatonite 5.

The idea behind developing XL-1 was to obtain an alloy with a preferable combination of high hardness and high toughness to produce hard and crack-free coatings. In the beginning, this was intended to produce hard coatings without the need for preheating or postheating during the laser deposition step. In this way, crack-free coatings (necessary for marine applications) could be attained more easily. Results of the erosion tests showed that the same criteria, i.e. a combination of high hardness and high toughness will also improve the erosion resistance of the coatings. Hence, developing high hardness-high toughness alloys will not only eliminate the

hassles of preheating/postheating during deposition of the coatings, but will also produce coatings with superior functional properties.

Hydraulic piston rods protected by laser deposited coatings are already in production[1,18,19]. Guidelines have also been proposed for qualification of such coatings[20]. The findings of the current work could provide a step forward in developing enhanced laser deposited coatings to protect the components used in marine applications.

6.6 Conclusions

The contents of Cr and B and the Si/B ratio are the predominant compositional characteristics of Ni-Cr-B-Si-C alloys. The former controls the amount of Cr-rich precipitates and the latter determines the volume and nature of the eutectic phases. High-alloy grades of Ni-Cr-B-Si-C (e.g. Colmonoy 69) are very susceptible to cracking. Hence, they are not good candidates for developing laser-deposited coatings for marine applications. A new Ni-base alloy was developed which could produce laser-deposited coatings with a good combination of hardness and toughness as well as superior corrosion and erosion resistance. Finally, it was found out that addressing the hardness-toughness paradox not only makes the deposition step easier, but results in coatings with an enhanced erosion resistance.

References

1. Said, B. A Brief Overview of Corrosion-resistant Piston Rod Coating Technology http://www.eaton.com/ecm/groups/public/@pub/@eaton/@hyd/documents/content/pct_298624.pdf (accessed Apr 8, 2013).
2. E.P.M. van Westing; G.M. Ferrari; J.H.W. de Wit The Determination of Coating Performance with Impedance measurements-I. Coating Polymer Properties. *Corrosion Science* **1993**, *34*, 1511–1530.
3. *Impedance Spectroscopy: Theory, Experiment, and Applications*; Barsoukov, E.; Macdonald, J. R., Eds.; 2nd ed.; Wiley-Interscience: Hoboken, N.J, 2005.
4. *Electrochemical Dictionary*; Bard, A. J.; Inzelt, G.; Scholz, F., Eds.; 2nd ed.; Springer: Heidelberg, 2012.
5. Jiang, W. H.; Kovacevic, R. Laser Deposited TiC/H13 Tool Steel Composite Coatings and Their Erosion Resistance. *Journal of Materials Processing Technology* **2007**, *186*, 331–338.
6. Mens, J. W. M.; Gee, A. W. J. de Erosion in Seawater Sand Slurries. *Tribology International* **1986**, *19*, 59–64.
7. Clark, H. M.; Llewellyn, R. J. Assessment of the Erosion Resistance of Steels Used for Slurry Handling and Transport in Mineral Processing Applications. *Wear* **2001**, *250*, 32–44.
8. Bitter, J. G. A. A Study of Erosion Phenomena Part I. *Wear* **1963**, *6*, 5–21.
9. Kanichi, T.; Hidaka, K. Hard Facing Nickel-Base Alloy **1984**.
10. *ASM Handbook-Alloy Phase Diagrams*; Baker, H., Ed.; 10th ed.; ASM International: Ohio, 1992; Vol. 3.
11. Przybylowicz, J.; Kusinski, J. Laser Cladding and Erosive Wear of Co–Mo–Cr–Si Coatings. *Surface and Coatings Technology* **2000**, *125*, 13–18.
12. Clark, H. M.; Wong, K. K. Impact Angle, Particle Energy and Mass Loss in Erosion by Dilute Slurries. *Wear* **1995**, *186–187, Part 2*, 454–464.
13. Levin, B. F.; Dupont, J. N.; Marder, A. R. Weld Overlay Coatings for Erosion Control. *Wear* **1995**, *181–183, Part 2*, 810–820.
14. Knott, J. F. *Fundamentals of Fracture Mechanics*; Butterworth: London, 1973.
15. Jeong, H.-S.; Ha, M.-Y.; Cho, J.-R. Theoretical and FE Analysis for Inconel 625 Fine Tube Bending to Predict Springback. *International Journal of Precision Engineering and Manufacturing* **2012**, *13*, 2143–2148.
16. Chauhan, A.; Goel, D. B.; Prakash, S. Erosion Behaviour of Hydro Turbine Steels. *Bulletin of Materials Science* **2008**, *31*, 115–120.
17. Weng, J. R.; Chang, J. T.; Chen, K. C.; He, J. L. Solid/liquid Erosion Behavior of Gas Tungsten Arc Welded TiNi Overlay. *Wear* **2003**, *255*, 219–224.
18. LASERTEK Piston Rod Coating http://www.doucehydro.com/index.php?mod=5&id=26 (accessed Apr 8, 2013).
19. Laser Cladding Applications - Innoteq GmbH http://www.innoteq.de/application.php?sub=2 (accessed Apr 8, 2013).
20. Haukas-Eide, O.; Fischer, K. P.; Lønvik, K. Qualification of Wear and Protective Surface Coating for Hydraulic Piston Rods. In *Proceedings of "Corrosion 2006" conference*; NACE: San Diego, CA, 2006.

Chapter 7

SUMMARY AND OUTLOOK

7.1 Summary

This research started with the idea of evaluating the effects of higher cladding speeds on microstructure and properties of laser-clad coatings. It is repeatedly reported that in laser deposition of metallic alloys, a higher cladding speed is beneficial because the microstructure will be refined, energy efficiency improved and hardness increased. The results presented in CHAPTERS 3 & 4 showed that this can be wrong or only partly true. In fact, for martensitic steels this "the faster, the better" approach can deteriorate the properties. In CHAPTER 3, it was discussed that higher cladding speeds refine the austenite cells. This in turn decreases the M_s temperature, reduces the percentage of martensite and results in *lower* hardness and wear resistance. The mechanism was explained in terms of the relationship between M_s and the strengthening of austenite by grain refinement.

In Ni-Cr-B-Si-C alloys, microstructure and properties varied significantly for different alloys (CHAPTER 4-6). An alloy such as Colmonoy 69 proved to be very sensitive to variations in cooling rate, which can be caused for example by increasing the cladding speed. Several microstructural variations could occur in Colmonoy 69 deposits as a result of changes in cooling rate. On the other hand, coatings deposited from Ni-Cr-B-Si-C alloys with a much less alloying content (e.g. Colmonoy 33) were not affected by changes in the cooling rate. Of course, the idea that cladding at higher speeds produces better (in most cases this means harder) coatings, sometime turned

out to be true as observed for Inconel 625 coatings (CHAPTER 6). The key to understand these different behaviors is strengthening mechanism of the alloy system. In physical terms, increasing the cladding speed increases the cooling rate of the coatings. This could refine the scale of constituent phases (because of more abundant nucleation) or initiate alternative phase formation reactions. These phenomena happen because higher cooling rates usually increase the undercooling (CHAPTER 4). Higher cooling rate will refine the cellular or dendritic structure of primary austenite. But this does not mean that hardness of the final martensitic structure will also be higher because that is controlled by the subsequent transformation of austenite to martensite.

In the case of alloys such as Colmonoy 69, phase formation of the system was much more complex and competition between different reactions determined the final microstructure and properties. To predict what exactly happens if Colmonoy 69 (or a similar alloy) is deposited faster, deep knowledge about the competing reactions is needed and no simple answers could be provided. The bottom line is that faster cladding will produce harder coatings only when the alloy is strengthened primarily by grain boundaries as is the case for Inconel 625. Hence, increasing the cladding speed as a method to produce superior coatings has a limited scope, especially given the issues (e.g. more cracking) which arise in deposition at higher rates.

Characterization of microstructures and phases was a central topic in this thesis work (CHAPTERS 3-6). This was done using a wide range of methods especially electron microscopy techniques. Scanning Electron Microscopy (SEM) and its related techniques, i.e. Energy Dispersive Spectroscopy (EDS) and Electron Backscatter Diffraction (EBSD) played a pivotal role in most characterizations. Examples are calculation of phase fractions using EBSD (CHAPTER 3), identification of boride/carbide precipitates using EDS/EBSD combination (CHAPTERS 4-5), studying the effects of dilution on microstructure and phase formation (CHAPTER 4-5), studying the microstructural aspects of crack growth (CHAPTER 4-5), and last but not least, microstructural observations. Other techniques such as X-ray diffraction, Transmission Electron Microscopy and Optical Microscopy (OM) were also used, sometime with unexpected outcomes. For example, OM proved to be essential in revealing the role of eutectic phases in crack growth in Ni-Cr-B-Si-C deposits (CHAPTER 5).

Nowadays, electron microscopy techniques are supplemented with powerful data collection and analysis softwares (e.g. *TSL-OIM* to collect and analyze EBSD data). But even these highly automated devices are far from

ready-to-use packages which provide reliable data at the click of a button. For all of the above-mentioned methods, a careful sample preparation and knowledge of both technique and sample were essential in obtaining high-quality results and avoiding incorrect interpretations.

Much attention was paid to solving (or at least alleviating) the cracking problem in hard laser-clad coatings (CHAPTERS 4-6). The approach adopted in this work was to improve the toughness of the existing alloy materials while preserving their hardness. The idea of microstructural refinement of the boride/carbide precipitates emerged from careful observations of crack growth path (CHAPTER 5). Additions of vanadium, zirconium and niobium to Colmonoy 69 were done to produce new boride/carbide precipitates to act as nucleation sites. Selection of these elements was done according to a set of defined rules. These rules stated that a refining element should be able to spontaneously form boride and/or carbide precipitates at high temperatures with little solubility in their Cr-rich counterparts (CHAPTER 5). Among the added elements, niobium could substantially refine the original microstructure without deteriorating the hardness. However, the refined microstructure of Nb-modified Colmonoy 69 coatings was still susceptible to cracking. Detailed analyses of the crack growth path in Colmonoy 69 and Nb-modified Colmonoy 69 coatings showed that the continuous network of hard eutectics contributed substantially to crack propagation in these alloys (CHAPTER 5). Such a contribution was previously overlooked because the eutectic network could not be clearly observed by SEM, the main observation technique of the work up until then.

When deposition of crack-free coatings from harder grades of Ni-Cr-B-Si-C alloys proved to be very difficult, other Ni-base alloys with lower hardness and better toughness values were selected (CHAPTER 6). At the same time, the lessons learned in CHAPTER 5 about the role of both precipitates and eutectics in crack propagation in Ni-base alloys were used to develop a novel type of Ni-base alloy with a good combination of hardness and toughness (CHAPTER 6).

The final leg of this research was evaluating the functional properties of the coatings. For this purpose, slurry erosion test and Open Circuit Potential (OCP) and Electrochemical Impedance Spectroscopy (EIS) measurements were performed on a number of selected coatings. Laser-clad coatings proved to be free from cracks and pores and able to provide the substrate steel bars with an excellent corrosion resistance. Furthermore, the slurry erosion results showed that a combination of high hardness and high

toughness is needed for a superior erosion resistance and coatings with only higher hardness values do not necessarily offer a better protection against slurry erosion (CHAPTER 6). The coatings deposited from the developed alloy showed the best performance in both corrosion and erosion tests.

7.2 Future work

The investigations of this work can be continued on the following subjects:

(i) *The strengthening mechanism-cooling rate relationships in laser-clad coatings (already underway)*: Alloys with different strengthening mechanisms e.g. grain boundary, grain boundary and carbide precipitates or martensite and carbide precipitates should be investigated for changes in their microstructure and properties upon deposition at different speeds. The results could be combined with those presented in this thesis to get a better picture of the effects of cooling rate on microstructure and properties of laser-clad coatings.
(ii) *In-situ toughness measurements using indentation*: Quantification of toughness values for laser-clad coatings using common techniques such as measurement of plane-strain fracture toughness (K_{IC}) or Charpy impact test requires several layers of coatings because of the required sample sizes for these tests. Indentation on the top surface of laser-clad coatings (after polishing) could be an alternative way to measure fracture toughness without the need for very thick coatings.
(iii) *Application of thermodynamic softwares to analyze the solidification sequence*: This could be particularly helpful for complicated alloy systems like the Ni-Cr-B-Si-C alloys discussed in this work. Software packages such as *Thermo-Calc*® or *Dictra*® could be helpful in understanding the phase formation reactions and in developing new alloys.
(iv) *Corrosion and erosion testing*: The corrosion tests performed in this work did not show large differences between various alloys. More tests for longer periods could better assess the functional performance of the coatings during their lifetime. For the erosion tests, new types of coatings (e.g. Ni-WC composite coatings) could be tested. The ultimate goal should be to define qualification procedures for specific applications.

An outlook for this work is production and qualification of laser-deposited coatings on an industrial scale for a wide range of components in marine applications and similar industries. Such a technology package partly exists in the market. But what makes the outlook of this work novel would be

the use of our developed alloy. By employing the new types of laser, powder injection nozzles and feedback control systems, it should be possible to deposit crack-free coatings without preheating, at high deposition rates and with higher hardness and superior corrosion/wear properties. For this outlook to materialize, a proper upscaling of the outcome of this work as well as developing qualification procedures for the laser-clad coatings is necessary.

LIST OF PUBLICATIONS

Journal papers

I. Hemmati, V. Ocelík, J.Th.M. De Hosson, "Microstructural characterization of AISI 431 martensitic stainless steel laser-deposited coatings", *Journal of Materials Science* 46 (2011) 3405–3414.

I. Hemmati, V. Ocelík, J. Th. M. De Hosson, "Effect of cladding speed in phase constitution and properties of AISI 431 stainless steel laser deposited coatings", *Surface & Coatings Technology* 205 (2011) 5235-5239.

I. Hemmati, V. Ocelík, and J.Th.M. De Hosson, "Dilution effects in laser cladding of Ni–Cr–B–Si–C hardfacing alloys", *Materials Letters* 84 (2012) 69–72.

I. Hemmati, J.C. Rao, V. Ocelík and J.Th.M. De Hosson, "Electron Microscopy Characterization of Ni-Cr-B-Si-C Laser Deposited Coatings", *Microscopy and Microanalysis*, 19 (2013) 1-12.

I. Hemmati, J.C. Rao, V. Ocelík, J.Th.M. De Hosson, "Phase formation and properties of vanadium-modified Ni-Cr-B-Si-C laser deposited coatings", *Journal of Materials Science* 48 (2013) 3315–3326.

I. Hemmati, V. Ocelík, J.Th.M. De Hosson, "Effects of the alloy composition on phase constitution and properties of laser deposited Ni-Cr-B-Si coatings", *Physics Procedia* 41 (2013) 302-311.

I. Hemmati, V. Ocelík, J.Th.M. De Hosson, "Advances in Laser Surface Engineering: Tackling the Cracking Problem in Laser-Deposited Ni-Cr-B-Si-C Alloys", *JOM* 65 (2013) 741-748.

I. Hemmati, V. Ocelík, J.Th.M. De Hosson, "Toughening mechanism for Ni-Cr-B-Si-C alloys", *Materials Science and Engineering A* 582 (2013) 305-315.

I. Hemmati, R. Huizinga, V. Ocelík, J.Th.M. De Hosson, "Microstructural design of hardfacing Ni-Cr-B-Si-C alloys", *Acta Materialia* 61 (2013) 6061-6070.

I. Hemmati, V. Ocelík, K. Csach, J.Th.M. De Hosson, "Microstructure and phase formation in a rapidly solidified laser deposited Ni-Cr-B-Si-C hardfacing alloy", *Metallurgical and Materials Transactions A*, in press.

I. Hemmati, V. Ocelík, J.Th.M. De Hosson, Microstructure and properties of Ni-base coatings for marine applications, in preparation for submission to *Applied Surface Science*.

V. Ocelík, M. Eekma, **I. Hemmati**, J.Th.M. De Hosson, "Elimination of Start/Stop defects in laser cladding", *Surface & Coatings Technology* 206 (2012) 2403-2409.

Conference presentations

I. Hemmati, M. Dutka, V. Ocelík, J. Th. M. De Hosson, "Characterization of a martensitic stainless steel coating deposited by high speed laser cladding", *Surface Modifications Technologies XXIV*, Eds. T.S. Sudarshan, E. Beyer and L.M. Berger, Valardocs 2011, pp.297-303.

I. Hemmati, V. Ocelík, J.Th.M. De Hosson, "Evolution of microstructure and properties in laser cladding of a Ni-Cr-B-Si hardfacing alloy", *Surface Effects and Contact Mechanics X*, Eds. J.Th.M. De Hosson and C.A. Brebbia, WIT Transactions on Engineering Sciences, Vol 71, © 2011 WIT Press, ISSN 1743-3533 (on-line), pp.287-296. doi:10.2495/SECM110251.

I. Hemmati, V. Ocelík and J. Th. M. De Hosson, "Microstructure and properties of V-modified Ni-Cr-B-Si-C laser deposited coatings", in proceeding of *Surface Modification Technologies XXVI*, Lyon, France, June 20-22, 2012, pp. 315-324, proceedings editors: T. S. Sudarshan, M. Jeandin and V. Fridrici, published by VALARDOCS, first printing, February 2013, ISBN: 978-81-926196-0-6.

V. Ocelík, **I. Hemmati**, J.Th.M. De Hosson, "Characterization of Protective Layers Produced by Laser Treatment", *31st International Congress on*

Applications of Lasers & Elektro-Optics, September 23-27, 2012 Anaheim, California USA, Paper #1806, pp.608-617.

V. Ocelík, M. Eekma, **I. Hemmati**, M. Dutka, J.Th.M. De Hosson, "Experimental approach to eliminate start/stop defects in laser cladding", *Surface Effects and Contact Mechanics X*, Eds. J.Th.M. De Hosson and C.A. Brebbia, WIT Transactions on Engineering Sciences, Vol 71, © 2011, WIT Press, ISSN 1743-3533, pp.245-254. doi:10.2495/SECM110211

V. Ocelík, **I. Hemmati**, J.Th.M. De Hosson, "Laser cladding of metallic coatings: processing-microstructure-properties relation (invited lecture)", *Laser Applications in Industry 2013*, March 19-20, 2013 Plzeň, Czech Republic, ed. S. Němeček, Matex PM, pp.33-40.

V. Ocelík, O. Nenadl, **I. Hemmati**, J. Th. M. De Hosson, "Thickness and waviness of surface coatings formed by overlap: modeling and experiment", *Surface Effects and Contact Mechanics XI*, WIT Transactions on Engineering Sciences, Vol 78, © 2013 WIT Press, pp. 135-143. doi:10.2495/SECM130111.

Patent applications

I. Hemmati, V. Ocelík, J.Th.M. De Hosson, "Enhanced hardfacing alloy and a method for the deposition of such an alloy", *Dutch patent application number N2009730*, filed on October 30, 2012

I. Hemmati, V. Ocelík, J.Th.M. De Hosson, "Nickel-base alloy, coating of such an alloy, and method for manufacturing such a coating", *Dutch patent application number N2010674*, filed on April 19, 2013.

Book chapter

I. Hemmati, V. Ocelík, J.Th.M. De Hosson, "Compositional modification of Ni-base alloys for laser-deposition technologies", to be published in *Laser surface engineering: Processes and applications*, Eds Jonathan Lawrence, Colin Dowding, David Waugh and Jonathan Griffiths, Woodhead Publishing Ltd., 2013.

ACKNOWLEDGEMENTS

It is the time for me to recollect my memories of the past four years and acknowledge those who helped me in one way or another. I got excited about doing a PhD in the Materials Science (MK) group from my very first day here. That day was February 26th, 2009 when I had my PhD application interview. I remember the day very clearly; from its typical cloudy Dutch weather to drinking milk for lunch (nobody does that in Iran!) and the army of bicycles outside each building. However, what I remember the most are not those trivial details, but the impressive and welcoming attitude of my future supervisors. I had a quite lengthy chat (couple of hours) with Prof. Jeff De Hosson in the morning during which we talked about research, Iran, the Netherlands, Groningen, lasers, and many more topics. That conversation was one of my most pleasant ones up until then. During the last four years, I had the privilege of working with Prof. De Hosson and we had many more of those inspiring and enjoyable talks. Jeff, I appreciate very much the opportunity you gave me to do my PhD in your fabulous research group. I learned and enjoyed a lot from your knowledge, integrity, discipline, sense of humor and easygoing character and I am so grateful to you for many things; the freedom you gave me to follow my ideas in this research, your incredibly fast response to my queries, your support to attend conferences and courses, just to name a few.

I did a satisfying, exciting and pleasant research during my PhD. This could not happen without the help and support from my daily supervisor and co-promoter Dr. Vaclav (Vasek) Ocelik. I consider myself very lucky that I was supervised by someone so knowledgeable, competent, kind and patient. I enjoyed very much working with Vasek and I especially had great times when we attended conferences and other professional events together, from Malta to Sweden and from Wales to Germany. Thank you Vasek for all you did for me!

Several other members of the MK group helped me with completing this work. I am thankful to Dr. David Vainchtein for his help with professional and non-professional matters. The members of MK group (including myself) do not need to worry about research facilities when David is around! I am grateful to Dr. Yutao Pei and Dr. Paul Bronsveld for the nice

discussions and their help with some of the experimental devices. Mikhail Dutka was one of my first roommates in the MK group. As a PhD student and one of our technical staff, he has been a great colleague to whom I am very grateful. Among the present and past members of the MK group, I am especially thankful to Dr. Jiancun Rao. He did an excellent Transmission Electron Microscopy analysis for me which played a big role in completing my research. His knowledge, dedication and sense of humor made him a great colleague. Thank you JC! I also thank Elly Eekhof for handling the administrative burden. I wish to thank Jacob Bass (Research Group Solid State Materials for Electronics) for being really helpful with XRD measurements. Richard Huizenga (TU Delft) is appreciated for performing excellent Thermo-Calc simulations.

I could not perform my PhD studies without the financial support of Materials innovation institute (M2i) and I am really grateful for this opportunity. Several people made my M2i experience a pleasant one. My special thanks go to Monica Reulink for being extremely helpful to me, especially for my application interview and the subsequent employment by M2i. I also would like to thank Bert van Haastrecht and people from HR and financial departments of M2i. Dr. Erik van Westing is kindly appreciated for his help with interpreting the results of the corrosion tests. The industrial colleagues of the project Dr. Pieter Quist and Jeroen Braadbaart (MTI Holland), Nico Kamperman and Roy Kastelein (DAF) are appreciated for their help and support.

I would like to thank members of my thesis' reading committee Prof. Petra Rudolf, Prof. Hans De Raedt and Prof. Laurens Katgerman for their careful reading and valuable comments. I am also grateful to my paranymphs Dr. Willem van Dorp and Ali Ghavami. I enjoyed very much the last months of my PhD with Willem as my roommate. I am much obliged to him for explaining the purpose of including "stellingen" in a PhD thesis! Ali Ghavami has been my second best buddy in Groningen (my wife was the first!). I am thankful to him for being such a nice friend to me.

I had a great time with the members of the MK group: Eric Detsi, Sergey Punzhin, Oleksii Kuzmin, Kalpak Shaha, Tony Kazantzis, Zhenguo Chen, Sriram Venkatesan, Huajie Yang, Diego Martinez Martinez, Catalina Mansilla-Sanchez, Enne Faber, Jintao Shen, Willem Pier Wellinga, Ferry Wieland, Anatoly Turkin, Ali Eivani, Ondrje Nenadl and Winand Slingenbergh. Ivan Furar and Jozef Vincenc Obona were my roommates during most of my PhD studies. I also spent six great months with Amirreza

Farnia as my roommate. I am grateful to them for all the fun and the nice moments we had together. A nice memory of my PhD studies was being a member of the MK football team together with Diego, Sergey, Enne, Catalina, Winand, Jintao, Jozef, Ivan, Ali Eivani, Ali Ghavami and Oleksii. Thank you all for making the past four years memorable! I enjoyed being with my Iranian friends: Sara, Amirhossein, Saeedeh, Saloomeh, Qader, Elham, Morteza, Parisa, Mehdi, Mehrnoosh, Mehrsima, Nafiseh and Fariba. Together, we could forget that we were away from home. Merci guys! I am sincerely grateful to our first neighbors in Groningen Dr. Syamak Solaymani, his wife Solmaz and their little daughter Atanaz for their help and support during our first months of living here.

Martin Luther King, Jr. once said that "Occasionally in life there are moments which cannot be completely explained by those symbols called words. Their meanings can only be articulated by the inaudible language of the heart." I could not explain my feelings about acknowledging my family more eloquently. I am deeply indebted to my mom and dad for their endless love and support. They made many sacrifices for me (and my siblings) for which I am truly grateful. I know my living abroad was not easy for them to cope with. But in the end, they accepted this as they knew this was what I wanted. Thank you mom and dad! I am also grateful to my brothers, my sister and my in-laws for supporting me and my wife in various ways during my PhD studies. Finally, I am quite sure I would have been lonely and much less happy during my stay in Groningen without my wife Sahar. She has been my best buddy in these years and has never stopped caring for me. Dear Sahar, I am grateful to our creator for having you by my side! Thank you for supporting me all along this way.

Ismail Hemmati
Groningen
September 2013